Search for resonant $WZ \to \ell\nu\ \ell\ell$ production using 13 fb^{-1} in $\sqrt{s} = 8$ TeV p-p collisions with the ATLAS detector

by

Peter Loscutoff

A dissertation submitted in partial satisfaction of the
requirements for the degree of
Doctor of Philosophy

in

Physics

in the

Graduate Division

of the

University of California, Berkeley

Committee in charge:

Professor Marjorie Shapiro, Chair
Professor Jim Siegrist
Professor Philip Stark

Spring 2013

The dissertation of Peter Loscutoff, titled Search for resonant $WZ \to \ell\nu\ \ell\ell$ production using 13 fb^{-1} in $\sqrt{s} = 8$ TeV p-p collisions with the ATLAS detector, is approved:

Chair _____ Date _____

_____ Date _____

_____ Date _____

University of California, Berkeley

Search for resonant $WZ \to \ell\nu\ \ell\ell$ production using 13 fb^{-1} in $\sqrt{s} = 8$ TeV p-p collisions with the ATLAS detector

Abstract

Search for resonant $WZ \to \ell\nu\ \ell\ell$ production using 13 fb^{-1} in $\sqrt{s} = 8$ TeV p-p collisions with the ATLAS detector

by

Peter Loscutoff

Doctor of Philosophy in Physics

University of California, Berkeley

Professor Marjorie Shapiro, Chair

This dissertation presents a search for a resonant state decaying to a W and a Z boson using events with three charged leptons (electrons or muons) and missing transverse energy. The search is performed using proton-proton collisions at a center-of-mass energy of 8 TeV, produced by the LHC and measured by the ATLAS detector in 2012. This data sample corresponds to an integrated luminosity of 13.0 fb^{-1}. Events are selected with reconstructed W and Z bosons found at similar rapidity and large angular separation. The invariant mass of three leptons and missing energy is calculated, assuming on-shell W production, and compared to the Standard Model expectation. No significant excess is observed and the results are interpreted as cross-section times branching ratio limits for two specific models. In the context of an Extended Gauge Model, a W' boson is excluded at a 95 % confidence level for masses below 1180 GeV. In the context of a Low Scale Technicolor model, two-dimensional limits are set for values of the technipion and technirho mass between 200 GeV and 1000 GeV. These limits are generalizable to any model predicting a narrow resonance that decays to a W and a Z boson.

To Mom and Dad

who have given me an abiding love for science.

Contents

List of Figures

List of Tables

Acknowledgments

This dissertation, and my time as a graduate student, would look very different without the influence of my adviser, Marjorie Shaprio, who has ensured that the path I have followed for the last years has been one of my own interests. She should also be acknowledged for getting me back on course when this path has taken me into the weeds. Her wealth of knowledge and willingness to dispense it has kindled a deep interest and respect for experimental physics that I grasped only faintly when I came into this program.

More broadly, the Berkeley ATLAS group has been without equal in their enthusiasm and expertise in discussing physics. I would not have the breadth of knowledge that I do now without their willingness to answer my innumerable questions. Among them, Juerg Beringer made sure that I was on hand when the first collisions were observed in the ATLAS detector, Shih-Chieh Hsu put me in contact with a many interesting projects and interesting people, Sarah Strandberg happily oversaw my training in both the pixel detector and the code used to operate it.

I have been fortunate to have a constant companion in Andre Bach. Andre studied for preliminary exams with me, joined the ATLAS group with me, and was an office mate more often than not after that. I do not know where I will be now that I cannot turn to the left and talk to him about the physics or coding problem that I am having today. He may very well be more productive without my constantly distracting him, but I could not have asked for a better peer.

The enthusiasm of Lindsey Gray, Johannes Ebke, and Peter Waller about physics, and coding, and chili has influenced me profoundly. I could not hope for better friends and better comrades during my deployment to CERN, which will be a different place in their absence. The most interesting things that I know about python, I know because of them.

Most importantly, this dissertation would not have been possible without the love and support of my wife, Megan. Thank you.

Chapter 1

Introduction

By the end of 2012, the Large Hadron collider (LHC) had completed an impressive run. In just over three years, the accelerator had traced a path through half a century of particle physics, starting with the characterization of proton-proton interactions [13], and proceeding through to the measurement of top quark cross section [14]. Crowning this impressive run is, potentially, the discovery of the Higgs boson [15].

This success is, however, bittersweet. The theoretical framework that underpins these measurements, the Standard Model, was first put forward more than 30 years ago. Since then, countless ideas have arisen for new physics beyond the Standard Model, and countless ideas have died at the hands of experimentalists. It is, in this sense, difficult to pin one's hopes on some particular model of new physics. History has not been kind to those who have done so.

As consolation, the experimentalist needs no particular theory to test the predictions of the Standard Model. While a theorist might dream of replacing the Standard Model, the experimentalist dreams of finding some new physics that no theory has considered. In this sense, the search for new physics can proceed based on the levers that the experimentalist has a firm hand on. If such a search finds no new phenomena, she joins decades of colleagues who have continued to verify the remarkable performance of the Standard Model. If such a search succeeds, her colleagues will flock to postulate the underlying theory of this new observation.

The reader should keep this motivation in mind when she reaches Chapter 7, noting just how many times the W and Z bosons are used as a standard candle to calibrate some process. In addition to the more concrete motivation, described in Chapter 2, the search for new physics decaying to these gauge bosons is motivated by the clean signature and excellent understanding of these particles from an experimentalist's point of view. In a similar manner, although an excellent understanding of the strong interaction and jets has been developed during the tenure of the Standard Model, electrons and muons remain, where they are available, much more powerful levers for probing the physics of particle colliders.

Aiming to use the powerful levers of weak boson production identified via electrons and muons, this dissertation presents a search for new physics that results in resonant production

of W Z boson pairs, which subsequently decay to three leptons (electrons or muons) and a neutrino, measured as missing transverse energy. The results are interpreted in the context of a technicolor ρ_T and an extended gauge model W'. This analysis uses 13.0 fb^{-1} of p-p collisions with $\sqrt{s} = 8$ TeV, collected using the ATLAS detector at the LHC. This dissertation expands on the work described in [16], which is an approved public result of the ATLAS collaboration.

This dissertation is organized as follows: Chapter 2 describes the background to the measurement, including the theoretical framework for this work and previous searches that have been performed. Chapter 3 describes the experimental setup of the LHC and the ATLAS detector, which were used to generated and collect the data used in this measurement. Chapter 4 gives a brief overview of the analysis strategy used for the measurement. Chapter 5 describes the reconstruction of physics objects from detector signals. Chapter 7 describes the specific use of those objects in the context of this analysis. Chapter 6 describes the data sample used in this analysis along with the simulation-driven and data-driven techniques used to estimate the contribution of various backgrounds to these data. Chapter 9 describes the sources of systematic uncertainty that affect this search. Chapter 10 describes the results of this search, interpreted in the context of several new physics models. Finally, Chapter 11 provides the conclusions arrived at in this measurement, including an outlook for improving future searches in this channel.

Chapter 2

Theoretical Framework

2.1 The Standard Model

The Standard Model of particle physics provides a remarkably concise description of matter at the smallest probeable scales. Since its formulation was finalized in the 1970s, it has survived almost completely intact, and seen the observation of the bottom quark [17] the top quark [18][19], the tau neutrino [20], and quite possibly the Higgs boson [15]. While the Standard Model cannot be a theory of "everything," at the least because it does not include a description of gravity or account for massive neutrinos, it has demonstrated both a remarkable theoretical elegance and an experimental hardiness that has withstood the probes of generations of graduate students and their betters.

The remainder of this chapter describes the theoretical framework and motivation for pursuing a search for a narrow resonance decaying to WZ. A complete description of quantum field theory and the Standard Model can be found in [21] and [22], which are cited here and used throughout this chapter. Discussions of fundamental physics and particle properties will use the convention $\hbar = c = 1$, for simplicity of units, although this convention is thoughtfully abandoned in discussions human-scale phenomena, e.g., in Section 3.2.

2.1.1 Standard Model Phenomenology

In the Standard Model, matter is composed of spin-1/2 quarks and leptons and spin-1 vector bosons. Quarks come in up-type and down-type varieties with an electric charge ($Q_u = +2/3$, $Q_d = -1/3$). Quarks come in three generations: up (u), charm (c), and top (t) for up-type quarks and down (d), strange (s), and bottom (b) for down-type quarks. The quark generations, and all generations in the Standard Model, differ only in mass from each other, with later generations being progressively heavier. Like quarks, leptons are divided into two types, charged leptons ($Q_\ell = -1$) and neutrinos ($Q_\nu = 0$). Also like quarks, leptons come in three generations: electron (e), muon (μ), and tau (τ), and their associated neutrinos (ν_e, ν_μ, ν_τ), again with generations differing only by their mass.

The spin-1 vector bosons are the carriers of the fundamental forces: electromagnetic, weak and strong. The electromagnetic force is carried by the photon, γ. The weak force is carried by the charged W bosons W^+ and W^- with $Q = \pm 1$, and the neutral Z. The strong force is carried by the gluon. Of the gauge bosons, only the W and Z are massive. The existence of this mass necessitates some outside mechanism to provide it. The simplest such mechanism gives rise to one additional particle, the spin-0 neutral Higgs. A table of the particles in the Standard Model can be found in Table 2.1.

Particle	Spin	Charge	Color	Mass
(e) electron	$\frac{1}{2}$	-1	singlet	5.11×10^{-4} GeV
(μ) muon	$\frac{1}{2}$	-1	singlet	0.106 GeV
(τ) tau	$\frac{1}{2}$	-1	singlet	1.77 GeV
(ν_e) electron neutrino	$\frac{1}{2}$	0	singlet	$< 2 \times 10^{-9}$ GeV
(ν_μ) muon neutrino	$\frac{1}{2}$	0	singlet	$< 1.9 \times 10^{-4}$ GeV
(ν_τ) tau neutrino	$\frac{1}{2}$	0	singlet	$< 18.2 \times 10^{-2}$ GeV
(u) up	$\frac{1}{2}$	$+\frac{2}{3}$	triplet	0.0023 GeV
(c) charm	$\frac{1}{2}$	$+\frac{2}{3}$	triplet	1.29 GeV
(t) top	$\frac{1}{2}$	$+\frac{2}{3}$	triplet	172 GeV
(d) down	$\frac{1}{2}$	$-\frac{1}{3}$	triplet	0.0049 GeV
(s) strange	$\frac{1}{2}$	$-\frac{1}{3}$	triplet	0.095 GeV
(b) bottom	$\frac{1}{2}$	$-\frac{1}{3}$	triplet	4.18 GeV
(γ) photon	1	0	singlet	0
(W) W boson	1	± 1	singlet	80.4 GeV
(Z) Z boson	1	0	singlet	91.2 GeV
(g) gluon	1	0	octet	0
(H) Higgs(?)	0	0	singlet	~ 125 GeV

Table 2.1: The particles of the Standard Model [1].

A certain amount of degeneracy exists in this description. First, each matter particle has a corresponding anti-particle; the positron to the electron and so on. The Higgs, Z, γ, and g are their own anti-particles, and the W^+ and W^- are anti-particles of each other. Quarks come with a "color" charge, associated with the strong force. There are three possible quark colors. Similarly, there are eight varieties of gluon, associated with a combination of a color and anticolor, aside from color charge. Quarks and gluons, or any other state with net color cannot be observed individually. Instead, particles with the color charge are always found in bound, colorless states in a process referred to as confinement.

Quarks and gluons produced in hard collisions at a hadron collider like the LHC are observed as a spray of colorless particles, called a *jet*, generated by soft radiation of colored particles off of the initial hard object. While both muons and taus are unstable, a muon

produced a LHC experiment will escape the detector before decaying, while a tau will decay before reaching any part of a detector. This dissertation will refer leptons that leave direct signatures in a LHC experiment as ℓ, denoting either an electron, e or muon, μ.

2.1.2 Standard Model as Gauge Theory

The Standard Model is a relativistic quantum field theory based on the principal of gauge invariance. Gauge invariance implies that the Lagrangian of the theory is invariant under a set of local transformations. These transformations define the symmetry group of the theory. Each symmetry group is further associated with a gauge field. The quanta of this gauge field are the gauge bosons. These bosons carry a force that is defined by the gauge field, and thus the symmetry group. Matter exists in representations of these gauge groups. The specific representation defines charge that matter has with respect to a given force.

The symmetry group of the Standard Model is:

$$SU(3)_C \otimes SU(2)_L \otimes U(1)_Y, \tag{2.1}$$

where $SU(3)_C$ is the symmetry group associated with the gluon, and gives rise to Quantum Chromodynamics (QCD), and $SU(2)_L \otimes U(1)_T$ is the symmetry group associated with the photon, W and Z, and gives rise to the Electroweak interaction. Both QCD and the electroweak interaction are non-Abelian: The elements of their symmetry groups do not all commute with each other.

2.1.3 QCD

Quantum Chromodynamics describes the interactions of quarks and gluons via the strong force. Any physics coming from collisions in the LHC will necessarily start from the interaction of the quarks and gluons inside the colliding protons. Hence, even in a search for a fundamentally electroweak process, like $WZ \to \ell\nu\ell\ell$, a good understanding of QCD is necessary.

It is interesting to consider why we can perform calculations in the context of QCD at all [23]. Low energy interactions mediated by the strong force were, and continue to be, remarkably difficult to describe. This is particularly true in the context of quantum field theory where calculations mean the application of perturbation theory via Feynman rules. This difficulty can be examined by considering the running of the strong coupling constant with energy (see Figure 2.1). At low energy, the strong coupling constant becomes O(1). With O(1) couplings, perturbation theory fails; perturbations are the size of the initial calculation. This running of the strong coupling constant with energy also explains why QCD can be used for hadron collider physics: In the other extreme, at high energy, the strong coupling constant becomes small. Small couplings allow the use of perturbation theory, and thus the calculation of a whole host of phenomena. This decreased coupling at high energy is one of the defining features of QCD: *Asymptotic freedom*. It allows quarks and gluons

to be treated as free particles in the context of high energy particle collisions, even though these free particles are not observed at low energy and long time scales.

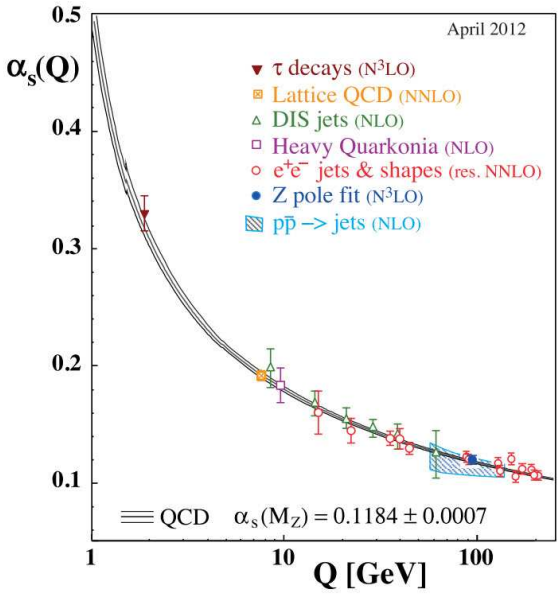

Figure 2.1: α_s, the strong coupling constant, as function of the energy scale, Q [1]

Theoretically, the running of the strong coupling constant, and thus the source of asymptotic freedom, can be calculated from the symmetry group defining the field. For the SU(3) symmetry group of QCD, this the contribution of gluons decreases the coupling at higher energy scales. The contribution of quarks in QCD ameliorates this running of the coupling, but does not prevent it. This can be understood in analogy to paramagnetism and diamagnetism. In the presence of a magnetic field (colored charge), paramagnetic materials (gluons) will tend to align with the field and enhance it while diamagnetic materials (quarks) will tend to align in opposition to the field. The vacuum in quantum field theory being filled with a sea of particle-antiparticle pairs, means that at long distances and thus, low energies, the effect of color charge is greatly enhanced by the polarized vacuum, while at short distances and high energies, it is diminished.

The other important principal of QCD is that of *confinement*. As discussed earlier, bare quarks and gluons are not seen in nature. Instead, they are always found to be part of some color singlet hadron. The qualitative explanation for this is as follows: The increase of α_s at low energy and large distance means that, as two colored objects that form a singlet are moved apart, the energy required to separate them increases without bound. At some point, it is energetically favorable to fluctuate a new quark-antiquark pair out of the vacuum. This new quark-antiquark pair then screens the original charges, and generates two new color singlet pairs. The one pair that had formed a color singlet becomes two pairs that form color singlets, but no bare charge remains. [24].

This qualitative description is played out constantly at the LHC. Quarks inside of protons scatter with energies much larger than the scale of confinement (~ 0.2 GeV). As the quarks are separated, new colored particles fluctuate from the vacuum, generated by the tremendous energy required for this separation. These new particles are also scattered, somewhat, with respect to the original quarks and they too separate, and fluctuate new colored particles out of the vacuum. This process continues until the energy moving the quark pairs apart is $\sim \Lambda_{QCD}$, at which point new color singlets are formed, and the resulting experimental signature is a collimated spray of hadrons, all of them color singlets, forming a jet.

Moreover, in spite of the failure of perturbative quantum field theory to describe low energy QCD, this qualitative description, formalized as the Lund string model, is at the heart of the PYTHIA event generator [25], used extensively throughout this analysis with remarkable accuracy. Similar models of non-perturbative QCD are also used with great success by other Monte Carlo generators such as SHERPA [26] and ALPGEN [27].

Thus, high energy interactions in QCD, such as the scattering of two quarks, can be calculated perturbatively because of asymptotic freedom. Low energy interactions, like the behavior of the proton containing those quarks, are subject to the principal of confinement and have only empirical descriptions, albeit very good ones. A proton-proton collision then, naturally interfaces these two regimes in experiment. The interface of these two regimes handled by the use of *factorization*. Factorization divides the calculation of an observable in a proton-proton collision into a perturbative part, where quarks interact in a manner governed by perturbative QCD, and a non-perturbative part, where those quark properties are the result of a universal understanding of proton structure. The representation of proton structure, here, comes in the form of Parton Distribution Functions (PDFs), which describe the amount of momentum carried by the proton constituents. An example of the PDFs calculated by the MSTW group is shown in figure 2.2, giving the probability density of observing particular kinds of partons (quarks and gluons) with a particular fraction of the proton longitudinal momentum at a given energy scale (Q^2). The difference in PDFs as a function of energy scale is a result of running of α_s with energy scale. An illustration of this model of proton-proton interactions can be seen in Figure 2.3, where a quark and antiquark in colliding protons interact in a "hard scatter," each carrying momentum described by the proton PDF.

2.1.4 The Electroweak Sector

Quantum Electrodynamics, (QED), is an Abelian gauge theory based on the $U(1)$ symmetry group, which describes the interaction of photons and matter at very short distances. The weak force was originally described as a contact interaction, requiring no mediating force carrier. This description was useful, but insufficient at high energy, and mathematically unsatisfying as it was a nonrenormalizable theory. A unified, electroweak theory, based on the $SU(2)_L \otimes U(1)_Y$ symmetry group solves these issues with contact interaction model of the weak force and provides a description of both the electromagnetic and weak forces in

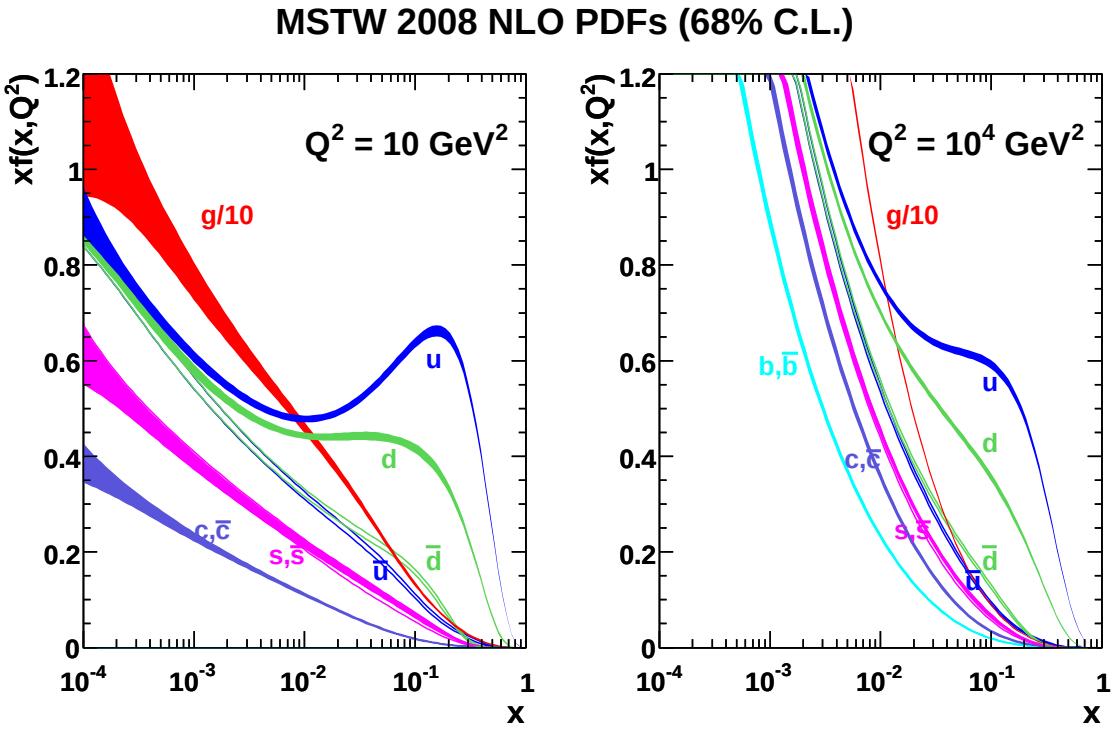

Figure 2.2: Proton Parton Distribution Function as calculated by the MSTW group at a scale of $Q^2 = 10$ GeV^2 (left) and $Q^2 = 10,000$ GeV^2 (right).[2]

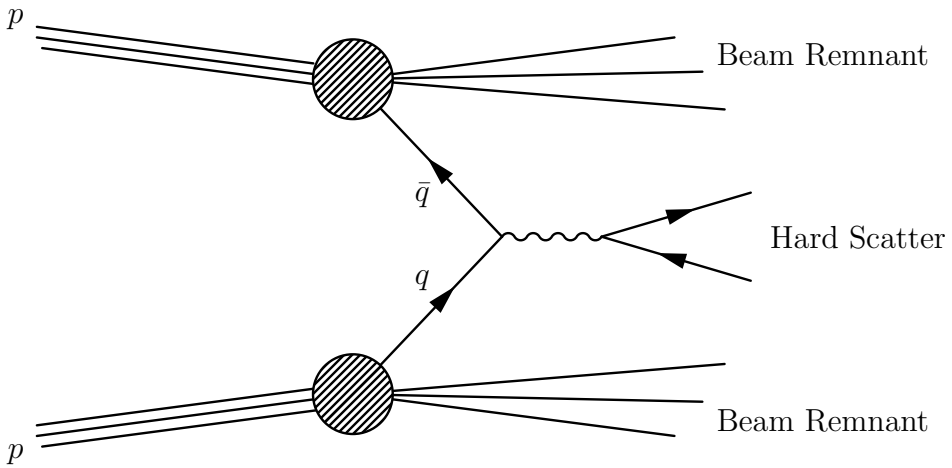

Figure 2.3: A proton-proton collision. The colliding quarks carry some fraction of the proton momentum, determined by the proton PDF. An example hard scattering process is shown, along with the beam remnants.

a single framework. This unified electroweak theory earned Glashow, Salam, and Weinberg

the 1979 Nobel Prize in Physics.

In the weak sector, only left handed particles and right handed anti-particles interact with the SU(2) fields. This interaction can be formalized by writing the left handed matter as SU(2) doublets and right handed matter as SU(2) singlets:

$$\begin{pmatrix} \nu \\ \ell \end{pmatrix}_L, \ell_R \tag{2.2}$$

$$\begin{pmatrix} u \\ d \end{pmatrix}_L, u_R, d_R. \tag{2.3}$$

The weak eigenstates here are not necessarily the same as the mass eigenstates, giving rise to quark and neutrino mixing in the weak interaction defined by the CKM matrix and PMNS matrix, respectively. The possibility of a right handed neutrino is excluded here because such a particle would be a singlet with respect to all of the Standard Model fields, and thus would not interact at all.[1]

The fields of a $SU(2) \otimes U(1)$ gauge theory can be written as $A_\mu^{\ a}$ for $a = 1, 2, 3$ and B_μ corresponding to the $SU(2)$ and $U(1)$ gauge fields with coupling strengths g and g' respectively. If a complex scalar field in the $SU(2)$ doublet representation, ϕ, is introduced and allowed to take a vacuum expectation value, the gauge symmetry can be broken and a model that fits the electroweak interaction can be developed.

To bring about a vacuum expectation value for ϕ, consider a potential:

$$V(\phi) = -\mu^2 \phi^\dagger \phi + \lambda (\phi^\dagger \phi)^2. \tag{2.4}$$

There is no explicit breaking of the SU(2) symmetry in this term, but for $\mu > 0, \lambda > 0$, the minimum value of this potential occurs at a non-zero point. This minimum of the potential occurs at, $\phi^\dagger \phi = \mu^2/(2\lambda)$. The vacuum of this field must exist at some specific point though, and by gauge invariance, the coordinates can be rotated so that it lies at

$$\langle \phi \rangle = \frac{1}{\sqrt{2}} \begin{pmatrix} 0 \\ v \end{pmatrix}. \tag{2.5}$$

The introduction of this vacuum expectation value generates mass terms for particular

[1] The existence of neutrino flavor oscillation implies finite mass differences between the neutrino flavors, and thus massive neutrinos. A model for massive neutrinos would need to incorporate right handed neutrinos as well.

combinations of the original fields. Specifically:

$$W_\mu^\pm = \frac{1}{\sqrt{2}}(A_\mu^1 \mp iA_\mu^2), \quad \text{with} \quad m_W = g\frac{v}{2} \tag{2.6}$$

$$Z_\mu^0 = \frac{1}{\sqrt{g^2+g'^2}}(g'A_\mu^3 - g'B_\mu), \quad \text{with} \quad m_Z = \frac{v}{2}\sqrt{g^2+g'^2} \tag{2.7}$$

$$A_\mu = \frac{1}{\sqrt{g^2+g'^2}}(g'A_\mu^3 + g'B_\mu), \quad \text{with} \quad m_A = 0. \tag{2.8}$$

We identify these mass eigenstates with the $W^\pm$ bosons, the Z boson, and the photon, respectively. From the original $SU(2)_L \otimes U(1)_Y$, a $U(1)_{EM}$ gauge symmetry is preserved, corresponding to the standard gauge symmetry of QED. Finally, the parameters of the original $SU(2)_L \otimes U(1)_Y$ symmetry can be rewritten in terms of the broken symmetry. The electron charge can be written:

$$\frac{gg'}{\sqrt{g^2+g'^2}}. \tag{2.9}$$

The rotation needed to map the A [3] and B fields onto the Z^0 and A fields can be written as the weak mixing angle, θ_w. Conveniently, this mixing angle can be expressed in terms of the W and Z boson masses:

$$cos(\theta_w) = \frac{m_W}{m_Z}. \tag{2.10}$$

In addition to these relations, a mass scale is necessary to characterize this symmetry breaking. This was originally introduced as the size of the Higgs vacuum expectation value v, which is ~ 246 GeV. The W or Z boson mass are more directly accessible however, and more frequently used.

In the process of breaking the electroweak symmetry, three of the four (for a complex doublet) degrees of freedom related to the original Higgs field are absorbed as the longitudinal polarizations for the, now-massive, gauge bosons. What remains is the field associated with a single scalar Higgs boson. At the conception of this dissertation, the search for this Higgs boson was proceeding in earnest, but had not yet produced results. At the writing of this dissertation, that search has produced a new particle at ~ 125 GeV [15] , with properties that are not inconsistent with such a single scalar Higgs boson.

2.2 Beyond the Standard Model

There is certainly physics beyond the Standard Model. Some quantum deception of gravity will become necessary at scales of 10^{19} GeV. In the ranges between 10^3 GeV, probed by the LHC and 10^{19}, is should not be at all surprising to find some phenomenon not yet considered. Further, the Standard Model fails to provide explanations for a number of physical observations: The existence of dark matter is well documented, but the Standard Model provides no

dark matter candidate. The observable universe is composed of matter, but not anti-matter. While the Standard Model can provide for matter-antimatter asymmetry, it cannot provide enough asymmetry to explain the universe as it exists. Even so, the motivation for physics beyond the Standard Model is experimentally unhelpful without a parallel motivation for some mass scale to consider.[2]

Clearly the electroweak symmetry is broken. The existence of massive W and Z bosons has been experimentally measured for three generations of colliders at this point. Further, the universality of the W coupling to quarks and leptons indicates that the W and Z are the gauge bosons of a spontaneously broken $SU(2)\otimes U(1)$ symmetry. While the simplest method of this symmetry breaking might be the introduction of a single scalar SU(2) doublet, this is by no means the only manner in which the electroweak symmetry can be broken. This simple breaking leads to the existence of a fundamental scalar particle, the Higgs boson, which would be unprecedented. The Standard Model, as it has been observed, contains matter particles with spin 1/2, interacting through forces mediated by gauge bosons with spin 1. The Higgs in this simplest theory would be a fundamental spin 0 particle.

The Higgs mechanism, described above can also be used to provide a mass for the fundamental fermions, through the Yukawa coupling terms, which are related to the Higgs vacuum expectation value as:

$$m_f = \frac{1}{\sqrt{2}}\lambda_f v, \tag{2.11}$$

for each fermion, f. The introduction of fermion mass through the Higgs mechanism is not particularly satisfying. It has simply traded a table of masses that are unknown from first principles for a table of Yukawa couplings that are unknown from first principles. Further, expressing the fermion masses as Yukawa couplings, implies that naively, all of these masses should be of a similar scale to the W and Z boson masses. A more natural explanation of flavor physics would require some larger theory, e.g., [29].

Whether the new particle observed at 125 GeV is a fundamental, unique, scalar Higgs boson or not, there is compelling reason to look closely at the electroweak sector as it is explored by the Large Hadron Collider. The scale of electroweak symmetry breaking is precisely at the energies that this experiment will consider. Further, in the absence of a Higgs boson below ~ 1 TeV, the scattering amplitude for $WW \to WW$ events would violate unitarity, bringing a need for some other physics to tame this divergence. Moreover, the elegant pieces of the electroweak symmetry breaking lie in the treatment of the weak vector bosons, and not the fermions. Therefore, it is useful to look for new physics in signatures associated with the weak vector bosons, at the energies probed by the LHC. The remainder of this section discusses such models.

[2]If new physics does only exist at the Planck scale, it has been suggested [28] that naked singularities could be used to accelerate particles to an appropriate energy. No serious endeavor has been made to build such an accelerator.

2.2.1 Technicolor

One attempt to deal with the problems of a single, scalar Higgs, is to suppose that Higgs is not fundamental. Instead, it is made of constituents like those of the Standard Model that experience some new strong force which confines them. With the obvious analogy to the color interactions of the strong force, such models are referred to as "technicolor" [30]. The idea of spontaneous symmetry breaking via composite particles is not novel. It is, for example spontaneous symmetry breaking by Cooper-pairs of electrons that is associated with superconductivity.

QCD is an useful place to start in a discussion of technicolor. It can be shown [3] that even with no Higgs field, the $SU(2) \otimes U(1)$ gauge symmetry of the Standard Model is broken by the strong sector, through the term

$$\langle \bar{q}_L q_R \rangle =\sim 100 \text{ MeV}. \tag{2.12}$$

This vacuum expectation value behaves precisely like the Higgs vacuum expectation value above, except that it would give us a W boson mass of 29 MeV. Still, this points to an obvious process and scale that can be used to dynamically break the electroweak symmetry.

More specifically, technicolor introduces a new set of fermions that are electroweak doublets that also engage in some new force, obeying a new gauge symmetry consistent with asymptotic freedom [31]:

$$\begin{pmatrix} U \\ D \end{pmatrix}_L, U_R, D_R. \tag{2.13}$$

The $\langle \bar{U}_L U_R \rangle$ vacuum expectation value should scale with the strength of the new strongly interacting sector. To reproduce the known vacuum expectation value for electroweak symmetry breaking:

$$\frac{\Lambda_{TC}}{\Lambda_{QCD}} \sim \frac{246\text{GeV}}{100\text{MeV}}, \tag{2.14}$$

where Λ_{TC} is the scale where the new techniforce becomes strong. At this scale, the presence of a strongly coupled theory can appear as a host of resonances, corresponding to technimeson and technibaryon states, in precisely the same way that the strongly coupled region of QCD gives rise to a host of mesons and baryons. In such a model, a vector technimeson can decay resonantly to a W and Z boson, as shown in Figure 2.4.

This explanation provides a mechanism for breaking the electroweak symmetry, and thus generating mass for the weak gauge bosons. It must further have some mechanism to generate the masses of the fundamental fermions. This can be done in *extended technicolor*, models [32], where a series of successively broken symmetries give rise to a series of mass scales for the fermions, although the large top quark mass can make the process more difficult.

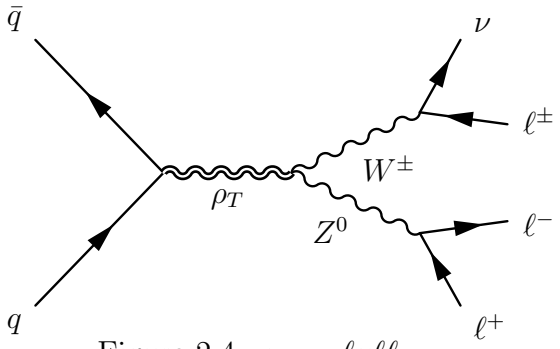

Figure 2.4: $\rho_T \to \ell\nu\ell\ell$

Walking Technicolor

The observation of a new particle at 125 GeV, not inconsistent with the Standard Model Higgs boson, immediately raises the question of whether or not such a particle is consistent with this technicolor framework. Several models have been proposed, [33] [34] in which the technicolor Higgs is consistent with this mass scale, e.g., because quantum corrections to the technicolor Higgs mass bring its mass significantly below the Λ_{TC}. These models are examples of *walking technicolor*, where the running of the technicolor gauge couplings is, in for some scales, very slow. A qualitative sketch of the technicolor coupling in such a model as compared to QCD-like technicolor behavior is shown in Figure 2.5. Such an approach is also more able to handle some of the constraints on technicolor imposed by precision electroweak measurements.

The mechanics of walking technicolor require a large number of technifermions to properly adjust the scaling of the technicolor gauge coupling. As discussed above, the vacuum expectation value of these technifermions is what breaks the electroweak symmetry in a technicolor model. Because each added technifermion will contribute to the vacuum expectation value, as the number of technifermions increases, the necessary contribution of each decreases. In a model with many technifermions, Λ_{TC} could be brought down significantly. Models of this sort are referred to as *low-scale technicolor*.

2.2.2 Little Higgs

Little Higgs models attempt to solve a problem of the Standard Model hinted at above. While quantum corrections to masses of the fundamental gauge bosons and fermions depend on the logarithm of the scale involved, quantum corrections to a scalar Higgs would depend on the square of the scale involved. Although these scales are not accessed by experiment, nature cares about physics up to, at least, the Planck mass at 10^{19} GeV. While logarithmic quantum corrections between Λ_{EW} and Λ_{Planck} are tolerable, quadratic corrections over this range would require very precise tuning to get $m(H)^2_{bare} + O(\Lambda^2_{Planck}) = O(100\text{ GeV})^2$. This fine tuning is known as the *hierarchy problem*.

Little Higgs models solve this problem by introducing at least two new symmetries that are collectively broken to produce a pseudo-Nambu-Goldstone boson, which is observed as

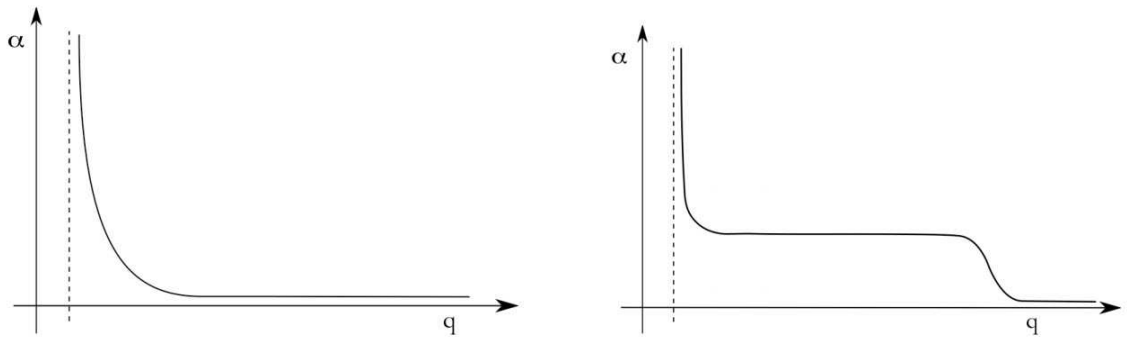

Figure 2.5: The technicolor coupling as a function of energy for a pure QCD analogue (left) and in a walking technicolor scheme (right) [3]

the Higgs[35] [36]. These Nambu-Goldstone bosons are the "degrees of freedom" that were discussed above in the context of the Standard Model Higgs mechanism. The addition of pseudo- here implies that the symmetries that are broken spontaneously are also broken explicitly by some interaction in the model. Adding new symmetries implies new associated gauge bosons. As these symmetries are broken, the gauge bosons can acquire a mass. These heavy gauge bosons can decay into pairs of weak vector bosons, and thus produce a signal $V' \to WZ \to \ell\nu\ell\ell$.

The scale for a Little Higgs theory arises from the need to turn off the unwanted Higgs boson corrections before they become too fine-tuned. Doing so requires this new sector to appear at $\sim$ 10 TeV. In such a model, the heavy gauge bosons could have masses that are O(1 TeV).

2.2.3 Extended Gauge Model

In a general sense, including extra symmetry groups in the Standard Model will bring the possibility of additional, heavy gauge bosons, as these extra symmetries will need to be broken to be consistent with the Standard Model at low energies. A general scheme for parameterizing such heavy gauge bosons can be found in [37].

2.3 Previous Searches

A search for resonant production of WZ rests on a firm understanding of the Standard Model WZ cross section. A measurement of the WZ cross section has been performed by the $D\varnothing$ [38] and CDF [39] collaborations at the Tevatron, where WZ production was first observed, and by the ATLAS [40] and CMS [41] collaborations at the LHC. In all cases, the result was agreed well with the Standard Model. The ATLAS, $D\varnothing$, and CDF results also place limits on anomalous triple gauge couplings, which give a model independent parametrization of

possible new physics in this channel. No significant deviation from the Standard Model was seen in these anomalous triple gauge coupling measurements.

Searches for resonant production of WZ decaying to $\ell\nu\ell\ell$ have been performed previously by the $D\varnothing$ collaboration [42], and by the ATLAS [43] and CMS [44] collaborations at the LHC using data at $\sqrt{s} = 7$ TeV. The most stringent limits were set by the CMS collaboration, using $4.98 fb^{-1}$ of p-p data collected at $\sqrt{s} = 7$ TeV. The CMS result obtained limits on the cross section for a resonance decaying to WZ based on a set of fixed windows in $m(WZ)$, using the number of expected signal and background events in each window. The CMS analysis excludes a W' boson in a Sequential Standard Model scheme (SSM), where the W' coupling to WZ is the same as the W coupling to WZ below 1143 GeV. Interpreted as a Low Scale Technicolor model, the CMS analysis excludes a ρ_T between 167 GeV and 687 GeV for the particular mass scheme $m(\pi_T) = \frac{3}{4}m(\rho_T) - 25$ GeV.

The previous result from the ATLAS experiment used $1.02 fb^{-1}$ of p-p data collected at $\sqrt{s} = 7$ TeV. The ATLAS result obtained limits on the cross section for a resonance decaying to WZ based on a log-likelihood ratio test of the $m_T(WZ)$ distribution for the expected signal and backgrounds. The ATLAS result excludes a W' boson in an Extended Gauge Model scheme (EGM), where the W' coupling to WZ is suppressed by $m_W m_Z / m_{W'}$, below 760 GeV. Interpreted as a Low Scale Technicolor model, the ATLAS analysis excludes a ρ_T between 200 GeV and 467 GeV for the particular mass scheme $m(\pi_T) = m(\rho_T) - m(W)$ and $m(a_T) = 1.1 m(\rho_T)$.

Chapter 3

Experiment and Accelerator

3.1 The Large Hadron Collider

The LHC [7],the world's highest energy particle accelerator, is located near Geneva, Switzerland. Construction of the LHC was approved in December 1994, influenced strongly by the suggestion that the construction of such an accelerator could be done at a manageable cost by re-using the tunnel and injection chain from the Large Electron-Positron (LEP) collider. This decision came in interesting juxtaposition to the fate of the Superconducting Super Collider project, which was canceled a year earlier in part as a result of cost issues. The LHC contains two counter-rotating beams of particles, which intersect at four points around the tunnel circumference. The LHC experiments are then built around these interaction points. The LHC relies on superconducting magnets, cooled to 1.9 K, for the bending and focusing of of the particle beams, and 400 MHz superconducting RF cavities to capture and store the particle beams.

3.1.1 Motivation

By the late 1980s, the Standard Model had provided a simple, elegant description of the known fundamental particles. Three fundamental forces exist: weak, strong, and electromagnetic. These forces are described by gauge theories and mediated by spin-1 gauge bosons. Matter is composed of quarks, which experience all three forces, and leptons, which experience only the weak and electromagnetic forces. Within this framework, nearly three full generations of quarks and leptons had been discovered, along with all of the gauge bosons, including the massive W and Z. The final piece in the third generation of matter, the top quark, would not be discovered until 1995 [19] [18]. In addition, the Standard Model put forward a simple unification of the electromagnetic and weak forces along with a mechanism to break that symmetry and cause the weak gauge bosons to acquire their large mass. Breaking this symmetry through the Higgs mechanism would give rise to at least one new particle, not yet observed. The absence of such a mechanism below 1 TeV would bring about unitarity violation in W-W scattering. With this scale in mind, the development of a hadron collider

with a center of mass energy between 5 and 20 TeV was suggested [30]. The Large Hadron collider is such a collider. With the cancellation of the SSC, it sits at the the energy frontier of collider physics.

3.1.2 Design

The LHC is comprised of 1232 dipole and 392 quadrupole magnets installed in a 26.7 km tunnel underneath the French-Swiss border near Geneva, along with 400 MHz RF cavities, cooling, vacuum, and powering systems. The LHC is designed to accelerate bunches of protons to an energy of up to 7 TeV, corresponding to roughly 3 m/s slower than the speed of light. These bunches can then be collided at a center of mass energy up to $\sqrt{s} = 14$ TeV. The limit on the center of mass energy is driven by the power of the dipole bending magnets in the LHC, which have a peak field of 8.33 T.

Two counter-rotating bunches intersect at four interaction points around the ring. On the site of these interaction points, the ATLAS, CMS, LHCb, and ALICE detectors are built. The LHC is designed to provide a peak luminosity of $L = 10^{34}\text{cm}^{-2}\text{s}^{-1}$ to the ATLAS and CMS experiments and a lower luminosity of $L = 10^{34}\text{cm}^{-2}\text{s}^{-1}$ to the LHCb experiment. This difference in luminosity is accomplished in a single run by variable focusing of the beams as they approach the interaction points. A proton bunch contains up to 1.15×10^{11} protons. At design luminosity, 2808 bunches are circulated in each beam with a spacing of 25 ns.

The LHC can also be used to collide fully stripped lead ions, at a design energy of 2.76 TeV/nucleon and nominal luminosity of $1.0 \times 10^{27}\text{cm}^{-2}\text{s}^{-2}$. The unprecedented energy of the LHC opens significant new ground for studying heavy ion collisions. Collisions of these ion beams are the primary focus of the ALICE experiment, but are also recorded and analyzed by the CMS and ATLAS experiments.

Accelerator performance depends on a cryogenic system to keep the superconducting magnets at 1.9 K. To achieve this cooling, the magnets are immersed in a pressurized bath of superfluid helium. The use of superfluid helium ensures excellent heat transfer across the electrical insulation. An excellent vacuum is required for good beam performance and lifetime. At room temperature, the LHC beam would be subjected to an equivalent vacuum of 10^{-10} mbar. The beam vacuum during operation is subjected to 1.9 K cryogenic temperatures.

Safe operation of the LHC relies on a dependable beam dumping system to avoid loss of the beam into the LHC or LHC experiments. The beam dump system is designed not to exceed one failure in 10^6 hours of operation, roughly 100 years. The beam dump system is comprised of 15 kicker magnets 15 septum magnets to deflect the beam horizontally and vertically away from the LHC machine. Ten dilution magnets are then used to spread the beam before it is absorbed by an assembly of steel and concrete.

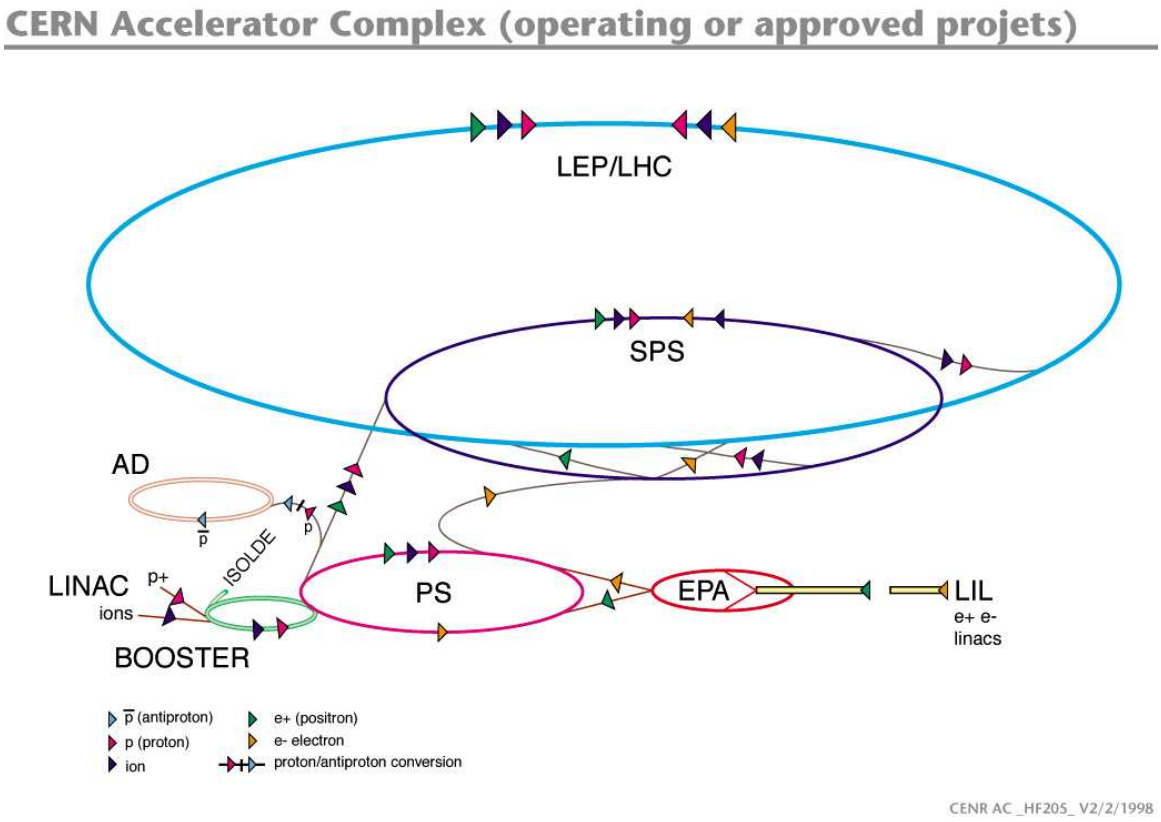

Figure 3.1: The LHC is the last ring in a chain of particle accelerators. The smaller machines are used in a chain to help boost the particles to their final energies [4].

3.1.3 Accelerator Chain

The LHC accelerator chain begins with a bottle of hydrogen. Hydrogen gas is stripped of its electrons and passed into a series of increasingly powerful accelerators, each serving as the injection mechanism for the next. An illustration of the LHC injection chain is shown in Figure 3.1. A full description of the LHC injection chain can be found at [45]

The hydrogen gas is passed into a duoplasmatron ion source where atoms are ionized into electrons and protons. The protons are then injected into the LINAC2 accelerator. The LINAC2 is a linear accelerator that boosts protons from an injection energy of 10 keV to 50 MeV. These protons are then injected into the Proton Synchrotron Booster (PSB), the first in a series of circular synchrotron accelerators that use a fixed path and tunable magnetic field to hold and accelerate the beam. The PSB accelerates proton bunches to 1.4 GeV and injects them into the Proton Synchrotron (PS). The PS is 630 m circumference synchrotron that further accelerates proton bunches to 25 GeV. The PS and PSB establish the 25 ns bunch structure that is seen in the LHC. In nominal operation, 6 bunches in the PSB are split into 18 bunches in the PS on injection. These 18 bunches are then further split into

72 bunches after the beam energy has been brought up to the full 25 GeV. Bunches ride in the minimum of an electromagnetic wave in the RF cavities. A modulation of the frequency inside this RF cavity is used to add energy to the bunches. Protons from the PS are then injected into the Super Proton Synchrotron (SPS). The SPS is the penultimate accelerator in the LHC chain, a synchrotron with a 7 km circumference that brings the bunches from 25 GeV to 450 GeV. It was at the SPS that the W and Z bosons were first observed in the UA1 and UA2 experiments. Unlike the LHC, which relies on the large fields possible in superconducting magnets, the PSB, PS, and SPS use room-temperature magnets to focus and bend the proton beams.

The bunch structure described above also contains a 320 ns gap, originating from a single empty bucket at the PS injection. This gap is necessary to ensure that, when the beam is dumped, the kicker magnet has sufficient time to turn on and eject the beam from the LHC ring. The structure of 72 bunches spaced every 25 ns, followed by a 320 ns, 12 bunch, gap provides a series of bunch trains that circulate in the LHC. In nominal operation, 3564 ns buckets are available in the LHC ring, of which 2808 are filled with protons.

3.1.4 Magnets

The beam energy at the LHC is limited by the bending power of the magnets in the complex. To achieve the unprecedented energies seen in this collider, electromagnets based on superconducting niobium-titanium (NbTi) Rutherford cables cooled to 1.9 K using superfluid helium are used to achieve magnetic fields in excess of 8 T. Although the use of NbTi superconducting magnets is not novel, previous experiments including the Tevatron and RHIC operated at 4.2 K, cooled by supercritical, rather than superfluid, helium, and saw magnetic fields around 5 T.

Design of the LHC magnets was further influenced by the limited space available in the tunnel. This constraint lead to the development of a "two-in-one" design [46], placing two beam pipes in the same cryostat with the magnetic flux circulating in opposite orientations through the two pipes. A cross section of a LHC dipole magnet is shown in Figure 3.2.

Successful operation of the LHC also requires highly uniform magnet performance. The integrated field and field shape are designed to see variance $\sim 10^{-4}$ during magnet operation and a reproducibility better than 10^{-4}. The magnets themselves require a high degree of structural stability to withstand the cooling from room temperature to 1.9 K. This structural stability is achieved, in part, by the use of a rigid collar to pre-stress the magnet and surrounding structure.

In addition to the dipole bending magnets, the LHC is lined with quadrupole magnets, used to keep the proton beam focused, and higher order multipole magnets used to correct deviations in the beam. Finally, the section before each interaction point is lined with high precision quadrupoles that are used to focus the beam down from 0.2 mm to 16 microns in the ATLAS and CMS interaction points.

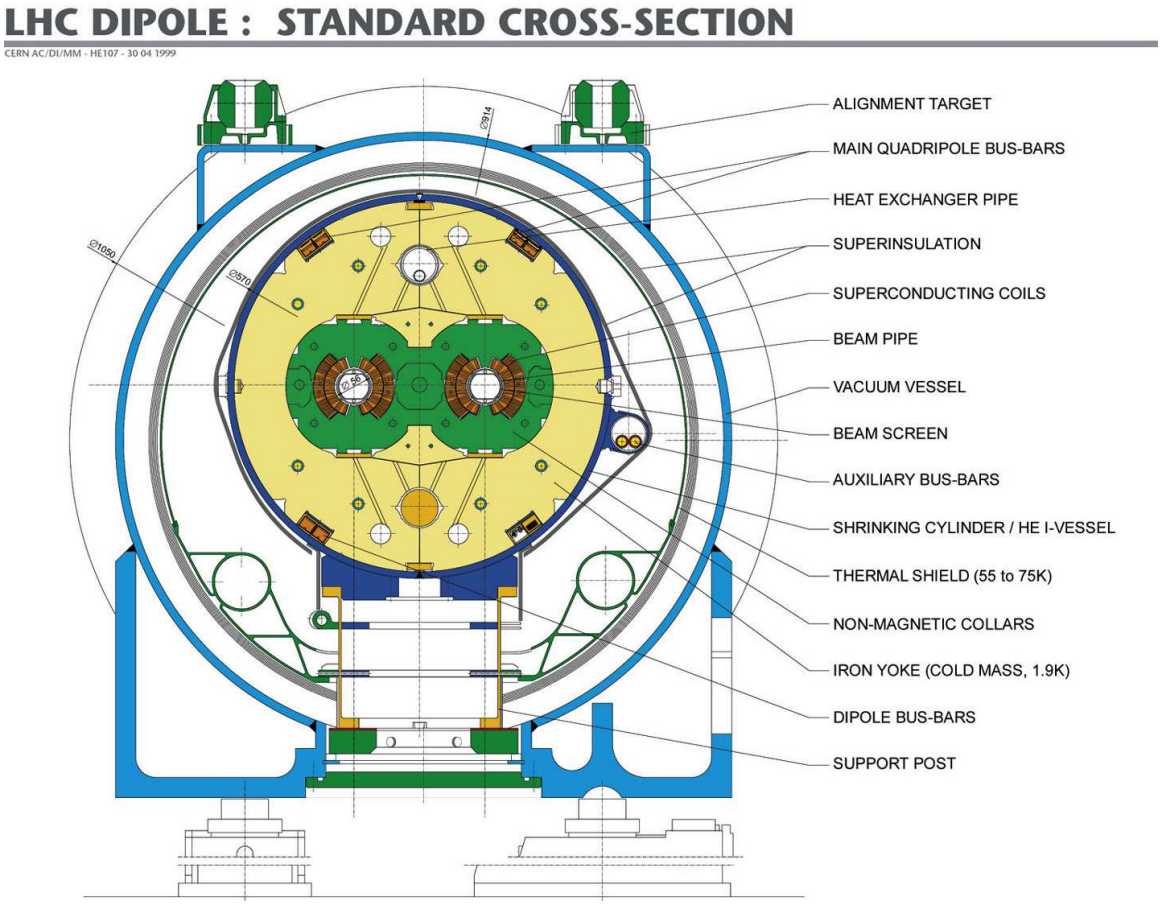

Figure 3.2: Diagram showing the cross-section of an LHC dipole magnet with cold mass and vacuum chamber. [5]

3.1.5 Luminosity

The luminosity of the LHC is a measure of the rate of proton-proton collisions. For specific processes, x, the expected rate is:

$$N_{=} L\sigma_x \tag{3.1}$$

where L is the luminosity and σ_x is the cross section for the process in question. of the luminosity can be increased either by colliding more protons, colliding a fixed number more frequently, or narrowing the colliding bunches so that a collision is more likely. Specifically, the luminosity can be extracted from the beam parameters as:

$$L = \frac{N_{\mathrm{b}}^2 n_b f_{\mathrm{rev}} \gamma_{\mathrm{r}}}{4\pi\epsilon_{\mathrm{n}}\beta_*} F, \tag{3.2}$$

where N_b is the number of particles in a bunch, $n_{\rm b}$ is the number of bunches in the beam, $f_{\rm rev}$ is the revolution frequency, $\gamma_{\rm r}$ is the usual relativistic Lorentz-factor, $\epsilon_{\rm n}$ is the transverse beam emmitence, a measure of the spread of particle momenta and energy in the beam, $\beta*$ is the size of the envelope of beam trajectories at the interaction point, and F is a geometric correction, accounting for the non-zero crossing angle between the two beams at the interaction point. This crossing angle is necessary to prevent "parasitic collisions" between unintended bunches. The luminosity can be written more geometrically as:

$$L = \frac{N_{\rm b}^2 n_{\rm b} f_{\rm rev}}{4\pi \Sigma_{\rm x} \Sigma_{\rm y}} F, \tag{3.3}$$

where $\Sigma_{\rm beam,x}$ and $\Sigma_{\rm beam,y}$ are the widths of the beam profile in the two directions transverse to the beam. For identical Gaussian beam profiles that collide head-on, the interaction region width is related to the beam width as $\Sigma_{\rm int} = \sqrt{2}\Sigma_{\rm beam}$. At design luminosity of $L = 10^{34}{\rm cm}^{-2}{\rm s}^{-1}$, these parameters are: $N_{\rm b} = 1.2 \times 10^{11}$ protons per bunch, with $n_{\rm b} = 2808$ bunches, circulating at $f_{\rm rev} = 11245$ Hz and colliding with beam spot size $\Sigma_{\rm beam,x}, \Sigma_{\rm beam,y} = 16\mu$m.

3.1.6 2012 Run Conditions

Proton beams were first circulated in the LHC on September 10, 2008 at the injection energy of 450 GeV. On September 19, 2008, during powering tests of a section of the LHC, a quench developed in a region between two magnets called a "bus bar splice" [47]. The quench is believed to have occurred because of faulty welding in the splice. This region was not monitored by the quench protection system (QPS.) The resulting arc ruptured the helium enclosure and cryostat. The helium that escaped into the insulation volume caused a rapid increase in pressure that damaged magnets and support structures along 755 m of the LHC tunnel. Repair of the damaged magnets and analysis of the incident delayed first collisions in the LHC until November 23, 2009. During this time the QPS was upgraded to prevent another such incident and other bus bar splices were examined and fixed, as necessary.

A number of further improvements to the LHC and QPS were deemed necessary to proceed to design energy [48]. In 2010 the machine began running at a reduced center-of-mass energy of 7 TeV. Experience with the machine in 2010 and 2011, and an updated analysis of the risks involved motivated an increase to a center-of-mass energy of 8 TeV in 2012 [49]. During the long shutdown between 2013 and 2014, the remaining improvements the QPS, magnets, and splices will be completed and the LHC is expected to restart with a center-of-mass-energy of 13 TeV in 2015.

The data analyzed in this dissertation correspond to an integrated luminosity $\mathcal{L} = \int L dt$ of 13.0 fb^{-1} taken between April and September in 2012 at a center of mass energy of $\sqrt{s} = 8$ TeV. During this period, the peak luminosity observed was $\sim 7 \times 10^{33}$ cm^{-2}s^{-1}. In a representative run, 1368 colliding bunches each containing $\sim 1.5 \times 10^{11}$ protons were circulated with a 50 ns spacing. At collision the transverse size of the interaction was measured to be ~ 15 μm, in the x and y directions. The evolution of the integrated luminosity

during the 2012 run is shown in Figure 3.3. During this time, an average of 20 proton-proton interactions were expected during every bunch crossing. Most of these interactions were present only as background to the more rare collisions.

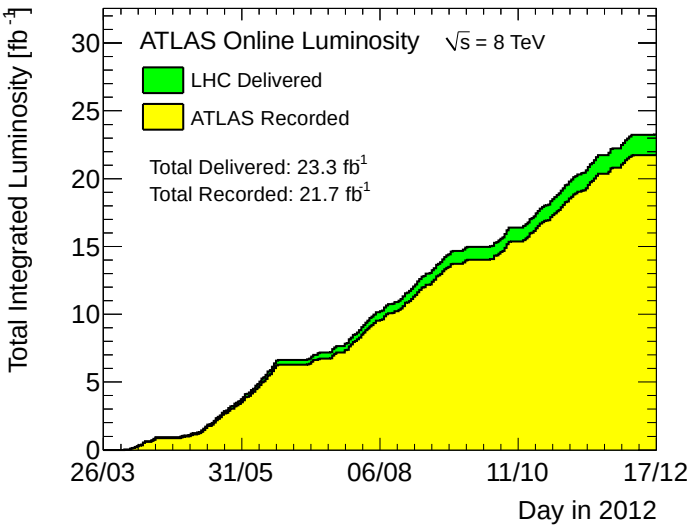

Figure 3.3: Cumulative luminosity delivered by the LHC and recorded by the ATLAS detector as a function of day in 2012 [6]

3.1.7 Experiments

A number of detector experiments are installed at the LHC. The layout of those experiments is shown in Figure 3.4. These experiments aim to reconstruct remnants of the proton-proton collisions that occur at the interaction points and look for the signatures of known, and potentially not-yet-known particles. The major LHC experiments are:

- **A T**oroidal **L**HC apparatu**S**[8]: A general-purpose detector built to provide hermetic coverage of particles originating from the IP and capable of resolving particle energies from hundreds of MeV to several TeV. ATLAS was built not to look for a single phenomenon, but rather to be sensitive to as wide a range of existing and new physics as possible. The eponymous toroids here are the toroidal superconducting magnets, used to bend muons, which pass through the rest of the detector.

- **C**ompact **M**uon **S**olenoid [50]: Also a general-purpose detector, built to probe a wide range of physics by reconstructing particles over a large range of directions and energies. The solenoid here refers to the superconducting magnet used to bend particles as they travel away from the interaction point.

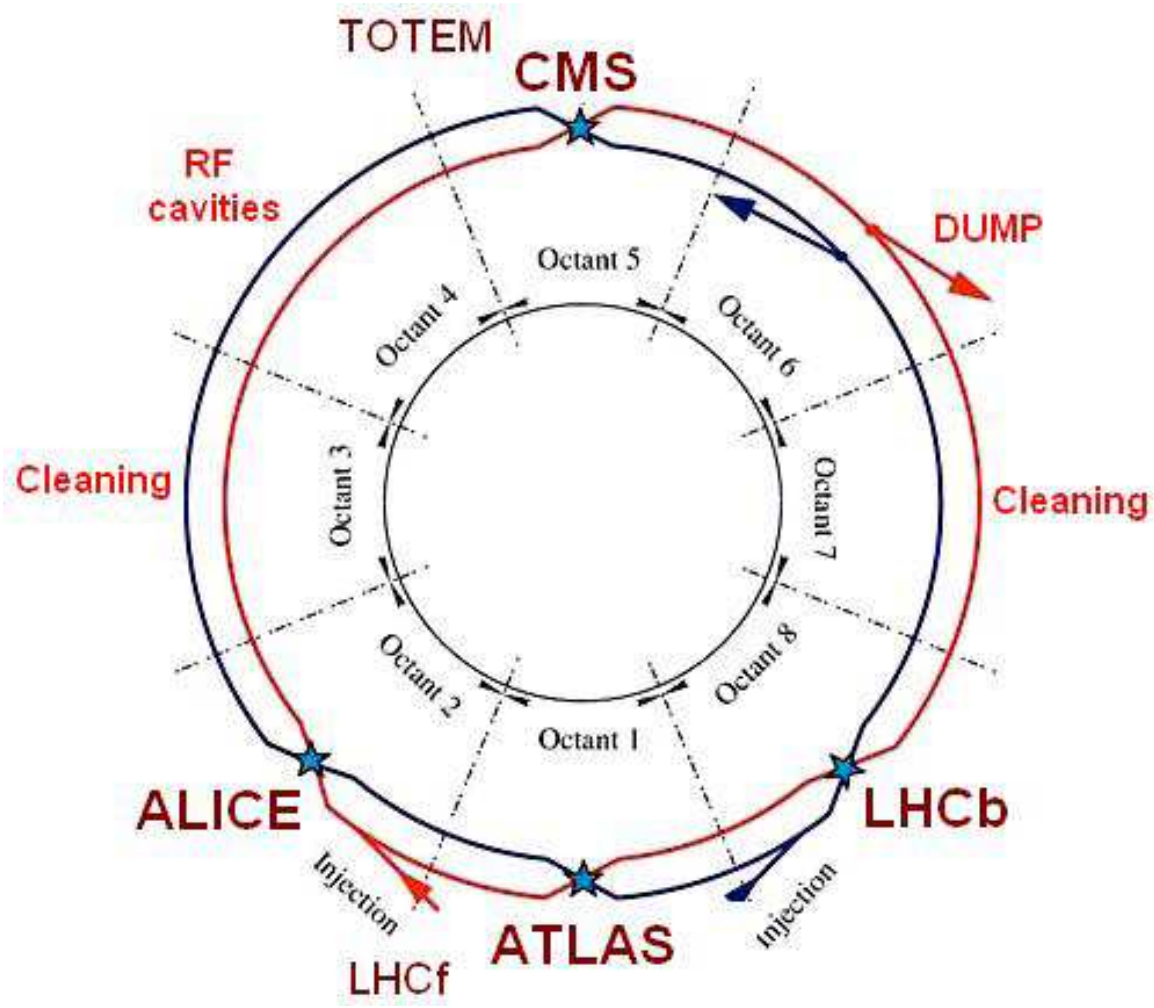

Figure 3.4: A schematic layout of the LHC with the various experiments [7]

- **L**arge **H**adron **C**ollider **b**eauty [51]: An asymmetric detector built exceptional forward coverage of events. This asymmetric design is provides improved performance in events with b-quarks, which will tend to travel a measurable distance before decaying, and produce a secondary vertex that reconstructed particles originate from.
- **A** **L**arge **I**on **C**ollider **E**xperiment [52]: An experiment built specifically to study the heavy ion collisions produced at the LHC. ALICE is designed to handle the tremendous density of particles that are produced in ion-ion collisions.

In addition to these four major experiments, a number of smaller experiments are also built along the LHC and designed with more focused research goals.

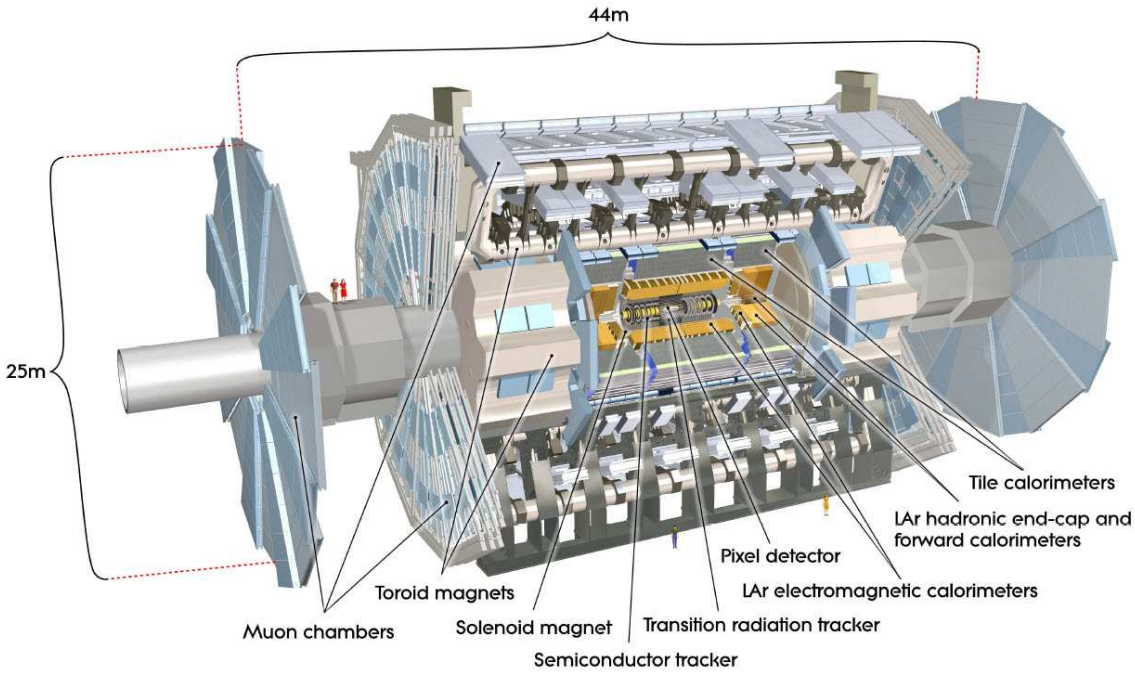

Figure 3.5: A schematic layout of the ATLAS detector with the various subdetectors [8]

3.2 The ATLAS Detector

ATLAS is composed of a set of concentric subdetectors, built outwards from the interaction point [8]. Immediately outside interaction point and beam pipe is the Inner Detector (ID), built to measure charged particle momenta and trajectories as these particles travel out from the interaction point. The ID consists of the Pixel Detector, the Semi-Conductor Tracker (SCT,) and the Transition Radiation Tracker (TRT). Around the ID is the calorimeter system, which is designed to stop electromagnetically and hadronically interacting particles, and measure their energy. Outside the calorimeters is the Muon System (MS), designed to measure the momenta of muons as they escape the calorimeters and leave the detector. A schematic drawing of the full ATLAS detector is shown in Figure 3.5.

In addition to the individual subdetectors, ATLAS relies on a powerful magnet system to bend charge particles and allow for momentum measurement; a trigger system, which can select 200 Hz of interesting events from a 400 MHz collision rate; and a number of specialized detectors to accurately measure the luminosity.

3.2.1 Coordinates

ATLAS uses a right-handed Cartesian coordinate system with its origin at the nominal interaction point in the center of the detector and the z-axis along the beam pipe. The x-axis points from the IP to the center of the LHC ring and the y-axis points upward.

Cylindrical coordinates (r, ϕ) are used in the transverse (x, y) plane, with ϕ the azimuthal angle around the beam pipe. The pseudorapidity is defined in terms of the polar angle θ as $\eta = -\ln\tan(\theta/2)$. The rapidity of a particle is defined in terms of the 4-momentum as $y = \frac{1}{2}\ln\frac{E+p_z}{E-p_z}$, where E and p_z are the particle's total energy and momentum along the z-axis. For a massless particle pseudorapidity and rapidity are the same. The purely geometric definition of the former makes it useful for discussing detector response, while the notion of rapidity is useful for characterizing the behavior of particles with momenta comparable to their mass.

3.2.2 Inner Detector

The ID, shown in Figure 3.6 is the innermost layer of the ATLAS detector. Immersed in a 2 T magnetic field, the ID measures the curved trajectories of charged particles. This detector is used to reconstruct charged particle momenta from particle trajectories. These trajectories can be used to reconstruct the primary vertex coming from collision at the interaction point. The ID can track charged particles down to 0.1 GeV over a wider range of angles, out to $|\eta| < 2.5$.

Because of its close proximity to the interaction point, the ID is subject to a significant radiation flux. The resulting damage to the detector is mitigated by the use of radiation hard sensors, the planned insertion of a supplementary innermost layer, and the operation of the more vulnerable elements at -5 to -10 °C. Finally, the design of the ID is balanced between a need for structural stability to ensure that detector positions are precisely known and a low material budget to reduce multiple scattering.

Pixel Detector

As the detector closest to the interaction point, the Pixel Detector [53] is subject to the strictest requirements on radiation hardness, occupancy, and precision. Each Pixel Detector element is a small patch of semiconducting doped silicon, put into reverse bias and attached to instrumentation. When a charged particle traverses the silicon, it leaves a trail of ionization that is then collected and measured.

Pixel sensors are built from 250 μm thick n-type bulk silicon with high positive and negative dose regions on each side of the wafer. An asymmetric depletion region in the p-n junction operates in reverse bias and extends over the bulk volume. The bias voltage required is 150 V at installation, but ion deposition from radiation will increase the necessary voltage, up to 600 V, and eventually turn the n-type bulk into a p-type bulk. Even after type-inversion, the sensor can still operate successfully. Oxygen impurities are introduced into the bulk during fabrication to increase radiation tolerance. The Pixel Detector consists of approximately 80 million pixels arranged into 1774 identical pixel sensors. The majority of pixels have a size of 50×400 μm^2. The size of the remaining pixels, located near the front-end chips of each module, is 50×600 μm^2. The anisotropic size of the pixel modules is a result of the need for excellent spatial resolution in the bending plane of the ID magnetic field,

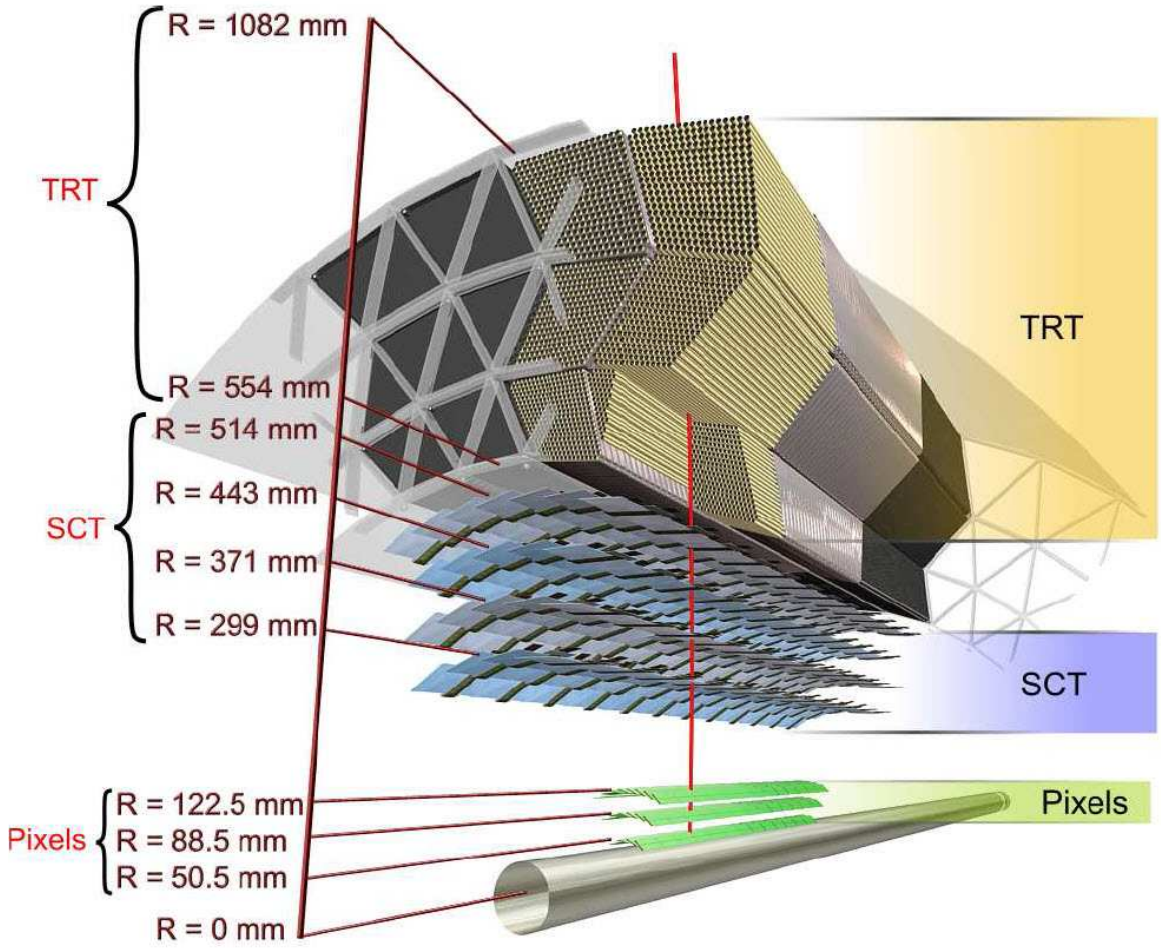

Figure 3.6: A cutaway of the ATLAS Inner Detector in the barrel region[8]

but looser tolerances in the z direction due to the widely spaced distribution of interaction vertices in that direction.

A pixel module consists of, from bottom up: a set of front end chips to handle the electronics readout; bump bonds that connect the electronics to the sensor elements; the sensor tile itself, described above; and a flexible printed circuit board with a module control chip glued to it. Hits in the pixel detector are read out if the collected charge exceeds a pre-defined limit measured by a comparator. The time that the signal is above threshold is related to the amount of charge deposited. The nominal threshold is ~ 3500 electrons. A minimally ionizing particle is expected to leave $\sim 20,000$ electrons.

The 1774 modules of the pixel detector are arranged into three barrel layers and two endcaps with three disk layers each. The barrel layers are located at a radius of 50.5 mm, 88.5 mm, and 122.5 mm from the beam, respectively. The endcap layers are located at a distance along the z-direction of 495 mm, 580 mm, and 650 mm, respectively. The pixel

detector provides tracking out to $|\eta| < 2.5$ around the full azimuthal angle.

The pixel modules have an intrinsic resolution of 10 μm in the transverse direction and 115 μm in the longitudinal direction. No significant degradation of this performance is seen in irradiated elements. Even so, potential degradation due to radiation damage will force the insertion of a new layer during the 2013-2014 shutdown. This new Insertible B-Layer has even greater radiation hardness and uses an even smaller feature size. It will be used to compliment the current three pixel layers.

Semi-Conductor Tracker

The Semi-Conductor Tracker (SCT) is the next detector outside the Pixel Detector. Because of the larger distance from the interaction point and the larger area needed to build a hermetic subdetector at that distance, the SCT uses silicon microstrip sensors to reduce the necessary channel count. The microstrip sensors still must handle a significant radiation fluence and provide excellent spatial resolution for good track momentum reconstruction.

The SCT sensors use standard p-in-n silicon with a thickness of 285 μm using AC-coupled readout strips. Like the Pixel Detector, the SCT will initially be operated at 150 V bias, which will increase to 350 V as ion deposition from radiation degrades the semiconductor bulk. The SCT contains 15,912 sensors arranged in 4088 modules. Each sensor has a pitch of ~ 80 μm and a length of 6 cm. The lower occupancy requirements, resulting from the larger distance form the interaction point, allow long strip design in the SCT. Good resolution in ϕ, resulting from the small strip pitch, is still needed to ensure excellent momentum resolution.

The SCT modules are arranged in four barrel layers at a radius of 284 mm, 355 mm, 427 mm, and 498 mm. There are nine SCT endcap disks between 853 mm and 2708 mm along the z direction. This arrangement provides coverage out to $|\eta| < 2.5$, ensuring at least four high quality space point hits for any charged particle passing through the tracking volume. The SCT modules are arranged in double layers with a small stereo angle between the two layers to allow for better space point measurement in two dimensions. Sets of four sensors are glued to a graphite baseboard, which provides the thermal and mechanical structure.

A SCT module has a spatial resolution of $\sim$16 μm in the transverse direction, and this performance remains consistent after module irradiation. Modules irradiated with the equivalent of three years of nominal running maintained stable operation at 350 V bias voltage with $< 1\%$ bad readout strips.

Transition Radiation Tracker

Outside the SCT, the Transition Radiation Tracker (TRT) [54] is an array of thin-walled proportional drift tubes, called "straws," interleaved with a transition radiation material. The larger distance from the interaction point allows the TRT to operate with less concern for occupancy and radiation hardness, but limits the cost per unit volume. The TRT extends the silicon detector tracks, with an average of 36 straws crossed by a particle as it travels

through the TRT. The use of transition radiation material allows the detector to distinguish electron and pion tracks.

Drift tube detectors detect particles by measuring the ionization trail left as a charged particle passes through a medium. In a drift tube, a high voltage is applied via a wire across a gaseous enclosure with the walls held at ground. The large potential accelerates the ionized particles through the gas causing further ionization. This cascade continues until it reaches the wire, where the charge from the cascade is collected. The charge collected is a measurement of the amount of ionization from the original track.

TRT straws are 4 mm-diameter polymide tubes filled with 70% Xe, 27% CO_2, and 3% O_2. This gas mixture was chosen to ensure efficient transition radiation absorption, high electron drift velocity, and good aging resistance. The straws are designed to ensure good electrical and mechanical properties with minimal wall thickness. The tube walls are made of 25 μm thick polymide film, coated on one side with a thin Al layer protected by a graphite-polymide layer. The other side is coated in polyurethane to seal the film. The straws are mechanically stabilized using carbon fibers. The straw anodes are connected directly to the front-end electronics and kept at ground. The anode resistance is $\sim$60 Ω/m. The cathode resistance is $\sim$300 Ω/m and the cathodes are held at $\sim$1500 V.

The TRT straws are interleaved with a transition radiation material. As a charged particle crosses the boundary between two materials with different dielectric constants, it will give off transition radiation. The amount of radiation is proportional to the Lorentz factor γ. Because of the substantial difference in the rest mass between, e.g., electrons and pions, the amount of transition radiation produced can give a measure of the type of charged particle that crossed this material boundary. In the TRT, transition radiation is absorbed by the straw gas mixture, producing further ionization: a "high threshold" hit. The ratio of low to high threshold hits gives a measure of the amount of transition radiation.

The TRT barrel contains up to 73 straw layers interleaved with transition radiation fibers. The barrel sits between a radius of 554 mm and 1082 mm from the beam line. The TRT endcap contains 160 straw planes interleaved with transition radiation foils. The endcaps sit 615 mm and 1106 mm from the interaction point in the z direction. The TRT covers the region $|\eta| < 2.0$. A track passing within this range will traverse at least 36 TRT straws, except in the transition region between the barrel and the endcap at $0.8 < |\eta| < 1.0$.

The spatial resolution of a TRT straw in the transverse direction is 130 μm. To attain this precision requires knowing the TRT wire positions to within 50 μm. Good mechanical operation of the TRT requires that the 72 cm wires sag by less than 15 μm in operation. The reduced radiation dosage in the TRT allows it to operate at room temperature.

3.2.3 Calorimeters

The ATLAS detector contains two sampling calorimeter systems designed to stop electrons, photons, and hadrons, and measure their energies. These calorimeters cover a range out to $|\eta| < 4.9$ using a variety of techniques to address specific physics goals and the varying radiation environment in the various η ranges. The inner, electromagnetic calorimeter has

fine granularity well suited to precision measurements of electrons and photons. The coarser granularity in the hadronic calorimeter is sufficient for the requirements of jet and missing energy reconstruction. The larger η coverage of the calorimeter system compared to the ID reflects the importance of detector hermeticity in reconstructing missing transverse energy, which can be observed only as an overall momentum imbalance in a given event.

In addition to providing good measurements for electrons, photons, and jets, the ATLAS calorimeter system is designed to limit the punch-through of hadrons into the muon system and to ensure that electromagnetic and hadronic showers are well contained. While good tracking performance in the ID relies on limiting the material budget to prevent multiple scattering, good performance in the calorimeters relies on a large material budget to prevent punch-through and contain showers. The calorimeter size in radiation lengths and interaction lengths is shown in Figure 3.7

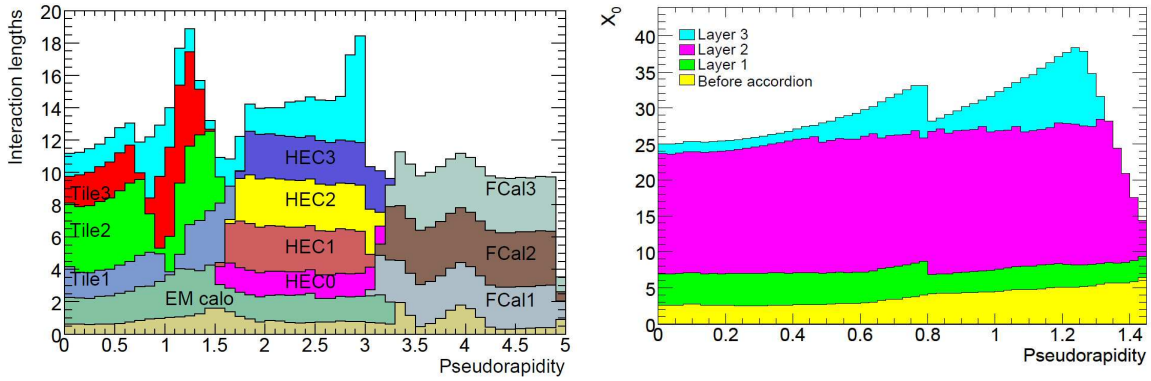

Figure 3.7: Cumulative amounts of material in the ATLAS detector in interaction length, (left) and radiation lengths (right) [8]

Electromagnetic Calorimeter

The ATLAS electromagnetic calorimeter is divided into a barrel section and endcap section. To reduce the material budget in front of the calorimeter, the central solenoid and EM calorimeter barrel share a cryostat, removing the need for separate walls for the two detector pieces. The EM calorimeter uses liquid argon (LAr) as the active material with lead absorber in an accordion geometry. The accordion geometry ensures uniform performance through the detector and fast extraction of the ionization signal at the front or rear of the electrodes.

A charged particle entering the EM calorimeter will produce a shower of electrons and photons. The LAr calorimeter measures the shower energy by collecting the charge at electrodes. Some energy is lost in the lead absorber, but the charge collected is proportional to the energy of the particle that initiated the shower. Although the lead is passive material, it ensures that an electromagnetic shower can be contained in a relatively small space.

The absorbers in the LAr calorimeter are lead plates, 1.13 mm or 1.53 mm thick, to which stainless steel sheets, 0.2 mm thick, are glued to provide mechanical strength. Readout electrodes consisting of three conductive copper layers insulated by polymide sheets are located in the gaps between the absorbers. The electrodes are held at a potential of 2000 V in the barrel and between 900 V to 2500 V in the endcaps, to ensure uniform charge collection. The liquid argon itself is kept at 88.5 K. The temperature-dependent response of the active material requires that this temperature be maintained to within 100 mK [55].

A LAr Calorimeter module is built in three layers, with varying readout granularity based on performance requirements. The first layer has granularity in η of 3.215×10^{-3}, with a depth of 6 X_0. The fine granularity of the first layer is designed to help distinguish electrons from pions. The second layer has a granularity in η of 0.025 with a depth of 6 X_0 to 24 X_0. The third layer has a granularity in η of 0.5 with a depth of 2 X_0. A schematic of the three EM calorimeter layers is shown in Figure 3.8. The coarser granularity at increasing depth is adequate because shower shapes become more diffuse with increasing depth. Additionally, a presampler in front of the first layer of the calorimeter measures and corrects for the energy loss in upstream material.

The EM calorimeter barrel occupies the region $|\eta| < 1.475$. The barrel is made of two half barrels centered around the beamline. Each half-barrel is made of 1024 accordion-shaped absorbers grouped into 16 modules for construction. Each 57 ton half-barrel is held in place with seven stainless-steel outer rings. The endcap calorimeters are two wheels, 63 cm thick, on on each side of the barrel EM calorimeter. The endcaps cover the region $1.375 < |\eta| < 3.2$. Each endcap consists of two 27 ton wheels divided into 8 wedge-shaped modules. Both wheels are supported by a six-ring support frame.

The electromagnetic calorimeter has excellent performance in both energy and spatial resolution. In test beam [56], the measured performance of the EM calorimeter is:

$$\frac{\sigma(E)}{E} = \frac{10\%}{\sqrt{E(\mathrm{GeV})}} \oplus 0.7\%. \tag{3.4}$$

The EM calorimeter is measured to be linear within 1% for clusters down to 10 GeV. The fine granularity in the sampling in the first layer of the EM calorimeter provides a resolution in the η direction of 50 mrad/$\sqrt{E(\mathrm{GeV})}$. This performance required for adequate angular reconstruction of photons in $H \to \gamma\gamma$ searches. Although the EM calorimeter performance is driven by EM shower requirements, the detector has a depth of $\sim 2\ \lambda_0$ interaction lengths. Thus, a significant fraction of jet energy can be deposited in the EM calorimeter. Because some of the jet energy is deposited in the EM calorimeter, this subdetector contributes significantly to jet performance.

Hadronic Calorimeter

The hadronic calorimeters in the ATLAS detector consist of the tile calorimeter [57] in the barrel, the liquid-argon hadronic endcap calorimeter (HEC,) and the liquid-argon forward calorimeter (FCal). The HEC and FCal use copper and tungsten absorbers with liquid argon

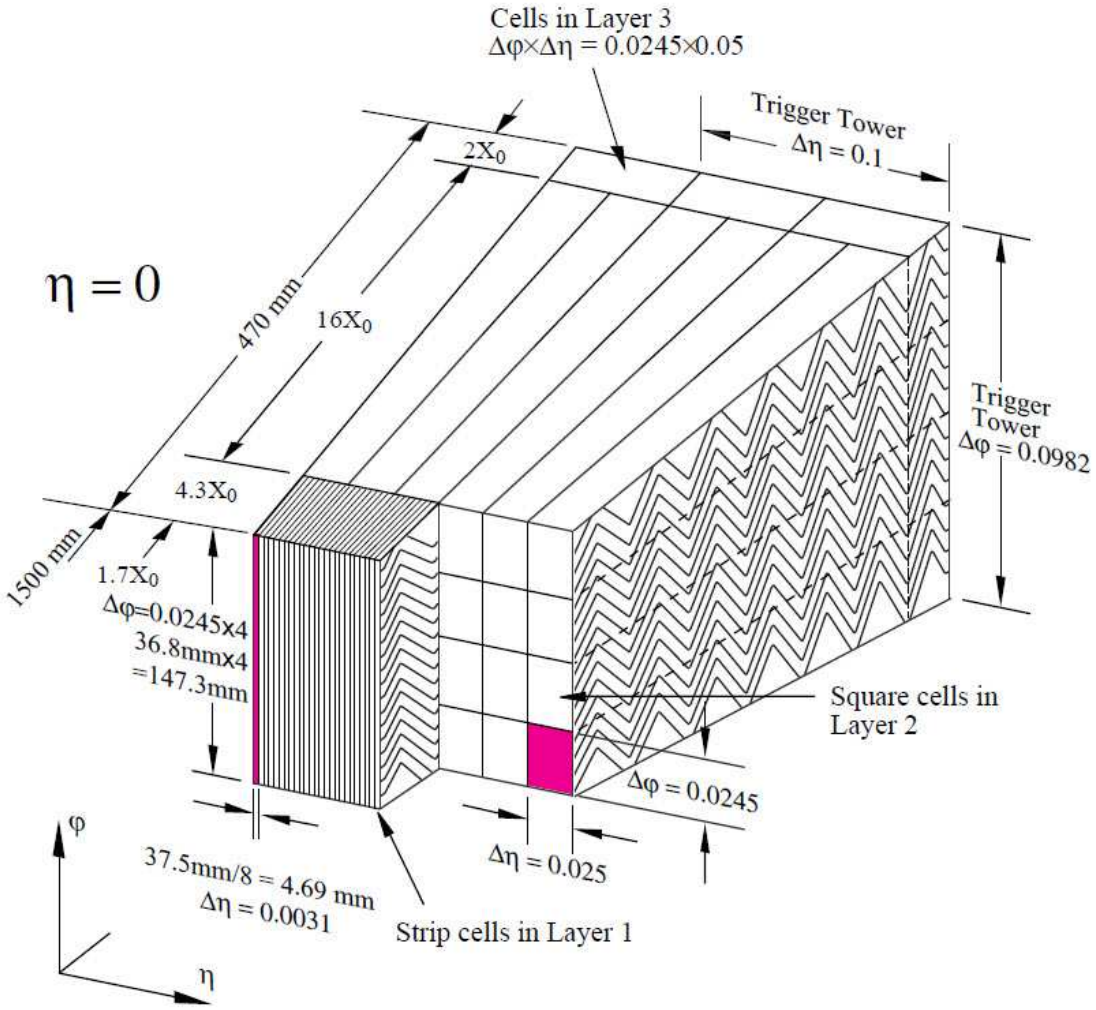

Figure 3.8: A barrel module inside the ATLAS electromagnetic calorimeter [8]

as the active material. The tile calorimeter uses steel absorber with doped polystyrene scintillator as the active medium. The hadronic calorimeters in ATLAS are designed to exhibit good hermeticity, uniformity, linearity, and energy resolution. The steel in the tile calorimeter also provides the flux return for the magnetic field from the central solenoid.

Unlike the LAr calorimeter, which collects the charge left by ionization, the tile calorimeter collects the light produced by the passage of showering particles through the active medium to measure the energy of a shower. This light then passes through wavelength shifting fibers to photomultiplier tubes to be read out. The hadronic showers produced in the tile calorimeter can be complicated and include embedded electromagnetic showers originating from π^0s.

The tile modules are composed of an alternating steel-scintillator structure with a ratio

of 4.7:1. A diagram of that structure is shown in Figure 3.9. Doped polystyrene is used as the scintillation material. The scintillators are enclosed in a reflective plastic sleeve to prevent damage and improve light yield. Wavelength shifting fibers at the edge of the tile collect the ultraviolet scintillation light, convert it to a longer wavelength, and transport it to photomultiplier tubes for readout.

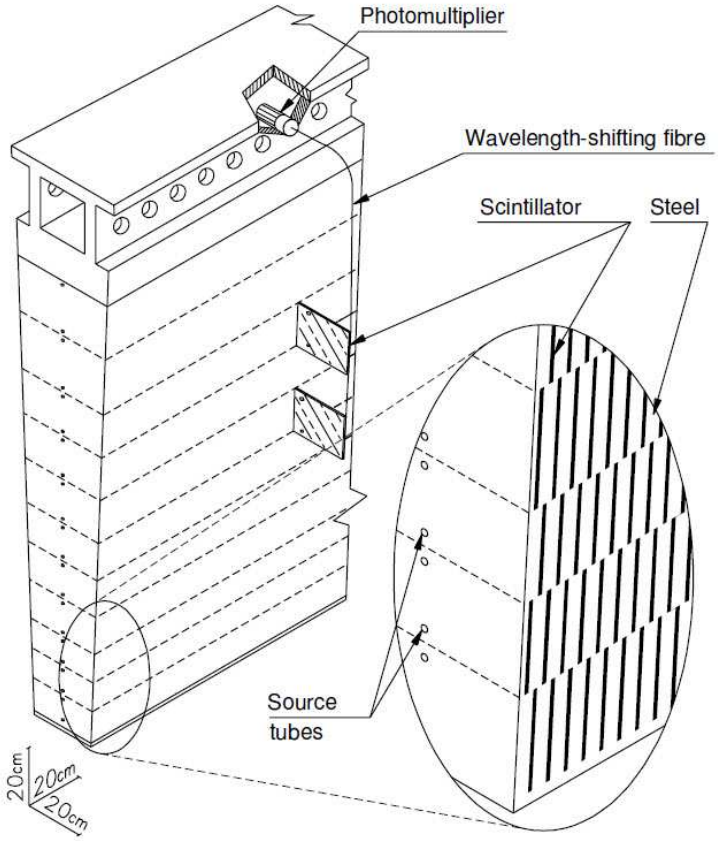

Figure 3.9: A tile drawer inside the ATLAS hadronic calorimeter [8]

The HEC modules are made from 24 copper plates, each 25 mm thick, in the front wheels and 16 copper plates, each 50 mm thick, in the rear wheels. The 8.5 mm gap between plates is divided by electrodes into four LAr drift zones with a 1.8 mm width each. The electrodes provide readout and a 1800 V potential to collect charge deposited in the liquid argon. FCal modules are split into three types, depending on depth. The most forward modules use copper scintillator and are designed to have increased EM shower sensitivity while the back two use tungsten scintillator and are optimized for a high absorption length. High voltage of 250 V to 500 V is used for charge collection in the FCal.

The tile calorimeter covers the range $|\eta| < 1.7$ and is located outside the EM calorimeter. It has an inner radius of 2.28 m and an outer radius of 4.25 m. The tile calorimeter is split into

a barrel with a coverage of $|\eta| < 1.0$ and two extended barrels that cover $0.8 < |\eta| < 1.7$. The tile calorimeter is divided azimuthally into 64 of the modules described above. The HEC calorimeter covers a range between $1.5 < |\eta| < 3.2$, overlapping slightly with both the tile calorimeter and the FCal. Each wheel in the HEC contains 32 identical wedge-shaped modules with two segments in depth per wheel and two wheels per side. The FCal covers the range $3.1 < |\eta| < 4.9$. At such forward pseudorapidity, FCal must be very radiation-hard. It uses only a small amount of liquid argon to prevent ion buildup. The expected performance of the tile calorimeter and HEC with respect to jets is:

$$\frac{\sigma(E)}{E} = \frac{50\%}{\sqrt{E(\text{GeV})}} \oplus 3\%. \tag{3.5}$$

The expected performance of the FCal with respect to jets is:

$$\frac{\sigma(E)}{E} = \frac{100\%}{\sqrt{E(\text{GeV})}} \oplus 10\%. \tag{3.6}$$

The degraded performance of the hadronic calorimeters compared to other detectors is a result of the significant amount of material inside the hadronic calorimeters; the innate difficulty in quantitatively understanding hadronic showers; and the significant volume of such detectors, necessitating a low cost per volume. The granularity of the tile calorimeter in $\eta \times \phi$ space is 0.1×0.1 in most layers. The granularity of the HEC is 0.1×0.1 or 0.2×0.2, depending on η. Although some loss of performance in the scintillation material in the tile calorimeter is expected with radiation damage, the energy resolution should degrade by only $\sim$10% after ten years at nominal operation. No significant damage is expected to the liquid argon calorimeters.

3.2.4 Magnets

The ATLAS magnet system [8] consists of one solenoid [58] and three toroids used bend charged particles as they travel through and out of the detector. A precise understanding of the resulting magnetic field is crucial in mapping particle bending to particle momenta. The solenoid magnet provides a 2 T magnetic field for the ID. The magnet itself is integrated into the EM calorimeter cryostat. The tile calorimeter is used as the flux return for the solenoid field so that the contribution of the this field outside the ID is minimized. The air core toroids provide a 0.5 T field in the barrel and 1 T field in the endcaps for the muon spectrometer. A map of the solenoid and toroid fields is shown in Figure 3.10

In addition to providing a uniform 2 T magnetic field for the ID, the ATLAS solenoid magnet is adheres to a strict material budget to minimize the number of radiation lengths in front of the EM calorimeter. The solenoid consists of from 1154 turns of superconducting NbTi Rutherford cable, stabilized with high-strength aluminum. The cable is mounted inside a 12 mm thick aluminum support cylinder. The full solenoid assembly contributes only 0.66 radiation lengths to the material budget. The central solenoid has a mass of 5.7

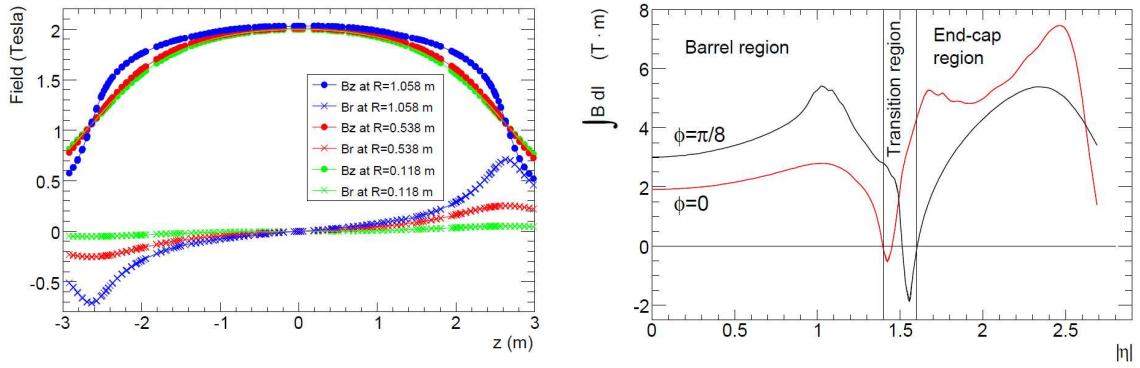

Figure 3.10: A measurement of the magnetic fields used in the ATLAS detector: The solenoid field (left) and the toroid field (right). [8]

tons and a length of 5.8 m. The superconducting material is cooled to 4.5 K using liquid helium. In the event of a magnet quench, the energy stored in the magnets is absorbed by the cold mass, safely raising its temperature to 120 K.

The magnetic field for the muon system is provided by a set of superconducting air core toroid magnets that provide a 0.5 T to 1 T magnetic field used to bend muons that pass through the ATLAS calorimeters. The barrel toroid consists of eight coils with 120 turns each of superconducting NbTi wire encased in individual racetrack-shaped vacuum vessels. The barrel toroid extends from a radius of 4.7 m to 10.1 m and has a mass of 830 tons. Each endcap toroid consists of a single cold mass with eight square 116-turn coils of superconducting NbTi wire and eight keystone wedges held in a rigid structure.. Each endcap has a radius of 5.4 m and a mass of 239 tons. Like the central solenoid, the toroid magnets are cooled to 4.5 K using liquid helium.

3.2.5 Muon System

The ATLAS muon system [59] [60] is encased in the magnetic field provided by the toroid magnets and contains of four different detector technologies. The muon system is designed to detect particles exiting the barrel and endcap calorimeters and measure their momenta. The muon system also provides triggers for such particles. The muon system covers out to $|\eta| < 2.7$ and can trigger on particles out to $|\eta| < 2.4$. The high field, large distance, and low material density in the muon system enable precise momentum measurements up to a few TeV. At these high energies, the significantly smaller ID is less useful at precisely measuring particle momentum.

In the barrel, the muon chambers are arranged into three concentric shells at a radius of 5 m, 7.5 m, and 10 m from the beam. In the endcaps, the muon chambers form large wheels at 7.4 m, 10.8 m, 14 m, and 21.5 m from the interaction point in the z direction. A gap in the muon system at $|\eta| < 0.08$ allows for the placement of services for the solenoid magnet,

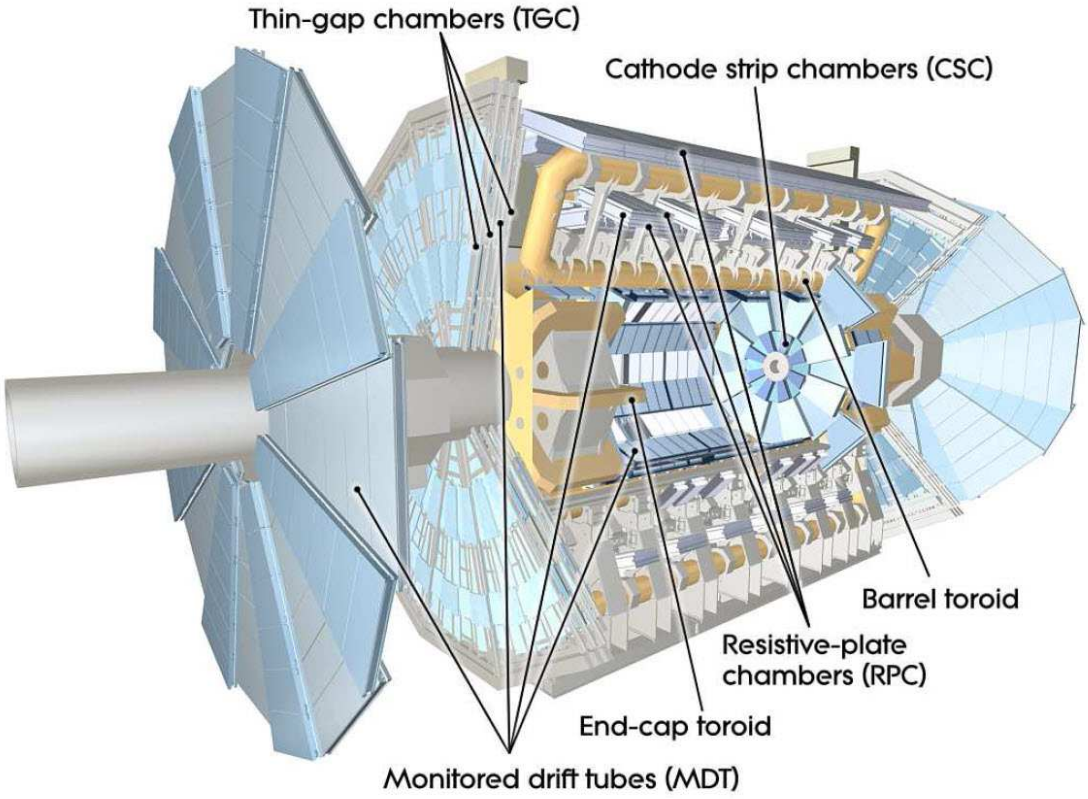

Figure 3.11: A schematic layout of the ATLAS muon system [8]

calorimeters, and ID. An overview of the muon spectrometer is shown in Figure 3.11. The particular geometry can be better seen in Figure 3.12

The precision measurement of muon momenta is performed by Monitored Drift Tube chambers (MDTs), which provide high accuracy and predictability along with good mechanical stability and simple construction, and Cathode-strip Chambers (CSCs), which are used in the innermost layer of the forward region for their ability to tolerate higher rates. MDTs cover out to $|\eta| < 2.7$, except in the innermost endcap layer where the coverage ends at $|\eta| = 2.0$. Each chamber consists of three to eight layers of drift tubes with an average resolution of 80 μm per tube and 35 μm per chamber. CSCs are multiwire proportional chambers, with the wires oriented in the radial direction. This arrangement allows for good resolution in two directions: 60 μm in the bending plane and 5 mm in the transverse plane.

In addition to precision momentum resolution, the muon system contains a system of fast trigger chambers that both record track information and deliver it within $15 - 25$ ns after the passage of a particle. This fast trigger response can identify a particular beam crossing associated with the trigger. In the barrel region, $|\eta| < 1.05$, this fast trigger is provided by Resistive Plate Chambers (RPCs). RPCs are gaseous parallel electrode-plate detectors. In

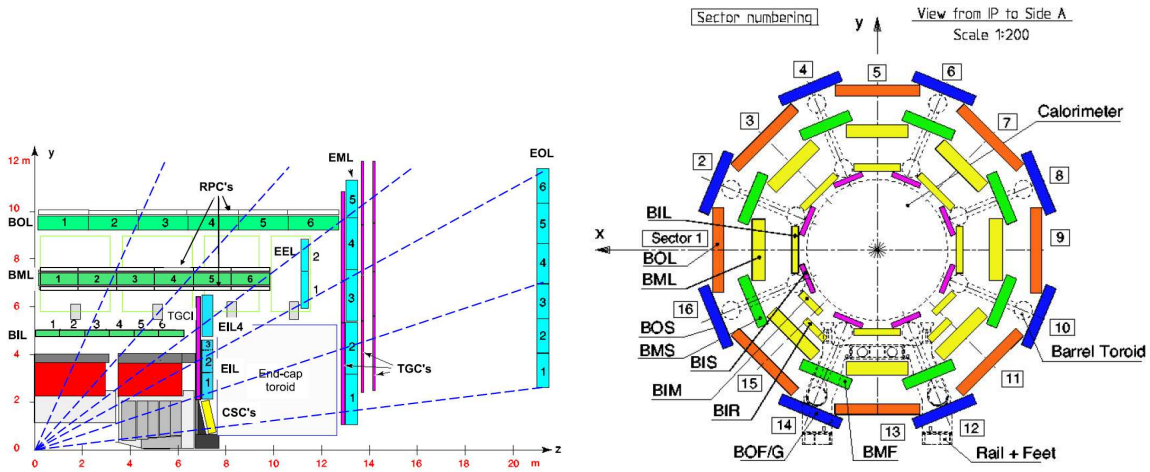

Figure 3.12: A cross sectional view of the ATLAS muon system, transverse to the beam direction (left) A quarter of the ATLAS muon system in the plane containing the beam line (right) [8]

the endcap region, $1.05 < |\eta| < 2.4$, this fast trigger is provided by Thin Gap Chambers (TGCs). TGCs are multiwire proportional chambers, chosen for their better granularity and higher rate tolerance compared to RPCs.

The ATLAS muon system shows excellent performance over its operating range. A muon passing through the muon system has an acceptance of 90% to 96% depending on the strictness of the hit requirements used. The trigger efficiency for the muon system is 80% to 90% for muons with a transverse momentum in the efficiency plateau. The momentum resolution of the muon system is between 3% and 12 %, for muons between 10 GeV and 1 TeV. The finite spatial resolution of the muon detector limits the momentum resolution for the very straight, high-momentum tracks. The muon system is designed for good radiation tolerance. The primary effect of detector irradiation is the introduction of background particles that can reduce track finding efficiency and introduce fake trigger signals. In the barrel, the rates for these background particles is $\sim$10Hz/cm^2, while for the CSCs, this rate can be as high as $\sim$ 300Hz/cm^2

Monitored Drift Tubes

The MDT chambers are arrays of drift tubes. The drift tubes have a diameter of 30 mm and are filled with 93 % Ar, 7% CO_2. Ionization from tracks passing through a tube is collected on a tungsten-rhenium wire held at a potential of 3080 V. The wire is held in the center of the tube by a cylindrical plug. The plug also allows gas transfer in and out of the tube. The tube lengths vary from 70 cm to 630 cm depending on their placement within the muon system. The maximum drift time for electrons within the tube is 700 ns.

Individual drift tubes are arranged in three to eight layers in a MDT chamber. Groups of three or four layers are separated by a mechanical spacer to ensure accurate positioning of the drift tubes. Three-layer groups are used in the middle and outer stations of the muon system, while four-layer groups are used in the inner stations to improve pattern-recognition. Rectangular chambers are used in the barrel and trapezoidal chambers are used in the endcaps to maximize the solid-angle coverage of the chambers.

A precise understanding of the drift time provides a resolution of 80 μm per drift tube in the sensitive direction and no significant resolution in a second coordinate. The combination of up to eight hits in a single chamber provides a combined resolution of up to 30 μm. Radiation damage will degrade MDT resolution by $\sim$ 20 μm. The wires in the drift tubes can sag significantly under the effects of gravity. This sag can be corrected by adjusting the wire tension and is controlled to within 10 μm.

Cathode Strip Chambers

Because MDTs cannot operate in the high rate environment of the first layer of the endcap, Cathode Strip Chambers are used instead. CSCs are multiwire proportional chambers with the anode wires oriented in the radial direction. A CSC chamber contains two cathodes that are segmented and aligned in directions parallel to and perpendicular to the anode wires. The position of a detector hit is determined by interpolating the charge induced on the cathode strips. Thus, the CSC resolution is limited by readout pitch, which is 5.31 mm or 5.56 mm in the precision direction. In the transverse direction, the readout pitch is 12.52 mm or 21.00 mm. The CSCs are operated at 1900 V and with have a maximum drift time of 40 ns, significantly faster than the MDTs. The two dimensional hits in the CSCs allow for the resolution of signal ambiguities when more than one track is present.

The CSCs are grouped into eight large and eight small chambers. Each chamber contains four CSC planes. Each plane gives an independent measurement of the track η and ϕ. CSC chambers are filled with a mixture of 80 % argon, 20 % CO_2. The chambers are spaced around the ϕ coordinate. Each small chamber contains 250 wires and each large chamber contains 402 wires along the bending direction. The 16 chambers are mounted onto a stainless steel frame, 7 m from the interaction point in the z direction.

A hit left in the CSCs deposits charge over several adjacent strips that are then weighted to determine the hit position. This procedure is limited by noise in the pre-amplifiers, so the weighting is performed only over nearby strips. Further contributions to the track resolution come from charge spreading as a result of delta rays, track angle, and the Lorentz force along the wire. The effect of the Lorentz force is minimized for high momentum tracks by tilting the CSCs to be normal to track incidence at infinite momentum. The timing resolution for a single chamber can vary as a result of a non-uniform electric field. By combining the four independent timing measurements for a single chamber, the timing resolution is improved to 3.6 ns, which is sufficient to tag a beam crossing.

Resistive Plate Chambers

Each RPC consists of two resistive plates made of phenolic-melaminic plastic laminate. The plates are held 2 mm from each other by insulating spacers with a mixture of of $C_2H_2F_4$, Iso-C_4H_{10}, and SF_6 gases in between. A 4.9 kV/mm field applied between the plates allows ionizing particles that pass through the chamber to generate an avalanche. The charge from this avalanche is captured at the anode. The resulting signal is read out by capacitive coupling to metallic strips mounted on the outer faces of the plates. The strong, uniform field in the RPCs allows for a clean signal when an ionizing particle traverses the chamber.

Each RPC chamber is built from two detector layers. Each layer provides a measurement of η and ϕ. Each detector layer contains two resistive plates with the spacers and gas volume described above. The two detector layers are each connected to four readout strip panels and supported by three layers for paper honeycomb. Two external support panels give stiffness to the chamber. Each RPC shares a common support structure with an MDT of equal dimensions.

The small drift distance and strong, uniform field ensure that the RPCs have an excellent 7 ns timing resolution. A significant lever arm between inner and outer RPCs allows the trigger to resolve high momentum tracks in the range of 9-35 GeV. A strip pitch of 30 mm in the RPCs provides a spatial resolution of 30 mm in both the η and ϕ directions. No significant radiation damage is expected in the RPCs during detector operation.

Thin Gap Chambers

Unlike a traditional multiwire proportional chamber, TGC modules have a wire to cathode distance, 1.4 mm, shorter than the wire-to-wire distance, 1.8 mm. TGC modules use a highly quenching gas mixture, CO_2 and n-pentane, which allows them to be operated in saturated mode. Operating the TGC modules in saturated mode reduces the sensitivity of the chambers to mechanical deformation, decreases the effect of parallax, and reduces the pulse-height tails of the read-out signal. TGC modules are operated at 2900 V. 99% of signals are picked up by the TGCs within 25 ns. Signals arriving after 25 ns come from tracks that passed at normal incidence precisely between two wires, where the field is at a minimum.

Each endcap has seven TGC layers that are arranged into two doublets and one triplet. The detectors are mounted in two concentric rings: one covering $1.05 < |\eta| < 1.92$ and one covering $1.92 < |\eta| < 2.4$. Each TGC module is sandwiched between two graphite planes. The planes are etched with copper strips to provide readout of the azimuthal coordinate. The planes are spaced from each other by paper honeycomb that protects the modules from gas overpressure.

The TGCs provide sufficient timing resolution to distinguish between bunch crossings at nominal LHC operation. The TGCs also provide two-coordinate hits, with a resolution of 2 to 6 mm in η and 3 to 7 mm in ϕ. No significant degradation of the TGCs is expected in either time resolution or charge per minimum ionizing particle during the detector lifetime.

3.2.6 Trigger

The ATLAS trigger system selects 200 Hz of interesting events from a collision rate of 40 MHz . This filtering of events proceeds in three stages. Each successive stage requires a smaller input event rate, but allows for more information to be used in a trigger decision. These stages are referred to as Level 1 (L1), Level 2 (L2), and Event Filter (EF). The nominal 40 MHz collision rate is reduced to a 75 kHz output rate for the L1 trigger, a 3.5 kHz output rate for the L2 trigger, and a 200 Hz output rate at the Event Filter.

The L1 trigger picks out high transverse momentum muons, electrons, photons, and jets. The L1 trigger also selects events with large missing transverse energy and large total transverse energy. In the calorimeters, the L1 trigger uses reduced-granularity information from all of the subsystems. In the muon system, the L1 trigger uses information from the TGCs and RPCs. The L1 decision is made by the Central Trigger Processor that combines information from various subdetectors. The L1 trigger decision is based on a menu of discrete flags for particular detector objects and energy thresholds. More detailed information about events is stored in the muon and calorimeter trigger processors and is used in a L2 trigger decision if the L1 decision is passed.

In the calorimeters, the L1 trigger decision is based on towers with a reduced granularity of 0.1×0.1 in $\Delta\eta \times \Delta\phi$. Independent systems operate in parallel to look for electron, photon, τ, and jet candidates. The L1 trigger decision for electrons, photons, and τ leptons can include isolation requirements. Electron candidates are selected based on 0.2×0.2 clusters in $\eta \times \phi$. Electron isolation at L1 is based on the 12 cells surrounding the cluster. A schematic of the calorimeter cells used in the electron trigger decision is shown in Figure 3.13. The search for jet candidates also produces scalar sums of transverse energy and a measurement of missing transverse energy that can fire a L1 trigger. The multiplicity of trigger objects is also taken into account for trigger decisions.

In the muon system, the L1 trigger uses the TGC and RPC detectors, described above. In both the barrel and endcaps, the trigger uses three trigger stations. The trigger algorithm defines a road that tracks the muon path and requires a coincidence of hits in different stations along that road. The road width is based on the trigger p_T threshold, ranging from 6 to 35 GeV.

The L2 trigger is based on Regions of Interest (RoI) that are defined in the L1 trigger and saved in the detectors as they wait for the L1 trigger decision. Only the data in these RoIs, representing 1-2% of the full data in the event, are used in the L2 trigger decision. While the L1 trigger decision must be made in 2.5 μs, the L2 trigger decision must be made in 40 ms. The objects in the L2 trigger decision are identical to the objects used in the Event Filter. Because the objects are the same, the L2 trigger analysis is used by the EF as part of its decision.

The Event Filter runs full event reconstruction, using the same algorithms as offline reconstruction. Entire events are built and analyzed for the EF trigger decision. This reconstruction is performed at a processing farm with a number of configurable, independent nodes. Events that pass the EF are sent to various streams based on the trigger chains that

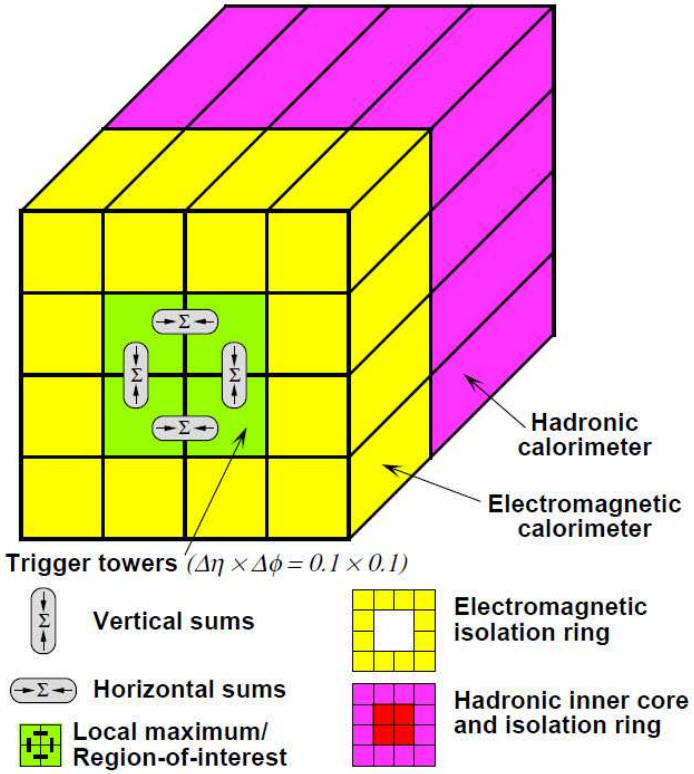

Figure 3.13: A schematic for the electron/photon/τ trigger including isolation [8]

seeded them: electrons, muons, jets, photons, E_T^{miss}, etc. Each event is recorded in one or more streams. The EF requires roughly 4 seconds per event.

3.3 Luminosity Measurements

An accurate determination of the delivered luminosity is a vital part of many ATLAS analyses; for a given process, the expected number of events will be proportional to the measured luminosity. Any uncertainty in the luminosity will directly affect the uncertainty of a measured cross section or limit. ATLAS measures luminosity using several different algorithms. The luminosity scale for these algorithms is calibrated using periodic beam separation scans. A full description of the luminosity determination as performed during the 2011 run is described in [9]. The luminosity determination for the 2012 run was done in a similar manner. The consistency of different luminosity measurements with each other ensures a good understanding of systematic uncertainties associated with the luminosity determination. Beam separation scans are performed infrequently, so it is important to understand the stability of these measurements at different times and with different detector conditions. Documen-

tation of the first beam separation scan in the LHC, measured using the ATLAS detector, can be found in [61].

The luminosity at a p-p collider can be written as

$$L = \frac{R_{\text{inel}}}{\sigma_{\text{inel}}}, \tag{3.7}$$

where R_{inel} is the rate of inelastic collisions and σ_{inel} is the cross section for inelastic collisions. As any physical detector has some finite acceptance, R_{inel} is an inaccessible quantity. Instead, some visible process must be measured with a finite efficiency: $\sigma_{\text{vis}} = \epsilon\sigma_{\text{inel}}$. If f_{rev} is the revolution frequency and n_{b} is the number of bunches, the luminosity can be rewritten as

$$L = \frac{n_{\text{b}} f_{\text{rev}} \mu_{\text{vis}}}{\sigma_{\text{vis}}}, \tag{3.8}$$

where μ_{vis} is the number of times the process in question is observed in a given bunch crossing. This measurement of luminosity can be compared to the luminosity defined by beam parameters for head on collisions and Gaussian beams:

$$L = \frac{N_{\text{b}}^2 n_{\text{b}} f_{\text{rev}}}{4\pi\sigma_{\text{x}}\sigma_{\text{y}}}. \tag{3.9}$$

The beams might not collide head on. To handle such a situation, the luminosity can be written in terms of beam overlap rather than beam size:

$$L = \frac{N_{\text{b},1} N_{\text{b},2} n_{\text{b}} f_{\text{rev}}}{2\pi\Sigma_{\text{x}}\Sigma_{\text{y}}}, \tag{3.10}$$

where Σ_{x} and Σ_{y} are the convolution of the beam widths in each direction. Σ_{x} and Σ_{y} can be measured directly using beam separation scans. If an external measurement of the number of protons in each bunch, $N_{\text{b},1}$ and $N_{\text{b},2}$ is made, the luminosity can be computed from this equation.

3.3.1 Luminosity Detectors and Algorithms

ATLAS has a number of detectors specifically designed to measure luminosity and a variety of algorithms that can be used to specify a σ_{vis}. These algorithms are broadly separated into *event counting* algorithms, which mark bunch crossings where a certain event criteria is satisfied, and *hit counting* algorithms, which count the number of hits in a given detector for each bunch crossing.

The ID, described in Section 3.2.2, can be used as a luminosity detector. Given the excellent reconstruction capabilities of the various subdetectors, a number of event and hit counting algorithms could be defined using the ID. In practice, the reconstruction of primary vertices is commonly used for luminosity determination. It was possible to use the observation of a primary vertex as an event counting technique in very early running. After this initial period, the significant number of interactions per bunch crossing, shown

in Figure 3.14, makes primary vertex counting a hit counting technique. Primary vertex counting is complicated by the possibility that some vertices will mask others. Hit counting techniques can be performed with the various ATLAS calorimeters as well.

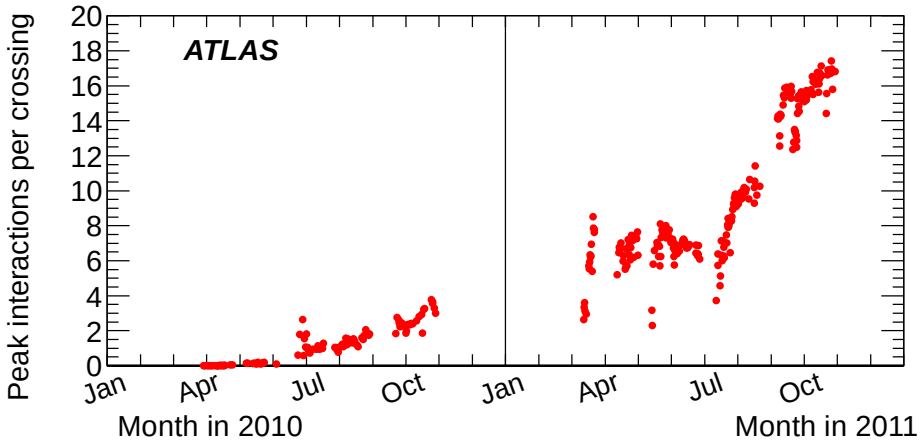

Figure 3.14: Average number of inelastic p-p interactions per bunch crossing at the start of each fill in 2010 and 2011 [9]

The Beam Condition Monitor (BCM) consists of four small diamond sensors arranged around the beam pipe at $z = \pm 184$ cm, corresponding to $|\eta| = 4.2$. The nominal purpose of the BCM is to provide a beam abort signal in situations where an badly controlled beam risks damaging the ID. Because the BCM provides hit information with a small acceptance, it can be used in an event counting algorithm for luminosity determination. The BCM is separated into vertical (BCMV) and horizontal (BCMH) sensors, based on their position relative to the beam pipe.

LUCID is a Cherenkov detector consisting of 16 aluminum tubes filled with C_4F_{10} at $z = \pm 17$ m, corresponding to $5.6 < |\eta| < 6.0$. Charged particles traversing the detector leave Cherenkov photons, which reflect from the tube walls and are measured by photomultiplier tubes. The LUCID detector is programmable, registering a hit if the PMTs produce a signal above some pre-set threshold. The relatively high rates in LUCID after 2010 force the detector to operate in a hit-counting mode for the 30 detector channels. The use of LUCID in hit-counting mode is complicated by the need to handle correlation between different channels.

3.3.2 Beam Separation Scans

To calibrate each algorithm, σ_{vis} for that detector and algorithm, and must be calculated. As discussed above, this can be done in a beam separation scan. Using the two definitions of luminosity above, σ_{vis} is solved for explicitly:

$$\sigma_{\mathrm{vis}} = \mu_{\mathrm{vis}} \frac{2\pi \Sigma_{\mathrm{x}} \Sigma_{\mathrm{y}}}{N_{\mathrm{b},1} N_{\mathrm{b},2}}. \tag{3.11}$$

Here, μ_{vis} is defined and measured for a particular algorithm. $N_{\mathrm{b},1}$ and $N_{\mathrm{b},2}$ are measured from beam-current transformers. In a beam separation scan the beams are displaced from each other by up to $\pm 6\sigma_{\mathrm{b}}$ in the x coordinate while centered in the y coordinate, where σ_{b} is the transverse beam size. The beam displacement is varied in a certain number of scan steps with the interaction rate recorded at each step. The width of the interaction rate as a function of beam displacement, shown in Figure 3.15, is a measurement of Σ_{x}. This process is repeated in the y coordinate with the beams centered in x. The analogous scan in the y direction is used to calculate Σ_{y}.

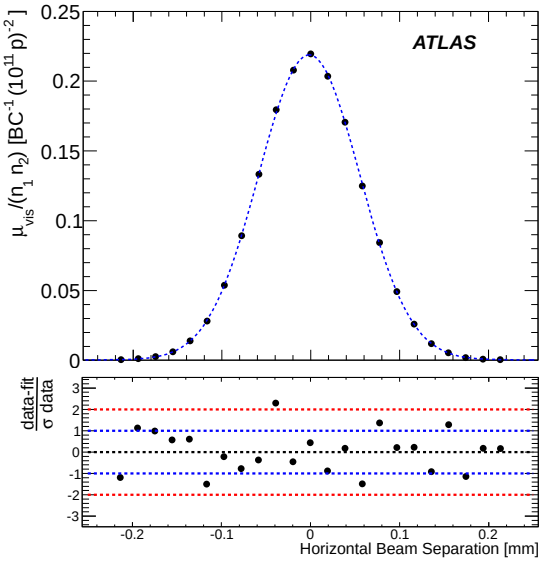

Figure 3.15: σ_{vis} as measured by the BCMH algorithm during a beam separation scan in 2011 [9]

The consistency of σ_{vis} is checked in a number of ways. The measurement of σ_{vis} can be performed independently for each of colliding bunch. The consistency of these independent measurements establishes the reproducibility of σ_{vis}. The consistency of σ_{vis} is also checked across many different algorithms, over a significant duration, and in a variety of detector conditions.

For the data considered in this dissertation, the BCMV_EventOR algorithm, which requires a hit in the BCMV detectors on either side of ATLAS, is used to determine the experiment luminosity. The uncertainty in the luminosity determination for this period in 2012 is 3.6%.

Chapter 4

Analysis Strategy

This chapter gives a brief overview of the remainder of the dissertation and provides context for each of the chapters. The search for a WZ resonance proceeds through four channels based on the types of leptons found in an event: $e\nu ee$, $\mu\nu ee$, $e\nu\mu\mu$, and $\mu\nu\mu\mu$. A simultaneous fit to all four channels is used for the final analysis. Given that there is no expectation that any process will favor a particular lepton flavor, the "inclusive" channel, which is the sum of the four individual channels, is often presented.

Electrons are selected based on tracking information from the Inner Detector combined with information about energy deposition and shower shape inside the calorimeters. This information is used to discriminate between electrons and photons, and electrons and pions. Muons are selected based on a combination of Inner Detector tracking and muon system tracking measurements.

Neutrinos produced inside the ATLAS detector will pass through it without interacting. The escaping neutrino will still carry momentum, and so its presence can be inferred from for a global momentum imbalance in the event. This imbalance is measured mostly in the calorimeters, and so is given the name "missing transverse energy." The precise calculation of missing transverse energy, however, uses all of the physics objects in the event: electrons, muons, tau leptons, photons, etc, each with its own energy or momentum calibration.

Events that contain three well reconstructed leptons and significant missing transverse energy are used for the analysis. The narrow resonance of the Z boson allows a clean tagging of events with a Z by reconstructing two leptons with the same flavor and opposite charge, and requiring that the invariant mass of the two-lepton system be near the Z boson pole mass. Because only transverse information is available for the neutrino associated with the W boson decay, an invariant mass cannot be formed directly. The transverse mass, i.e., the mass using only the information in the x and y coordinates is reconstructed instead. This transverse mass is not allowed to be much larger than the W pole mass, as this would indicate an event that does not have a physical W boson. Once a good W candidate is found, the assumption that it is, in fact, on-shell adds an additional constraint that can be used to recover the missing component of the neutrino momentum.

Resonant production of WZ events will tend to produce events that are more back-to-

back than the WZ production in the Standard Model. This difference is used to place cuts on angular separation of the W and Z bosons. These cuts also allow a clean definition of control regions where the contribution from a potential new physics signal would be small.

The number and distribution of events passing this selection and originating from Standard Model processes can be estimated from simulated events. "Monte Carlo" samples of Standard Model WZ production, along with a range of other background and signal processes that can pass this selection are generated and passed through a simulation of the ATLAS detector. These samples provide a good description of some processes, such as the prompt production of muons, but a less reliable description of other processes, such as the rate at which jets land in a strange kinematic corner and are reconstructed as electrons.

These "fake" leptons are known to be poorly modeled by simulation. The contribution of events with fake leptons to the signal selection is measured using a "fake factor." The fake factor is the ratio of leptons from fake sources that are reconstructed as real leptons, to leptons from fake sources that are reconstructed with a looser selection. Once measured, this fake factor can be used to estimate the number of events that have reconstructed leptons coming from fake sources by looking at the number of events that have this looser kind of object.

A significant number of individual cuts and tunings go into performing this analysis. In order to ensure that these cuts and tunings are not unintentionally biased towards a specific end result, this analysis is performed in a blind fashion. The boson angular cuts, described above, are inverted to define a Standard Model WZ control region that is unlikely to have any contribution from new physics. The work of optimizing cuts and understanding background distributions is performed only looking at data in this and other control regions. Tuning for good sensitivity is done looking at simulated events in the signal region, but never at data in the signal region. Once a good understanding of the analysis is obtained from these control regions, the tuning of the analysis is frozen and the signal region is unblinded.

Two specific control regions are of significant importance. The first is, as mentioned above, the Standard Model WZ control region. An event in the Standard Model WZ control region must fail the angular separation cuts that are required in the signal region, but pass all other analysis cuts. This region, as suggested by the name, is dominated by the contribution of Standard Model WZ events. A second control region, based on events with low missing transverse energy and low W transverse mass, is used to select a region dominated by fake leptons where the fake factor can be measured.

The calculations performed in this analysis rest on a large number of inputs that are not perfectly understood: The response of the calorimeter to an electron of a particular energy is understood and tuned, but that tuning is only known to within a few percent. The same is true for all of the detector inputs, for the expected cross section for background processes, and for the measurement of the fake factor. The effect of these systematic uncertainties is propagated through the analysis and quantified as a fractional deviation per bin in the invariant mass of the WZ system. The largest systematic uncertainty in the total event counts comes from uncertainty in the Standard Model WZ cross section. The largest systematic uncertainty for high mass events comes from an uncertainty in extrapolating the background

distributions to those regions.

With the simulated signals, estimated backgrounds, and systematic uncertainties in place, limits are set on the cross section for a number of different resonant masses. The full shape of the WZ invariant mass is used by performing a negative log likelihood fit to the background only and to the signal plus background hypothesis. The CL_{s} method is used to derive limits on the size of a potential new physics signal.

Chapter 5

Object Selection

5.1 Tracking

A key step in building physics objects from detector outputs is to reconstruct tracks. The full track reconstruction procedure is described in [62] and [56]. The primary method for track reconstruction starts from the innermost tracking detector layers, building space points into track seeds and track seeds into roads that are then fit to a particle track and extended into the TRT. This inside-out method is supplemented by an outside-in tracking algorithm to help recover non-prompt tracks or tracks with badly resolved innermost hits.

Space points are constructed by mapping the two-dimensional hit information for a particular detector to a three-dimensional point. In the pixel detector, this requires only an accurate description of the detector geometry. In the SCT, both hits in a double layer are used with detector geometry and beam spot information to produce a single space point. Space points in the pixel detector and the innermost SCT layer are then formed into track seeds.

For each seed, a track is built by adding hits from sequential layers. At each step, a Kalman filter [63] is used to refit the result. A material model of the detector here allows handling multiple scattering of tracks.

Because the resulting collection of tracks may contain hits shared between several tracks and fake tracks, which do not come from a single particle, an ambiguity-resolving step is run that scores tracks based on precision hits and penalizes them for holes. Ambiguous hits are then assigned to high scoring tracks, and the tracks refit accordingly. Once track finding has finished in the silicon detectors, the tracks are extended into the TRT, and one final refit is done.

5.2 Vertex Reconstruction

The accurate reconstruction of the primary vertex [64] in an event is important for disentangling the objects from a single interesting interaction from the average of 20 pile-up

interactions that can occur in a single event. Vertex reconstruction starts from the identification of tracks passing the quality requirements described in [64] and coming from the interaction region. Given these tracks, vertex seeds are chosen based on clustering of tracks along the z coordinate. Given these seeds, a deterministic annealing [65] procedure is used to fit the vertex parameters. Tracks that are incompatible with this vertex are then used to seed a new vertices. This process is iterated on until no new vertices can be formed. The vertex with the highest sum p_T^2 of associated tracks is defined to be the primary vertex.

The vertex fitting procedure minimizes an iteratively re-weighted sum of square deviations of the vertex position with respect to each track. The weights are determined both by the track parameters and a temperature, which softens the contribution of tracks poorly matched to the vertex. The fit is then iterated with progressively lower temperatures, allowing the fit to converge on the proper vertex and reducing the chance of ending in a local minimum.

To minimize the contamination of cosmic rays passing though the detector, a primary vertex is required to have at least three tracks with $p_T > 400$ GeV.

5.3 Beam Spot Reconstruction

The parameters of the beam spot are determined by an unbinned maximum likelihood fit to the reconstructed vertices in an event [61]. The beam spot fit is run once for each period of roughly 10 minutes of data. The fit reconstructs the beam spot position, width, and tilt in the x-z and y-z planes. To disentangle the spread in vertices arising from the size of the beam spot and the spread in vertices arising from the uncertainty in their position, a vertex error scale factor is also included in this fit. This scale factor is expected to be close to 1, and its behavior is cross checked using a data-driven method.

To verify the accurate performance of the beam spot fit to the vertex error scale factor, a vertex splitting method is used to measure the intrinsic vertex resolution. In the vertex splitting method, the tracks associated with a vertex are split evenly into two sets. Each set of tracks is then rebuilt into a "half" vertex. Using simulated data, it is verified that the distance between half vertices is well described by the uncertainty in the position of similar full vertices, as seen in Figure 5.1. When this split vertex method is compared to the vertex error scale factor from the beam spot fit, the results are found to show a tension on the order of 5%, as seen in Figure 5.2. This tension is assessed as a systematic uncertainty in the beam spot parameters.

5.4 Electrons

Electron reconstruction in ATLAS combines calorimeter information with tracks in the Inner Detector to build electron candidates of varying quality. A full description of electron reconstruction can be found in [66]. Electron reconstruction starts with the formation of 3×5 (in $\eta \times \phi$ space) cell clusters in the middle sampling of the electromagnetic calorimeter. A cell

has dimensions 0.025×0.025. A sliding window algorithm is used to cover the full acceptance of the EM calorimeter. Clusters with $E_T > 2.5$ GeV are used to seed the reconstruction algorithm.

Given these seeds, an electron candidate is formed if a cluster is matched to a track in the ID with $p_T > 0.5$ GeV; the track that extrapolates closest to the cluster barycenter is considered the best match. These electron candidates are then classified into object quality categories, *loose*, *medium*, and *tight*, intended to provide good acceptance for true electrons and a strong rejection of photon conversions and QCD jets [10]. The cuts defining these categories vary over η and ϕ to ensure that the electron performance is consistent throughout the detector.

Loose electrons are selected based on hadronic leakage, the amount of energy that is deposited beyond the EM calorimeter in the hadronic calorimeter, and the shower shape variables in the EM calorimeter. *Medium* electrons are selected based on the *loose* criteria plus requirements on the size and shape of the cluster in the strip layer of the EM calorimeter, requirements on the number of hits, and impact parameter for the track associated with the

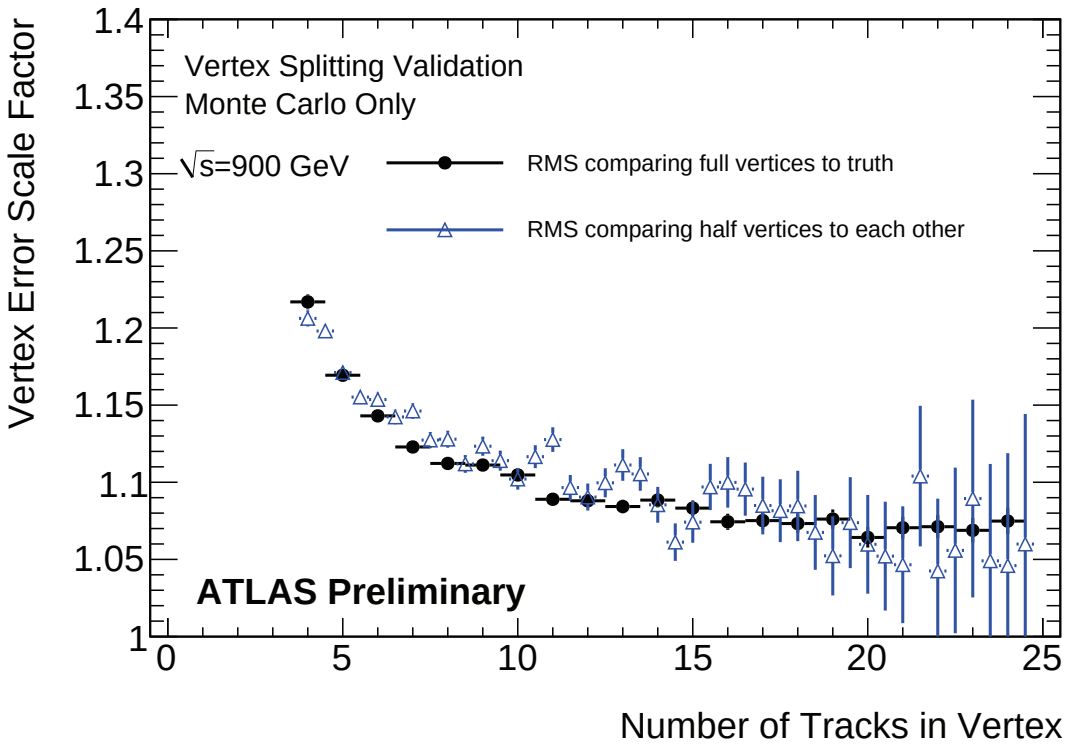

Figure 5.1: Scale factor between the actual and estimated offline vertex resolutions in minimum bias Monte Carlo as a function of the number of tracks. The scale factor from full vertices is binned by the number of tracks in that vertex. The scale factor from vertex splitting is binned by the average number of tracks in the two half vertices.

electron, and matching between the track and calorimeter η. *Tight* electrons are selected based on the *medium* electron criteria plus requirements on a hit in the innermost layer of the pixel detector, matching between the cluster and track ϕ, matching between the cluster energy and track momentum, and requirements for a number of hits and high threshold hits in the TRT.

Electron cluster energy is computed by summing four contributions: energy deposited in the material in front of the EM calorimeter, energy deposited inside the cluster itself, energy deposited inside the calorimeter but outside the cluster, and energy deposited behind the EM calorimeter. These contributions are parametrized as a function of the presampler and three accordion layer energies, and these parameters are a function of the cell pseudorapidity.

5.5 Muons

Muon reconstruction in the ATLAS detector defines several categories of muons, based on the use of the dedicated muon system, Inner Detector, and calorimeters, described in full in

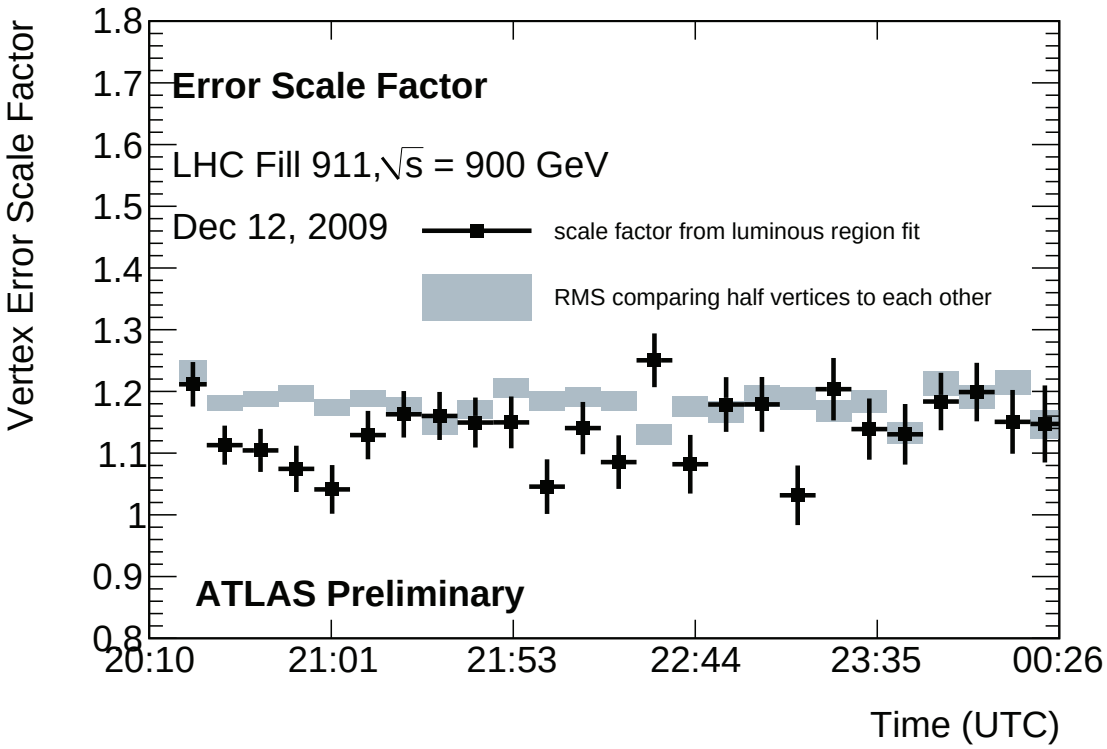

Figure 5.2: Scale factor time line. Scale factor between the actual and estimated offline vertex resolutions taken as the k parameter from the fit to the luminous region, compared to the RMS from the vertex splitting method.

[56]. *Stand-alone muons* use only the muon system, extrapolating the resulting track back to the beam line. *Combined muons* match tracks in the muon system with tracks in the ID. *Tagged muons* extrapolate ID tracks out to track segments in the muon system.

Stand-alone muons are built from track segments at each of the three muon system stations and extrapolated back to the interaction point. Stand-alone muons must correct for multiple scattering and energy loss in the detector material traversed before reaching the muon system. Because only muon system information is used, stand-alone muons are more likely to contain contamination from muons produced by π and K decays in the calorimeter.

Combined muons pair ID tracks with muon system tracks, keeping well matched pairs. The STACO algorithm used in this analysis does a statistical combination of the resulting muon tracks based on parameters at the interaction point to obtain a combined track. Because of the requirements of both a muon system and ID track, combined muons are limited to $|\eta| < 2.5$. The combined muon requirements give them the best discrimination against non-prompt or fake muons.

Tagged muons start with an ID track and extrapolate it to the first muon station. If a sufficiently good match is found, the ID track is used to describe the muon kinematics. Tagged muons are useful for understanding low p_T muons, which do not reach the outer muon stations.

The muon reconstruction process [67] starts from the selection of a 0.4×0.4 in $\eta \times \phi$ space region of activity (ROA) centered around an RPG/TGC hit in both coordinates. All chambers that intersect this ROA then take part in the muon reconstruction.

Next, straight track segments are formed by looking for pairs of hits in an MDT station, requiring further that these track segments point roughly back to the interaction point. A straight track segment is used because the distance between points is small.

These track segments are extrapolated to each other and fitted to a muon system track. This extrapolation uses tracking in the muon system magnetic field and gives an estimate of the track momentum. Further, this extrapolation selects a single segment per station to be used in the final fit.

Finally, if at least two track segments are associated with a potential muon, the hits associated with these track segments are refit to a single track using information that includes a description of the muon magnetic field and the matter traversed by the particle.

5.6 Jets

Although jets are not used directly in this analysis, they contribute significantly to the reconstruction of missing transverse energy. Jets also help to probe fake lepton backgrounds, which often contain a jet that is mis-reconstructed as a real, prompt lepton.

Jets in the ATLAS detector are formed from energy in the calorimeters, clustered into toplogical objects [68], and built into jets using the using the anti-k_T algorithm [69]. Topological clusters are used to select calorimeter energy deposits that are unlikely to have resulted from noise. The anti-k_T algorithm sequentially combines topological clusters using a metric

that favors high energy and spatially close clusters. This sequential combination out to a certain radius parameter satisfies a number of theoretical concerns, including infrared safety and experimental concerns, including having a well defined jet shape and clear separation between overlapping jets.

Topological clusters are formed, first by finding seed calorimeter cells that have a signal to noise ratio $t_{\text{seed}} > 4$. These calorimeter cells define the beginnings of a cluster. From this list of clusters, all neighboring cells with a signal to noise ratio $t_{\text{cell}} > 2$ are added to the corresponding cluster. This process of adding neighboring cells is iterated until no further cells satisfy $t_{\text{cell}} > 2$. Afterward, one more iteration of neighboring cells with $t_{\text{cell}} > 0$ is added to each cluster. The resulting cluster has energy equal to the sum of the constituent cells at a position determined by the energy-weighted barycenter of those cells.

The anti-k_T algorithm sequentially combines calorimeter clusters into jets based on the metric:

$$d(i,j) = min(k_{T,i}^{-2}, k_{T,j}^{-2}\frac{\Delta(i,j)^2}{R^2}) \tag{5.1}$$

$$d(i,B) = k_{T,i}^{-2}, \tag{5.2}$$

where $\Delta(i,j) = \sqrt{(\eta_i - \eta_j)^2 + (\phi_i - \phi_j)^2}$. In each iteration, the smallest distance between objects is calculated. If that distance is $d(i,B)$, object i is declared a jet and removed from the list of objects. If that distances is $d(i,j)$, objects i and j are combined.

In an environment with hard clusters (formed predominantly from real particles) and soft clusters (from both real particles and calorimeter noise), such an algorithm will add clusters to a growing, hard object until $\Delta(i,j) > R^2$ for all of the remaining noise outside the cluster. This is useful behavior compared to the k_T algorithm, which uses $k_{T,i}^2$ rather than $k_{T,i}^{-2}$ and thus clusters soft energy deposits first, making jet shape sensitive to calorimeter noise. The seedless behavior of the anti-k_T algorithm also provides infrared safety, ensuring that a large energy deposit split between two clusters is quickly recombined into a single object.

5.7 Missing Transverse Energy

Although neutrinos will escape the detector without interacting, it is important, especially when studying electroweak processes, to attempt to measure those escaping particles' properties. This can be accomplished by considering the transverse momentum imbalance in an event, E_T^{miss}. Because momentum conservation is expected in the transverse plane, a significant imbalance likely corresponds to a particle escaping the detector. The missing transverse energy of an event is the opposite of the sum of the transverse momentum of the measured objects in that event:

$$E_{x(y)}^{miss} = -(E_{x(y)}^{\mu} + E_{x(y)}^{e} + E_{x(y)}^{\gamma} + E_{x(y)}^{\tau} + E_{x(y)}^{jet} + E_{x(y)}^{calo}). \tag{5.3}$$

Such an argument cannot be made in the longitudinal direction however, where an unmeasured amount of energy continues down the beam line.

The missing transverse energy is built from reconstructed physics objects and unassociated energy in the calorimeter, as described in [70]. In order, energy is associated with muons, electrons, photons, hadronically decaying taus, jets, and unclustered calorimeter energy. Although the energy of all of these objects, save muons, is measured in the calorimeter, the particular calibration for each physics object is used to better resolve that object's energy and to consistently use each physics object in an event.

Chapter 6

Monte Carlo Samples

A number of different physics processes are expected to contribute to the final set of selected events. Modeling of these processes is important to understand the Standard Model expectation and potential contributions from new physics signals. A large fraction of the event modeling is done via Monte Carlo simulation of events, starting from a variety of event generators, which simulate both the hard scatter and subsequent hadronization of p-p collisions, through detector simulation using GEANT4 [71], and event reconstruction using the ATLAS reconstruction software. Each sample is normalized to the integrated luminosity used in this analysis.

6.1 Signal

Signal samples containing a resonant decay to WZ are generated for two models: An extended gauge model (EGM) W' boson [37] and a low scale Technicolor ρ_T [72] [73]. W' events are produced for masses between 200 GeV and 2 TeV with 200 GeV spacings using the PYTHIA8 event generator [74] with the modified leading order (LO*) MSTW2008LO [75] [2] parton distribution function (PDF). The LSTC process is not available in PYTHIA8, and so PYTHIA6 [25] is used for the matrix element calculation. The resulting Les Houches Accords file [76] is passed to PYTHIA8 for hadronization. LSTC events are generated between 250 GeV and 1000 GeV in steps of 50 GeV. The specific parameters used are: N_{TC}, the number of technicolors in the model, is 4. Q_U, the charge of up-type technifermions is 1. Q_D, the charge of down-type technifermions is 0. $sin\chi$, the mixing angle between technipions and electroweak gauge bosons is 1/3. Two scenarios are used for the mass of the a_T particle, $m_{aT} = 1.1m_{\rho T}$ and $m_{aT} = 5$ TeV. The latter represents a scale where the a_T is not accessible to this sample of events. The π_T mass is varied when considering limits, although only a single sample with $m_{\rho T} = m_{\pi T} + m_W$ is passed through full reconstruction. Because the shape of the WZ mass peak is strongly dominated by detector resolution, the samples with different $m_{\pi T}$ only have a different branching ratio to WZ. Similarly, only the $m_{aT} = 1.1m_{\rho T}$ signals are passed through reconstruction, with the $m_{aT} = 5$ TeV a_T mass

affecting only the signal cross section times branching fraction of the technicolor signal, but not the shape of $m(WZ)$. A table of the generated events is in Table 6.1. For both W' and ρ_T samples, the Z boson is required to decay to either electrons or muons, and the W boson is required to decay to electrons, muons, or taus. The inefficiency to reconstruct two tau leptons as electrons or muons. and for the result to fall within the selected Z mass window makes effect of neglecting events with $Z \to \tau\tau$ small.

Table 6.1: EGM W' and LSTC ρ_T MC samples with the generator used, the number of simulated events, k-factor, and the corresponding cross-sections times branching ratios. No generator level filter was used for these samples.

MCID	Process	Generator	Events	$\sigma\times$ B [pb]	k-factor	ϵ_{filter}
159227	$W' \to WZ \to \ell\nu\ell\ell$ ($M_{W'} = 200$ GeV)	PYTHIA	30000	1.01	1.0	1.0
159228	$W' \to WZ \to \ell\nu\ell\ell$ ($M_{W'} = 400$ GeV)	PYTHIA	30000	0.174	1.0	1.0
159229	$W' \to WZ \to \ell\nu\ell\ell$ ($M_{W'} = 600$ GeV)	PYTHIA	30000	0.0323	1.0	1.0
159230	$W' \to WZ \to \ell\nu\ell\ell$ ($M_{W'} = 800$ GeV)	PYTHIA	30000	0.00913	1.0	1.0
159231	$W' \to WZ \to \ell\nu\ell\ell$ ($M_{W'} = 1000$ GeV)	PYTHIA	30000	0.00329	1.0	1.0
159232	$W' \to WZ \to \ell\nu\ell\ell$ ($M_{W'} = 1200$ GeV)	PYTHIA	30000	0.00135	1.0	1.0
159233	$W' \to WZ \to \ell\nu\ell\ell$ ($M_{W'} = 1400$ GeV)	PYTHIA	30000	0.000595	1.0	1.0
159234	$W' \to WZ \to \ell\nu\ell\ell$ ($M_{W'} = 1600$ GeV)	PYTHIA	30000	0.000278	1.0	1.0
159235	$W' \to WZ \to \ell\nu\ell\ell$ ($M_{W'} = 1800$ GeV)	PYTHIA	30000	0.000135	1.0	1.0
159236	$W' \to WZ \to \ell\nu\ell\ell$ ($M_{W'} = 2000$ GeV)	PYTHIA	30000	0.0000685	1.0	1.0
158129	($M_{\rho_T} = 250$ GeV)	PYTHIA	20000	0.133	1.0	1.0
158130	($M_{\rho_T} = 300$ GeV)	PYTHIA	20000	0.0767	1.0	1.0
158131	($M_{\rho_T} = 350$ GeV)	PYTHIA	20000	0.0460	1.0	1.0
158132	($M_{\rho_T} = 400$ GeV)	PYTHIA	20000	0.0288	1.0	1.0
158133	($M_{\rho_T} = 450$ GeV)	PYTHIA	20000	0.0191	1.0	1.0
158134	($M_{\rho_T} = 500$ GeV)	PYTHIA	20000	0.0130	1.0	1.0
158135	($M_{\rho_T} = 550$ GeV)	PYTHIA	20000	0.00910	1.0	1.0
158136	($M_{\rho_T} = 600$ GeV)	PYTHIA	20000	0.00654	1.0	1.0
158137	($M_{\rho_T} = 650$ GeV)	PYTHIA	20000	0.00479	1.0	1.0
158138	($M_{\rho_T} = 700$ GeV)	PYTHIA	20000	0.00356	1.0	1.0
158139	($M_{\rho_T} = 750$ GeV)	PYTHIA	20000	0.00270	1.0	1.0
158140	($M_{\rho_T} = 800$ GeV)	PYTHIA	20000	0.00206	1.0	1.0
158141	($M_{\rho_T} = 850$ GeV)	PYTHIA	20000	0.00159	1.0	1.0
158142	($M_{\rho_T} = 900$ GeV)	PYTHIA	20000	0.00125	1.0	1.0
158143	($M_{\rho_T} = 950$ GeV)	PYTHIA	20000	0.000978	1.0	1.0
158144	($M_{\rho_T} = 1000$ GeV)	PYTHIA	20000	0.000777	1.0	1.0

6.2 Background from MC

The dominant irreducible background, coming from Standard Model WZ production is calculated at next-to-leading order (NLO) by the POWHEG [77] [78] generator using the CTEQ10 parton distribution function [79] interfaced to the PYTHIA8 generator [74] for hadronization. The QED initial and final state radiation in these events is handled separately by PHOTOS [80]. Tau decays are handled separately by TAUOLA [81].

ZZ events can fall into the event selection if one lepton falls outside the detector acceptance, or fails the reconstruction requirements. $ZZ \to \ell\ell\ell\ell$ events are also simulated with POWHEG. $Z + \gamma$ events can pass the event selection if the photon is mis-reconstructed as an electron. This process is simulated with SHERPA 1.4.0 [26] and its cross section corrected to NLO using results obtained from the MCFM generator [82]. $W + \gamma$ events are generated using the ALPGEN 2.1.4 generator [27] with cross sections corrected using MCFM, though none of the simulated events passes the final event selection. WW events can pass the event selection when a jet in the event is mis-reconstructed as a prompt lepton. WW events are produced using MC@NLO 4.0.6 [83] Simulated events from $W + jet$ and $Z + jet$ processes are generated using POWHEG and can pass into the event selection in the presence of fake leptons, as can $t\bar{t}$, single top, and Wt processes, which are simulated at NLO using MC@NLO 4.0.6. While samples that enter the selection through jets faking leptons are generated to study kinematic distributions, because this process is difficult to describe using Monte Carlo this analysis uses a data-driven method, described in Section 8.1, to measure the contribution of lepton fakes from jets. Background samples that are used in the analysis are listed in Table 6.2. Reducible background samples that are used only as cross checks to the data-driven estimates backgrounds are listed in Tables 6.3, 6.4, and 6.5.

Table 6.2: MC samples for backgrounds that do not require fake leptons from jets to pass selection. The generator used, the number of simulated events, k-factor, and the corresponding cross-sections times branching ratios and generator filter efficiency are shown.

MCID	Process	Generator	Events	$\sigma\times$ B [pb]	k-factor	ϵ_{filter}
129477	$W^+Z \to eee$	POWHEG + PYTHIA	190000	0.29456	1.0	1.407
129478	$W^+Z \to \mu\mu e$	POWHEG + PYTHIA	190000	0.35211	1.0	0.9382
129479	$W^+Z \to \tau\tau e$	POWHEG + PYTHIA	76000	0.16682	1.0	0.1746
129480	$W^+Z \to ee\mu$	POWHEG + PYTHIA	189999	0.29351	1.0	1.399
129481	$W^+Z \to \mu\mu\mu$	POWHEG + PYTHIA	190000	0.35132	1.0	0.9537
129482	$W^+Z \to \tau\tau\mu$	POWHEG + PYTHIA	76000	0.16863	1.0	0.1746
129483	$W^+Z \to ee\tau$	POWHEG + PYTHIA	75400	0.14289	1.0	1.399
129484	$W^+Z \to \mu\mu\tau$	POWHEG + PYTHIA	76000	0.18256	1.0	0.9382
129485	$W^+Z \to \tau\tau\tau$	POWHEG + PYTHIA	19000	0.058517	1.0	0.1719
129486	$W^-Z \to eee$	POWHEG + PYTHIA	189899	0.29694	1.0	0.9795
129487	$W^-Z \to \mu\mu e$	POWHEG + PYTHIA	190000	0.35302	1.0	0.639
129488	$W^-Z \to \tau\tau e$	POWHEG + PYTHIA	76000	0.15969	1.0	0.1125
129489	$W^-Z \to ee\mu$	POWHEG + PYTHIA	190000	0.29766	1.0	0.9359
129490	$W^-Z \to \mu\mu\mu$	POWHEG + PYTHIA	76000	0.35414	1.0	0.6488
129491	$W^-Z \to \tau\tau\mu$	POWHEG + PYTHIA	76000	0.16023	1.0	0.1125
129492	$W^-Z \to ee\tau$	POWHEG + PYTHIA	76000	0.14803	1.0	0.9359
129493	$W^-Z \to \mu\mu\tau$	POWHEG + PYTHIA	76000	0.18657	1.0	0.639
129494	$W^-Z \to \tau\tau\tau$	POWHEG + PYTHIA	19000	0.056651	1.0	0.1107
126937	$ZZ \to eeee$	POWHEG + PYTHIA	599998	0.07686	1.0	0.90739
126938	$ZZ \to ee\mu\mu$	POWHEG + PYTHIA	599799	0.1755	1.0	0.82829
126939	$ZZ \to ee\tau\tau$	POWHEG + PYTHIA	599899	0.1754	1.0	0.58235
126940	$ZZ \to \mu\mu\mu\mu$	POWHEG + PYTHIA	600000	0.07687	1.0	0.91187
126941	$ZZ \to \mu\mu\tau\tau$	POWHEG + PYTHIA	600000	0.1754	1.0	0.58726
126942	$ZZ \to \tau\tau\tau\tau$	POWHEG + PYTHIA	300000	0.07685	1.0	0.10604
126949	$ZZ \to ee\nu\nu$	POWHEG + PYTHIA	299400	0.05431	1.0	1.0
126950	$ZZ \to \mu\mu\nu\nu$	POWHEG + PYTHIA	300000	0.05431	1.0	1.0
126951	$ZZ \to \tau\tau\nu\nu$	POWHEG + PYTHIA	299999	0.05431	1.0	1.0
145161	$Z\gamma \to ee\gamma$	SHERPA	1199795	32.26	1.0	1.0
145162	$Z\gamma \to \mu\mu\gamma$	SHERPA	1199596	32.317	1.0	1.0

Table 6.3: MC samples for backgrounds that require fake leptons from jets to pass selection. The generator used, the number of simulated events, k-factor, and the corresponding cross-sections times branching ratios and generator filter efficiency are shown. These samples are used only as a cross check to the data-driven background estimation.

MCID	Process	Generator	Events	$\sigma\times$ B [pb]	k-factor	ϵ_{filter}
147806	$Z \to ee$	POWHEG + PYTHIA	9994580	1109.9	1.0	1.0
147807	$Z \to \mu\mu$	POWHEG + PYTHIA	9978282	1109.8	1.0	1.0
147808	$Z \to \tau\tau$	POWHEG + PYTHIA	4999692	1109.9	1.0	1.0
126928	$W^+W^- \to e^+e^-$	POWHEG + PYTHIA	299700	0.59774	1.0676	1.0
126929	$W^+W^- \to \mu^+e^-$	POWHEG + PYTHIA	299700	0.59745	1.0681	1.0
126930	$W^+W^- \to \tau^+e^-$	POWHEG + PYTHIA	290000	0.59753	1.0680	1.0
126931	$W^+W^- \to e^+\mu^-$	POWHEG + PYTHIA	299999	0.59772	1.0676	1.0
126932	$W^+W^- \to \mu^+\mu^-$	POWHEG + PYTHIA	299999	0.59724	1.0685	1.0
126933	$W^+W^- \to \tau^+\mu^-$	POWHEG + PYTHIA	300000	0.59737	1.0682	1.0
126934	$W^+W^- \to e^+\tau^-$	POWHEG + PYTHIA	300000	0.59699	1.0689	1.0
126935	$W^+W^- \to \mu^+\tau^-$	POWHEG + PYTHIA	299999	0.59770	1.0677	1.0
126936	$W^+W^- \to \tau^+\tau^-$	POWHEG + PYTHIA	299999	0.59759	1.0679	1.0

Table 6.4: MC samples for backgrounds that require fake leptons from jets to pass selection. The generator used, the number of simulated events, k-factor, and the corresponding cross-sections times branching ratios and generator filter efficiency are shown. These samples are used only as a cross check to the data-driven background estimation.

MCID	Process	Generator	Events	$\sigma\times$ B [pb]	k-factor	ϵ_{filter}
110001	$t\bar{t}$ (dilepton filter)	MC@NLO	9977338	207.68	1.146	0.105
117360	t-channel $\to e$	ACERMC	299999	8.5878	1.1037	1.0
117361	t-channel $\to \mu$	ACERMC	299999	8.5889	1.1035	1.0
117362	t-channel $\to \tau$	ACERMC	299999	8.5810	1.1045	1.0
108346	$W\ t$	MC@NLO	198387	20.666	1.0825	1.0
108343	s-channel $\to e$	MC@NLO	199899	0.56495	1.0744	1.0
108344	s-channel $\to \mu$	MC@NLO	199899	0.56430	1.0737	1.0
108345	s-channel $\to \tau$	MC@NLO	199799	0.56434	1.0736	1.0

Table 6.5: MC samples for backgrounds that require fake leptons from jets to pass selection. The generator used, the number of simulated events, k-factor, and the corresponding cross-sections times branching ratios and generator filter efficiency are shown. These samples are used only as a cross check to the data-driven background estimation.

MCID	Process	Generator	Events	$\sigma\times$ B [pb]	k-factor	ϵ_{filter}
107680	$W \to e\nu + 0jets$	ALPGEN + HERWIG	3459894	8136.8	1.1330	1.0
107681	$W \to e\nu + 1jet$	ALPGEN + HERWIG	2499491	1791.5	1.1330	1.0
107682	$W \to e\nu + 2jets$	ALPGEN + HERWIG	3769487	541.60	1.1330	1.0
107683	$W \to e\nu + 3jets$	ALPGEN + HERWIG	1009997	146.65	1.1330	1.0
107684	$W \to e\nu + 4jets$	ALPGEN + HERWIG	249999	37.334	1.1330	1.0
107685	$W \to e\nu + 5jets$	ALPGEN + HERWIG	70000	11.355	1.1330	1.0
107690	$W \to \mu\nu + 0jets$	ALPGEN + HERWIG	3469692	8133.4	1.1330	1.0
107691	$W \to \mu\nu + 1jet$	ALPGEN + HERWIG	2499694	1792.7	1.1330	1.0
107692	$W \to \mu\nu + 2jets$	ALPGEN + HERWIG	3769886	541.27	1.1330	1.0
107693	$W \to \mu\nu + 3jets$	ALPGEN + HERWIG	1006698	146.49	1.1330	1.0
107694	$W \to \mu\nu + 4jets$	ALPGEN + HERWIG	254999	37.341	1.1330	1.0
107695	$W \to \mu\nu + 5jets$	ALPGEN + HERWIG	69900	11.364	1.1330	1.0
107700	$W \to \tau\nu + 0jets$	ALPGEN + HERWIG	3419992	8135.7	1.1330	1.0
107701	$W \to \tau\nu + 1jet$	ALPGEN + HERWIG	2499793	1793.7	1.1330	1.0
107702	$W \to \tau\nu + 2jets$	ALPGEN + HERWIG	3765989	541.24	1.1330	1.0
107703	$W \to \tau\nu + 3jets$	ALPGEN + HERWIG	1009998	146.48	1.1330	1.0
107704	$W \to \tau\nu + 4jets$	ALPGEN + HERWIG	249998	37.344	1.1330	1.0
107705	$W \to \tau\nu + 5jets$	ALPGEN + HERWIG	65000	11.477	1.1330	1.0
107280	$W \to \ell\nu + b\bar{b} + 0jets$	ALPGEN + HERWIG	474997	52.255	1.1330	1.0
107281	$W \to \ell\nu + b\bar{b} + 1jet$	ALPGEN + HERWIG	359500	45.540	1.1330	1.0
107282	$W \to \ell\nu + b\bar{b} + 2jets$	ALPGEN + HERWIG	174898	23.671	1.1330	1.0
107283	$W \to \ell\nu + b\bar{b} + 3jets$	ALPGEN + HERWIG	50000	12.525	1.1330	1.0
117284	$W \to \ell\nu + c\bar{c} + 0jets$	ALPGEN + HERWIG	1274900	143.07	1.1330	1.0
117285	$W \to \ell\nu + c\bar{c} + 1jet$	ALPGEN + HERWIG	1049994	143.68	1.1330	1.0
117286	$W \to \ell\nu + c\bar{c} + 2jets$	ALPGEN + HERWIG	524900	80.762	1.1330	1.0
117287	$W \to \ell\nu + c\bar{c} + 3jets$	ALPGEN + HERWIG	169500	35.932	1.1330	1.0
117293	$W \to \ell\nu + c + 0jets$	ALPGEN + HERWIG	6489580	758.93	1.5200	1.0
117294	$W \to \ell\nu + c + 1jet$	ALPGEN + HERWIG	2069796	274.24	1.5200	1.0
117295	$W \to \ell\nu + c + 2jets$	ALPGEN + HERWIG	519998	71.634	1.5200	1.0
117296	$W \to \ell\nu + c + 3jets$	ALPGEN + HERWIG	110000	16.425	1.5200	1.0
117297	$W \to \ell\nu + c + 4jets$	ALPGEN + HERWIG	19900	4.7468	1.5200	1.0

Chapter 7

Event Selection

Events are selected to ensure an inclusive and pure sample of WZ to lepton decays. The data quality ensured by the use of a good run list is further corrected for specific issues that arose during the data-taking period. A single electron or muon trigger defines the sample on which further cuts are made. From this sample, three high quality, isolated leptons are required. Two of these leptons are required to be consistent with a leptonic Z boson decay. The third lepton and the missing transverse energy in the event are assumed to come from a leptonic W boson decay. By assuming that the W boson produced an on-shell decay, the full W boson kinematics can be calculated, and thus, a full WZ invariant mass can be constructed.

The data for this analysis were collected between April and September of 2012. These data are further subjected to a number of data quality cuts, ensuring that the all elements of the detector needed for object reconstruction were operating properly. These requirements define a *good run list*, which selects an integrated luminosity of 13.0 fb^{-1} of data from this period on which the analysis is performed. The data are categorized into `egamma` and `muon` stream, based on which trigger was fired. Events in the `muon` stream that pass the specific muon trigger for this analysis are kept. Events in the `egamma` stream that pass the electron trigger and fail the muon trigger are kept.

A number of other data quality requirements are imposed beyond the good run list. The trigger, timing, and control system at times required a restart in certain period to recover from a busy state. These restarts could produce incompletely reconstructed events in the following minutes, so such events are removed. Events containing a LAr noise burst, where coherent noise affects a significant fraction of the calorimeter, are removed. Events with corrupt output from the tile calorimeter are removed.

7.1 Jet Cleaning

Because of the reliance of this analysis on missing transverse energy, it is important that calorimeter performance does not impede the overall data quality. This section details two

data quality issues that occurred during data taking that did not result in vetoing events via the good run list, but nonetheless needed to be addressed.

In part of May 2012, an unmasked hot tile calorimeter cell was included in the data described above. To minimize the effect of this hot cell, events with a jet pointing near this cell are considered. If such a jet has its highest energy fraction in the second tile layer and that layer contains $E_{\text{layer}}/E_{\text{jet}} > 0.6$, the event is removed.

For most of July 2012, improper high voltage powering of a part of the forward calorimeter resulted in poor performance in that region. To minimize the effect of this problematic region, events with a jet of $p_T > 20$ GeV pointing towards this region are removed.

Additionally, a fraction of the Monte Carlo corresponding to the fraction of data affected by these issues is checked for jets in these kinematic regions. Monte Carlo events assigned to this fraction that fail these cuts are also removed.

7.2 Trigger

Because interesting signals in this analysis will come from high mass resonances decaying to high p_T leptons, the data for this analysis are selected using unprescaled single lepton triggers from the 2012 LHC run. For both electrons and muons, a low-threshold, isolated trigger is combined with a high-threshold, non-isolated trigger. This combination is done to ensure a sufficiently low threshold for leptons used in the analysis along with high efficiency for high p_T objects, where the isolated triggers can become inefficient. A table of the EF triggers and full trigger train used can be seen in Table 7.1. The `EF_mu24i_tight` and `EF_e24vhi_medium1` entries are for the isolated muon and electron triggers, respectively, with a threshold of 24 GeV each. The `EF_mu26_tight` and `EF_e60_medium1` entries are for non-isolated muons and electrons, with thresholds of 26 and 60 GeV, respectively.

Event Filter	Level 2	Level 1
EF_mu24i_tight	L2_mu24_tight	L1_MU15
EF_mu26_tight	L2_mu36_tight	L1_MU15
EF_e24vhi_medium1	L2_e24vhi_medium1	L1_EM18VH
EF_e60_medium1	L2_e60_medium1	L1_EM30

Table 7.1: Single lepton triggers and respective trigger chain

The full requirements of the trigger closely resemble the trigger definitions from 2011 [84] [85], although particular energy thresholds have changed to accommodate the increased luminosity in the 2012 run.

7.3 Pileup Reweighting

The Monte Carlo used for this analysis is generated with additional minimum bias interactions overlaid on the hard scatter in the event. This overlay models the often significant number of multiple interactions per bunch crossing. These additional interactions contribute tracks and calorimeter energy to the event. Therefore, a proper modeling in Monte Carlo of the true pileup behavior is important, particularly for the accurate reconstruction of missing transverse energy, which can depend significantly on the behavior of unclustered energy in the calorimeter. The distribution of $< \mu >$ in the data is shown in Figure 7.1

The distribution of mean number of interactions per bunch crossing, $< \mu >$, cannot be set perfectly when Monte Carlo events are generated. Instead, $< \mu >$ is recorded for each Monte Carlo event. Knowing the full distribution of $< \mu >$ for the Monte Carlo sample and the dataset being used in the analysis, events are reweighted so that the Monte Carlo has the same $< \mu >$ distribution as the data.

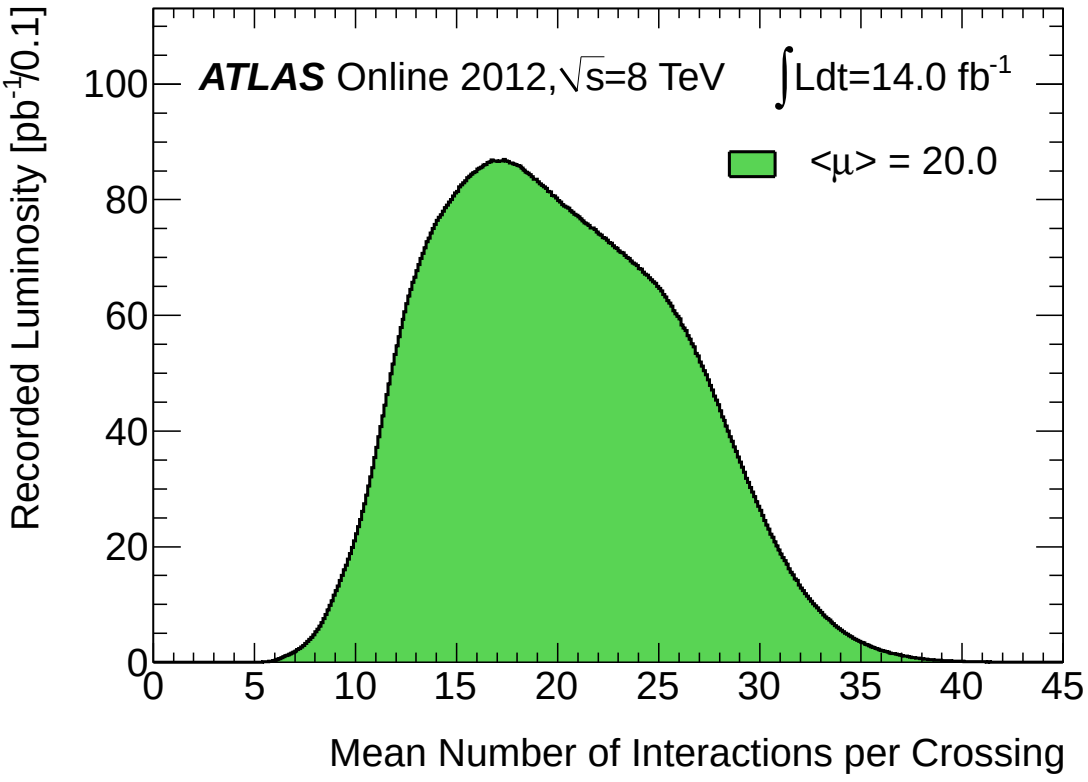

Figure 7.1: The luminosity-weighted average interactions per bunch crossing during data-taking in 2012 until September [6]

7.4 Electrons

7.4.1 Electron Selection

Electrons are required to be reconstructed by the cluster-based electron algorithm, described in Section 5.4, and *not* also reconstructed by the conversion electron, forward electron, or photon reconstruction algorithms. Reconstructed electrons are selected only within the fiducial region of the EM calorimeter, $|\eta| < 2.47$, and not in the transition region between the EM calorimeter barrel and endcap, $1.37 < |\eta| < 1.52$. This transition region shows degraded electron performance because of the large amount of material in front of the first calorimeter layers. The electron η and ϕ are measured using information from the associated track if that track contains at least four hits in the pixel and SCT detectors. Otherwise, these coordinates are taken from the energy cluster in the calorimeter.

Reconstructed electrons are required to pass a set of object quality cuts. Electron candidates are removed if the associated calorimeter cluster is affected by a dead front end board in the first or second sampling, a dead high voltage region in any sampling, or a masked cell in the core of the cluster. Electrons associated to the Z decay are required to pass the *medium* electron cuts, described in Section 5.4. Electrons associated with a W decay are required to pass the *tight* electron cuts described in that section. The looser requirements for the Z-decay leptons are appropriate because the requirement that those two electrons form an object with mass close to m_Z reduces the level of background.

A number of requirements are made on the track associated with an electron. These requirements help ensure that a reconstructed electron comes from the primary vertex. If the electron track crosses a live part of the innermost pixel layer, a hit is required in that layer. The distance of closest approach, z_0, of the electron track to the primary vertex in the z direction is required to satisfy $|z_0 sin(\theta)| < 0.4$ mm. The distance of closest approach of the track in the transverse direction, d_0, is required to satisfy $|d_0/\sigma(d_0)| < 3$, where $\sigma(d_0)$ is the uncertainty in the d_0 track parameter.

To ensure that electrons used in this analysis are not coming from secondary decays inside jets or from pathological jets that fake the appearance of an electron, calorimeter-based and track-based isolation requirements are applied to reconstructed electrons. The sum of the p_T of tracks in the cone $|\Delta(R)| < 0.3$ around the electron track must be less than $0.16 \times E_{T,ele}$, where $\Delta(R) = \sqrt{\Delta(\eta)^2 + \Delta(\phi)^2}$. The corrected sum of calorimeter energy in the cone $|\Delta(R)| < 0.3$ around the electron cluster must be less than $0.16 \times E_{T,ele}$. The raw calorimeter energy in this cone must be corrected both for the leakage of the electron energy deposition outside the cone and for energy from the underlying event and pileup interactions. The effect of pileup on this isolation is corrected based on the number of vertices reconstructed in the event.

7.4.2 Corrections to Electron Efficiency

Because the simulated electron performance does not perfectly match the measured electron performance, corrections to the electron efficiency are applied in Monte Carlo. The corrections, described more completely in [10], are derived using $Z \rightarrow ee$ events. These measurements have since been updated and corrections for 2012 data have been used, e.g., in [15].

The electron efficiency correction has three components: a reconstruction efficiency to match an electromagnetic cluster to a track in the Inner Detector; an identification efficiency for an electron to pass the necessary identification cuts to be classified as, e.g., *medium*; and an isolation efficiency for an electron to pass the requirements limiting track and calorimeter activity around the object. Each component of these efficiency corrections is measured separately from the others and in bins of η and p_T. Differences between the measured efficiency and the expectation from Monte Carlo are used to derive efficiency scale factors.

The electron reconstruction efficiency is measured in $Z \rightarrow ee$ data. Events are selected with a *tight* tag electron and a dielectron invariant mass between $80 - 100$ GeV. Probe reconstruction efficiency is measured with respect to sliding window clusters in the EM calorimeter. The resulting electron reconstruction efficiency compared to Monte Carlo is shown in Figure 7.2 for reconstruction only and after track hit requirements are applied.

The electron identification efficiency is measured using a similar tag-and-probe method in $Z \rightarrow ee$ events. The identification efficiency is measured with respect to electron objects. The resulting identification efficiency can be measured for both *medium* and *tight* electrons, shown in Figure 7.3. Structure in the *tight* identification efficiency reflects the dependence of those cuts on tracking variables, which are sensitive to interaction with material in the ID. Electron isolation scale factors are derived using a similar tag-and-probe method and are O(1%) for the objects used in this analysis.

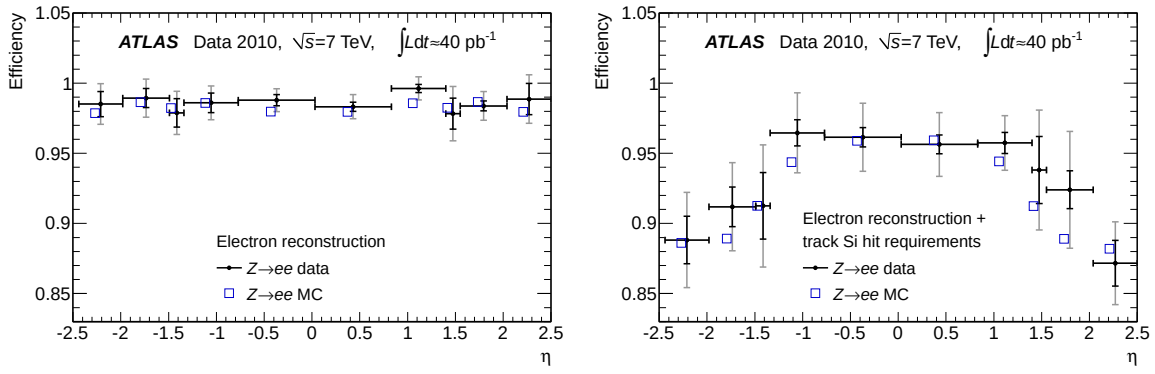

Figure 7.2: Electron reconstruction efficiency in data and MC, for reconstruction only (left) and reconstruction with track hit requirements (right) [10]

7.4.3 Corrections to Electron Energy

As with the electron efficiency, the electron energy performance in simulation does not perfectly match the measured electron performance. Again, a set of corrections is derived in $Z \to ee$ events to correct the electron energy scale and resolution.

Electron energy scale performance is evaluated in-situ using $Z \to ee$ events [10]. Events are selected with two *medium* electrons where the di-electron invariant mass is $80-100$ GeV. The $Z \to ee$ mass peak, seen in Figure 7.4 is compared to Monte Carlo. Miscalibration of electron energy skews the position and shape of the Z mass peak. Corrections to the electron energy scale are parametrized as a function of η:

$$E^{\text{measured}} = E^{\text{true}}(1 + \alpha(\eta)). \tag{7.1}$$

This parametrization is used because of the strong effect of ID material on electron performance. The linearity of this correction in E_T is also checked using $J/\psi \to ee$ events and $W \to e\nu$ events.

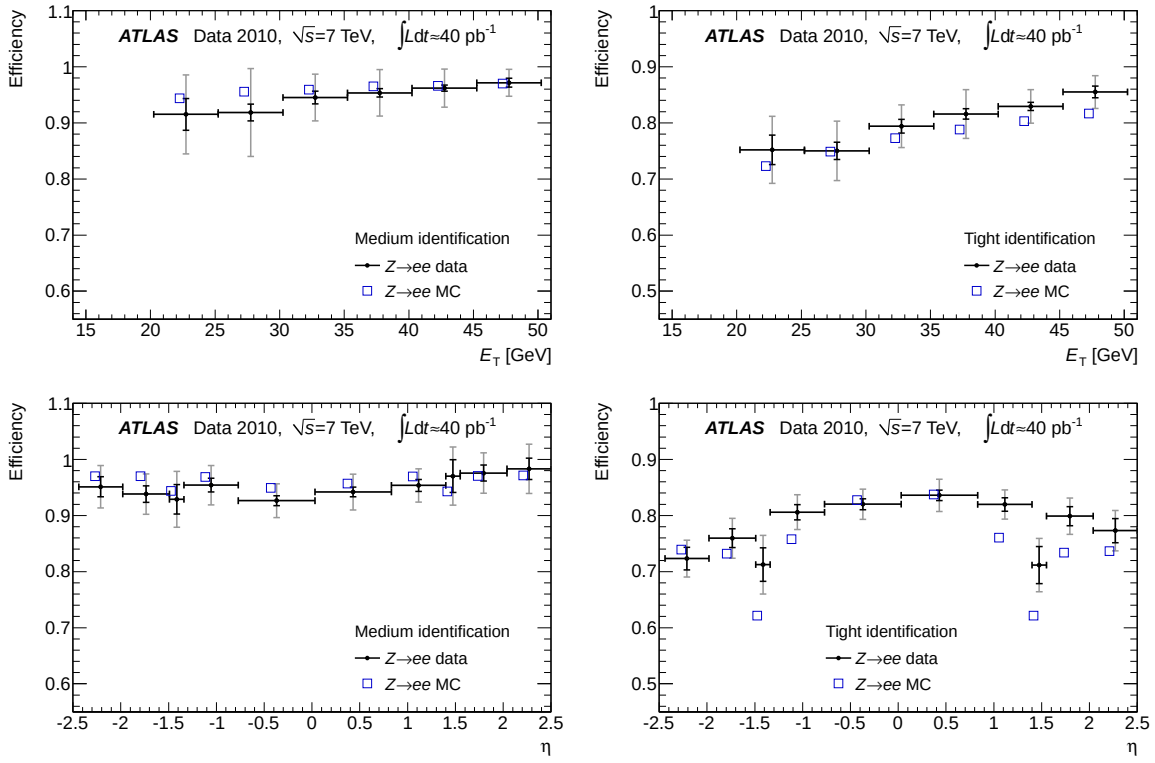

Figure 7.3: Electron identification efficiency in data and MC for *medium* electrons vs E_T (top left), *tight* electrons vs E_T (top right) *medium* electrons vs η (bottom left), and *tight* electrons vs η (bottom right) [10]

A similar Z selection is used to calculate an electron resolution correction. The Z line shape from electrons, shown in Figure 7.4, is fit to a Breit-Wigner function convoluted with a Crystal Ball function. The Breit-Wigner parameters are fixed to the measured Z parameters, while the Crystal Ball width is used to describe the experimental resolution. The difference between simulated and measured electron energy resolution is applied as a correction to individual electrons in Monte Carlo:

$$E^{\text{smeared}} = E^{\text{original}} \times \mathcal{N}(\mu, \sigma_{\text{corr}}) \tag{7.2}$$

$$\sigma^2_{\text{corr}} = \sigma^2_{\text{data}} - \sigma^2_{\text{MC}}, \tag{7.3}$$

smearing them to match the Monte Carlo resolution to the measured resolution.

7.5 Muons

7.5.1 Muon Selection

Muons are required to be reconstructed by the STACO algorithm [67] and to be *combined* as described in Section 5.5 with an Inner Detector track. Reconstructed muons are selected only within the tracking volume of the detector, $|\eta| < 2.5$. In order to ensure that a good quality ID track is associated with a muon, requirements are imposed on the ID track:

- At least one hit in the innermost layer if the track crosses a live element of that layer.
- At least one pixel hit or traversed dead module.

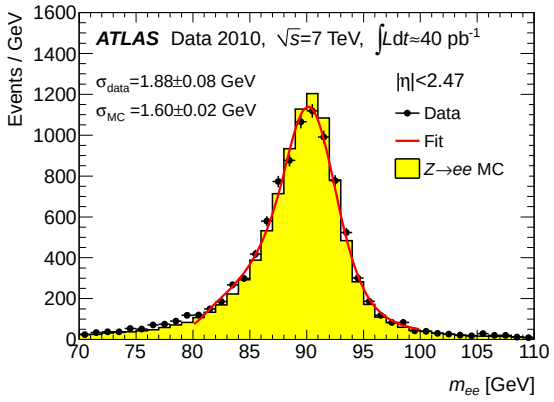

Figure 7.4: $Z \to ee$ lineshape in Monte Carlo and 2010 data. The difference in resolution is used to correct the electron resolution in Monte Carlo. A similar fit is performed to derive corrections in the 2012 data. [10]

- At least five SCT hits or traversed dead modules.
- Less than three holes in the pixel and SCT layers.
- For tracks with $0.1 < |\eta| < 1.9$: At least five hits or outliers in the TRT, with less than 10% of those points being outliers.
- For tracks with $|\eta| < 0.1$ or $|\eta| > 1.9$ and at least five hits or outliers in the TRT: Less than 10% of TRT points being outliers.

To ensure that the ID track for the muon originates from the primary vertex, requirements on the impact parameter are imposed. The longitudinal impact parameter is required to satisfy $|z_0 sin(\theta)| < 1$ mm|. The transverse impact parameter is required to satisfy $|d_0/\sigma(d_0)| < 3$.

To ensure that muons are the well reconstructed product of a hard scatter rather than the result of decays inside of jets, muons are required to be isolated from both other tracks in the event and from energy in the calorimeter. The corrected calorimeter energy within a cone of $\Delta(R) < 0.3$, $E_{T,\text{cone30}}$, must satisfy: $E_{T,\text{cone30}}/p_T < 0.2$ and $E_{T,\text{cone30}}/p_T < 0.014 \times p_T[\text{GeV}] - 0.15$, where p_T is the muon transverse momentum. The calorimeter energy here is corrected both for the effects of pileup, based on the number of vertices in the event, and for the energy deposition of the muon itself. The transverse momentum of tracks within a cone of $\Delta(R) < 0.3$, $p_{T,\text{cone30}}$, must satisfy: $p_{T,\text{cone30}}/p_T < 0.15$ and $p_{T,\text{cone30}}/p_T < 0.01 \times p_T[\text{GeV}] - 0.105$.

As with electron efficiency and resolution, muon efficiency and resolution are corrected in Monte Carlo using measurements from Z tag-and-probe studies [11] [86]. As with the electron corrections, these corrections have been updated since the publication of the above references. Updated results have been used used in, e.g., [15].

7.5.2 Corrections to Muon Efficiency

The muon efficiency correction has two components: a reconstruction efficiency to match an ID track to a muon candidate and an isolation efficiency for a prompt muon to pass the isolation requirements described above. A full description of the method used to obtain muon efficiency scale factors can be found in [11]. These efficiencies are measured in $Z \rightarrow \mu\mu$ events. A good, tag, muon is used to identify an event and a second, probe, muon candidate is used to measure the relevant efficiency. The tag muon and probe muon must have opposite charge and form an invariant mass within 10 GeV of the Z mass peak.

The muon reconstruction efficiency, measured in [11], is the probability that a probe track is matched to a combined muon. The measured reconstruction efficiency is shown in Figure 7.5 . The difference between the efficiency in data and Monte Carlo is used as a scale factor to correct Monte Carlo events.

The muon isolation efficiency, measured in [11], is the probability that a muon satisfies a certain set of calorimeter-based and track-based isolation requirements. Although this analysis uses a different set of isolation requirements from [11], the same tag-and-probe

method is used to measure the isolation efficiency. The difference between muon isolation efficiency in data and Monte Carlo is used as a scale factor to correct Monte Carlo events.

7.5.3 Corrections to Muon Resolution

Muon momentum resolution is also measured in $Z \to \mu\mu$ events [86]. The $Z \to \mu\mu$ lineshape is fit to a function that accounts for the natural decay width and resolution effects from both the ID measurement and muon system measurement of the muon momentum. The difference between momentum resolution in Monte Carlo and momentum resolution in data is used to apply a correction to the two momentum measurements in Monte Carlo. The effect of this correction in the 2012 dataset is shown in Figure 7.6, which shows the Z lineshape before and after muon momentum smearing.

7.6 Boson Selection

Because a single object may pass several object reconstruction algorithms, an overlap removal procedure is applied to ensure that only one physics object is used for each physical object that was in the event. Any electron found within $\Delta R < 0.1$ of a reconstructed muon is removed. If two good electrons are found within $\Delta R < 0.1$ of each other, the lower p_T electron is removed.

An event is required to have three good leptons, as defined above, each with $p_T > 25$ GeV. To reduce contamination from $ZZ \to \ell\ell\ell\ell$, events with a fourth good lepton with $p_T > 20$ GeV are rejected. At least one of the leptons in the event must be geometrically matched to the lepton reconstructed in the trigger algorithm.

After leptons are selected, a Z boson is reconstructed from the opposite sign, same flavor lepton pair that has an invariant mass closest to the Z boson pole mass. The dilepton mass

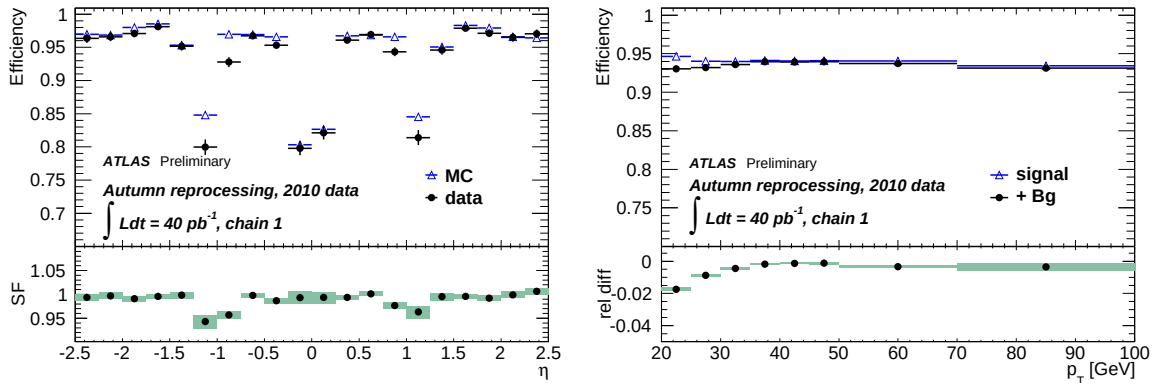

Figure 7.5: Muon reconstruction efficiency in data and MC, vs muon η (left) and muon p_T (right) [11]

so constructed must be within 20 GeV of the Z pole. A relatively large Z mass widow is used for event selection because signal events would have highly boosted leptons that have a worse absolute resolution.

The neutrino from the leptonic W boson decay should give rise to significant missing transverse energy in the event. The missing transverse energy, reconstructed as in Section 5.7, is further corrected for scale and resolution corrections to leptons. The corrected missing transverse energy is required to satisfy $E_T^{miss} > 25$ GeV.

The neutrino p_Z is reconstructed from the "third" lepton, not associated with the Z decay, and the missing transverse energy. If the W boson was precisely on-shell when it decayed, a quadratic constraint on the neutrino p_Z is obtained:

$$(E_\ell + E_\nu)^2 - (p_{x,\ell} + p_{x,\nu})^2 - (p_{y,\ell} + p_{y,\nu})^2 - (p_{z,\ell} + p_{z,\nu})^2 = M_W^2 \tag{7.4}$$

$$E_\ell^2 - p_{x,\ell}^2 - p_{y,\ell}^2 - p_{z,\ell}^2 = M_\ell^2 \tag{7.5}$$

$$E_\nu^2 - p_{x,\nu}^2 - p_{y,\nu}^2 - p_{z,\nu}^2 = M_\nu^2, \tag{7.6}$$

which reduces to:

$$\alpha = \frac{M_W^2 - M_\ell^2}{2} + p_{x,\ell}p_{x,\nu} + p_{y,\ell}p_{y,\nu} \tag{7.7}$$

$$p_{z,\nu}^2(E_\ell^2 - p_{z,\ell}^2) + p_{z,\nu}(-2\alpha p_{z,\ell}) + (E_\ell^2(p_{x,\nu}^2 + p_{y,\nu}^2) - \alpha^2) = 0. \tag{7.8}$$

This equation is quadratic in the neutrino p_z and can be straightforwardly solved. If the solutions are real, the smaller $|p_z|$ is used in the remainder of the analysis. In Monte Carlo

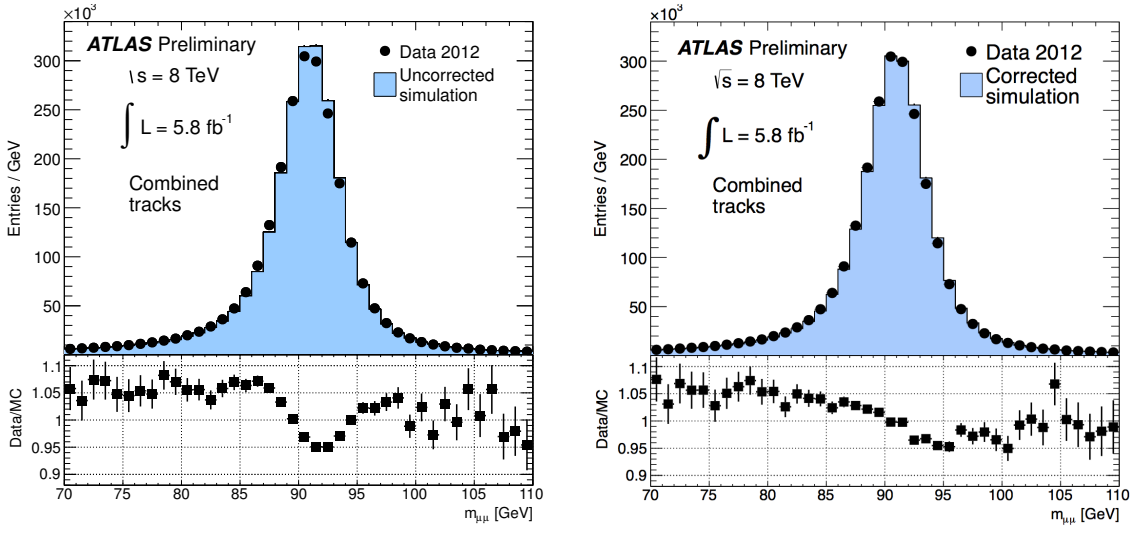

Figure 7.6: $Z \to \mu\mu$ invariant mass before (left) and after (right) muon momentum smearing in Monte Carlo [12]

simulation of an 800 GeV signal, this choice correctly matches the real neutrino p_Z in 70% of events. If the solutions to this equation are complex, the neutrino p_Z is assumed to be the real part of the solution. Events where the W transverse mass is greater than 100 GeV are removed because these events are likely to contain significantly mismeasured lepton momenta or significantly mismeasured missing transverse energy.

With the neutrino p_z so reconstructed, the full W and Z four-vectors are available to the analysis. Angular cuts are placed on the $\Delta\phi$ and Δy between the two bosons. y here refers to the boson rapidity relative to the beam axis,

$$y = \frac{1}{2} ln \frac{E + p_z}{E - p_z}. \tag{7.9}$$

Heavy resonances decaying to WZ tend to give rise to events with back-to-back bosons and similar boson rapidities. Events are selected with $\Delta y(W, Z) < 1.8$ and $\Delta\phi(W, Z) > 2.6$. The distribution of these variables in Monte Carlo is shown in Figure 7.7

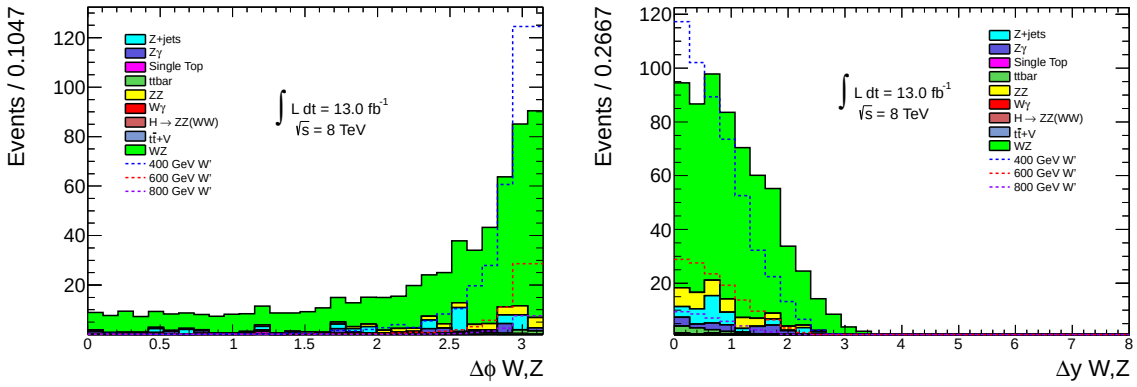

Figure 7.7: Distribution of $\Delta\phi(W, Z)$ (left) and $\Delta y(W, Z)$ (right) from simulated events requiring all cuts except these angular cuts. Resonant WZ production tends to give rise to back-to-back events with similar boson rapidity.

Chapter 8

Control Regions

8.1 Fake Lepton Backgrounds

Because fake leptons from jets are difficult to model properly in Monte Carlo, a data-driven method is used to model backgrounds containing fake leptons from jets. These modeling difficulties are less pronounced for photons faking electrons, where a track is incorrectly matched to the calorimeter cluster of a photon or where a photon converts in the Inner Detector. Therefore, the contribution of events with photons faking electrons is handled separately.

Jets can fake electrons when fragmentation produces a real electron or photon, or when a jet falls into a kinematic tail to look particularly electron-like. Electron identification criteria, described in Section 5.4, and isolation requirements, described in Section 7.4.1, remove the majority of potential fakes. The *medium* and *tight* electron requirements have a jet rejection of 2000 and 8×10^4 respectively [56] for light jets. This jet rejection is degraded in heavy flavor jets, which are more likely to contain real leptons from heavy quark decays.

Truly fake muons from charged hadron misidentification or object punch-through are rare. The majority of muon candidates considered in this section come from real muons that are the result of hadron decays, but that are not part of the hard scatter in the event. The muon isolation isolation requirements, described in Section 5.5, will eliminate fakes from the analysis by vetoing on jet activity near a selected muon. Additionally, the muon d_0 requirements will veto muons from secondary vertices, e.g., from heavy flavor decays inside of a jet.

This analysis will use the term *fake* leptons to refer both to electrons, which are largely algorithmic fakes, and muons, which are largely non-prompt, but real. While the lepton selection has been chosen to limit the contribution of fake leptons, some events with fake leptons will still pass event selection. This analysis uses events with a real Z boson and a third lepton candidate to measure a lepton *fake factor*. The third lepton candidate is likely to come from a fake source, and so is selected as a sample of fake leptons. The fake factor is the ratio of events with a "good" third lepton, which passes all analysis cuts, to events with

a "bad" third lepton, which fails some subset of the analysis cuts,

$$f_\ell = \frac{N_{good\ell}}{N_{bad\ell}}. \tag{8.1}$$

The data sample that passes all other analysis cuts and has two "good" leptons and one "bad" lepton is then scaled by this fake factor to estimate the contamination of the signal region by fake-lepton backgrounds.

Although a very large sample of fake leptons can be selected from dijet events, the success of a data-driven background measurement based on a fake factor relies on the fake factor being the same in the region where it is measured and the region where it is applied. The fake factor will depend on the quark-gluon composition of the relevant jets, the heavy flavor fraction of those jets, the trigger used to select dijet events, the p_T distribution of the resulting leptons, and many other factors. While some of these factors can be corrected for, e.g., by using a fake factor binned in p_T, others are very difficult to understand and correct, e.g., the quark-gluon composition of the relevant jets. To minimize the impact of extrapolating the fake factor from the region where it is measured to the region where it is applied, this analysis uses $Z + jet$ events to measure the predominantly $Z + jet$ fake lepton background. Some extrapolation is still necessary (the fake factor cannot be measured in the same events to which it is applied,) but the uncertainties associated with this extrapolation can be minimized by minimizing the distance of this extrapolation. The analysis of backgrounds from fake leptons is limited to events with a real Z boson, with the fake lepton associated with the W boson decay. The requirement that the Z boson is reconstructed from same flavor, opposite sign pairs of leptons near the Z pole mass removes all but a few events. Limiting this discussion to only the non-Z leptons gives an accurate measurement of the total fake contribution to within 2%, which is negligible compared to other systematics uncertainties associated with these backgrounds.

The fake factor is measured in a region with a Z boson, as defined in the nominal analysis, discussed in Section 7.6, plus a third lepton that does not need to pass the full lepton selection, and a number of additional selection cuts to ensure orthogonal samples and select fake third leptons.

The fake factor for electrons is measured in a region defined by the cuts:

- A Z boson, as defined in the nominal analysis.
- The missing transverse energy cut is reversed, requiring events to have a $E_T^{miss} <$ 25 GeV. This helps to select against Standard Model WZ events, where the real neutrino in the event will tend to produce high missing transverse energy.
- The transverse mass between the missing transverse energy in the event and the third lepton is required to be below 40 GeV. Missing transverse energy and fake leptons will often be collinear, resulting in a small m_T.

- The invariant mass of the three lepton system must be greater than 20 GeV from the Z mass. This requirement removes some of the contamination of events with a Z that emits a mis-reconstructed photon in final state radiation.

A good electron is defined as one that passes all of the analysis cuts, including the *tight* identification requirements for the W decay product, and the track-based and calorimeter-based isolation requirements. A bad electron is defined as one that passes the *medium* identification requirements, but fails either the track-based or calorimeter-based isolation requirements. The distributions of good and bad third electron p_T in this region is shown in Figure 8.1. The distribution of bad electrons comes mostly from fake leptons, with the small contributions from $Z\gamma$, ZZ, and WZ. High pileup during the 2012 run makes it difficult to select a clean sample of good electrons coming from fake sources, even by requiring low missing transverse energy in the event. The statistical uncertainty in the number of good electrons from fake sources after subtracting out the contribution of good electrons from prompt sources in this selection is the dominant uncertainty in the electron fake factor.

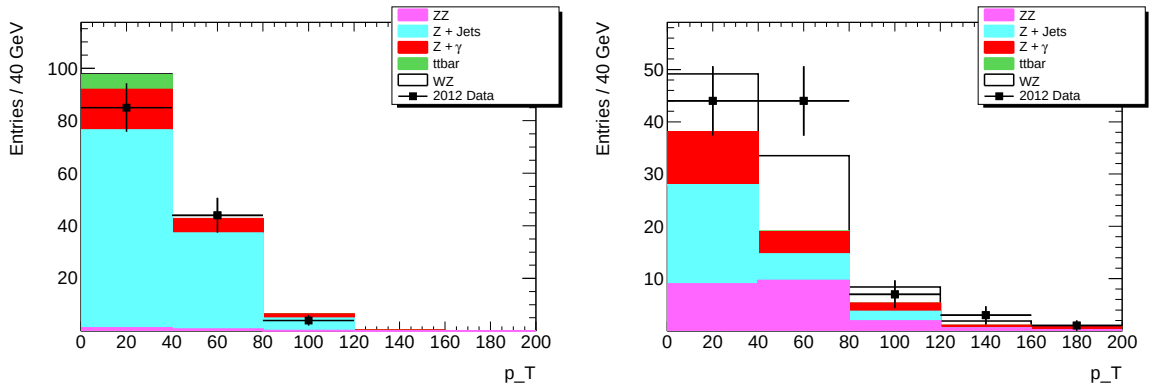

Figure 8.1: Third electron p_T distribution for non-isolated electrons on the left, and isolated electrons on the right. Data points are shown together with Monte Carlo predictions of both fake and prompt leptons. Although the p_T distribution is shown here, only the overall number of events is used in the calculation of the Z tagged fake factor.

For muons, the electron specific cuts are not required. Instead events are selected with Z boson plus a third lepton candidate where the third lepton in the event has a d_0 significance greater than 3.

A good muon in this region passes all of the analysis cuts except the cut on d_0 significance. A bad muon in this region passes all analysis cuts, except on d_0 and isolation, and fails either the calorimeter-based or track-based isolation requirements. The distribution of good and bad muon p_T in this region is shown in Figure 8.2.

The use of d_0 to select a sample of good and bad fake muons provides a pure selection of fake muons compared to the selection of fake electrons. The distribution of lepton d_0 significance in this region is shown in in Figure 8.3, where the removal of prompt muon

contamination from WZ events by use of a d_0 significance cut can be clearly seen. A cut on d_0 tends to select precisely the heavy flavor decays and π/K decay-in-flight events that contribute non-prompt muons to the signal selection. There is, however, a potential bias to this selection if the isolation efficiency of low d_0 fake muons is different from the isolation efficiency of high d_0 fake muons or if the low d_0 region contains muons fakes that are not coming from these processes. The low rate of algorithmic fakes for muon candidates protects this selection somewhat from differing behaving between low d_0 and high d_0 fake muons, and the stochastic nature of hadron decays provides a good reason to trust the consistency between these regions for heavy flavor or decay-in-flight events. These assumptions are not perfect, however. A 35% correction between the fake factor in the low d_0 and high d_0 region is found in simulated $Z + jet$ events and applied to the fake factor that is measure in data.

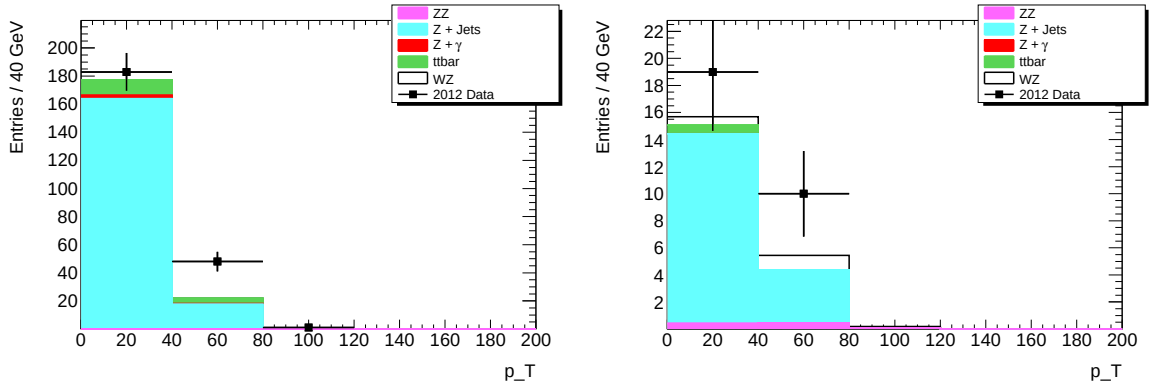

Figure 8.2: Third muon p_T distribution for non-isolated muons on the left, and isolated muons on the right. Data points are shown together with MC predictions for both fake and prompt leptons. Although the p_T distribution is shown here, only the overall number of events is used in the calculation of the Z tagged fake factor.

The fake factor can be constructed from the number of good leptons from fake processes divided by the number of bad leptons from fake processes. Because the fake factor is measured in a region that is contaminated by prompt leptons, the number of leptons from fake processes is assumed to be the number of leptons observed in data, minus the number of leptons expected in Monte Carlo from prompt processes:

$$f_\ell = \frac{N_{\text{good } \ell} - N^{\text{prompt},\gamma}_{\text{good } \ell}}{N_{\text{bad } \ell} - N^{\text{prompt},\gamma}_{\text{bad } \ell}}. \tag{8.2}$$

Because the fake lepton kinematics in the region where the fake factor is measured match closely to the fake lepton kinematics in the region where the fake factor is applied, and because of the limited statistics available for this measurement of the fake factor, no binning is done on this fake factor. Although the use of Z tagging minimizes the error from extrapo-

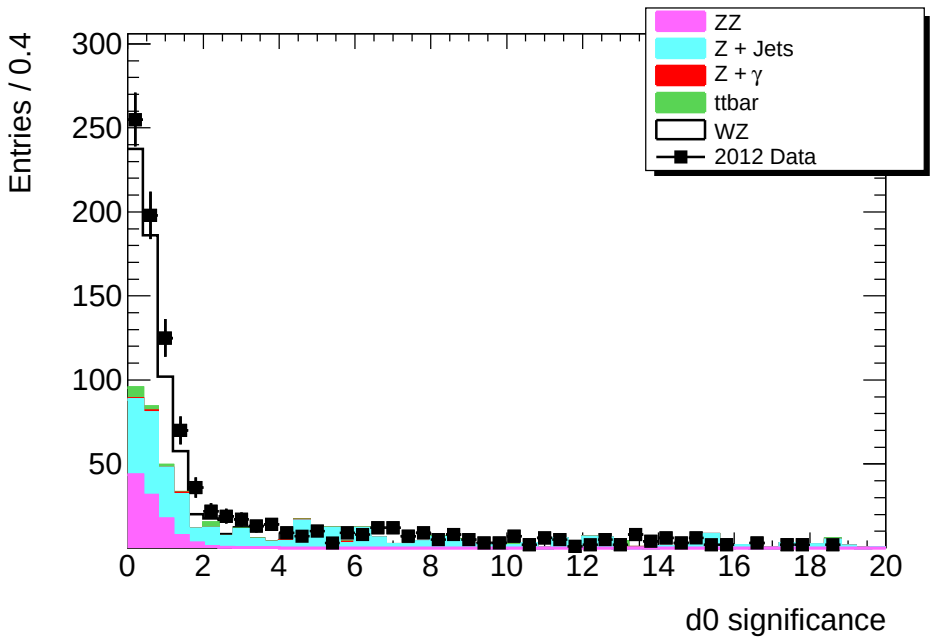

Figure 8.3: Third muon d_0 significance distribution, including data and various processes simulated in Monte Carlo. The fake factor is measured for events with a d_0 significance greater than 3.

lating the fake factor to the region where it is applied, a number of systematic uncertainties are considered:

- The fake lepton in this calculation might be biasing the trigger performance for the event. This bias is checked by recalculating the electron fake factor in $\mu\mu e$ events, using only the muon trigger and by recalculating the muon fake factor in $ee\mu$ events using only the electron trigger. In both cases, the resulting change in the fake factor is $< 1\%$ and considered negligible.

- Because an unbinned fake factor is used, this approach implicitly assumes that the kinematics for bad third leptons from fake sources is a good description of good third leptons from fake sources. This assumption is checked by comparing the p_T distribution of third leptons in a $Z + jet$ Monte Carlo sample. The difference between good and bad third lepton kinematics in this sample is shown in Figure 8.6 for electrons and Figure 8.7 for muons. The average per-bin difference, weighted by the fraction of events in each bin, is 5% for electrons and 2% for muons.

- The electron fake factor is measured in a region with low missing transverse energy and low W transverse mass, and applied in a region with high missing transverse energy, where the fake factor might be different. This difference in fake factor is measured in

$Z + jets$ Monte Carlo events and found to be 5% with an uncertainty of 10% based on which Monte Carlo generator is used. The difference in Monte Carlo is applied as an extrapolation correction to the fake factor in data, and the error is assessed as a systematic uncertainty in the electron fake factor.

- The electron kinematics are assumed to be the same in the region where the fake factor is measured and the region where it is applied. The bias associated with this assumption is measured in $Z + jets$ Monte Carlo by comparing the p_T distributions of third leptons in the low missing energy region and third leptons in the high missing transverse energy region, shown in Figure 8.4. The average per-bin difference between these regions is 3%, weighted by the fraction of events in each bin. This average difference is assessed as a systematic uncertainty in the electron fake factor.

- As discussed above, the muon fake factor is measured in a region with high d_0 significance and applied in a region with low d_0 significance. The difference between the fake factor in these two regions when measured in $Z + jets$ Monte Carlo is 35% with an uncertainty of 15% based on which Monte Carlo generator is used. This correction is applied to the measured muon fake factor in data, and the error is assessed as a systematic uncertainty in the fake factor.

- The muon kinematics are assumed to be the same in the region where the fake factor is measured and the region where it is applied. The bias associated with this assumption is measured in $Z + jets$ Monte Carlo by comparing the p_T distribution of third leptons in the low and high d_0 regions, shown in Figure 8.5. The average per-bin difference between the high d_0 significance and low d_0 significance regions weighted by fraction of events in each bin is 1%.

Using the process and corrections described above, the fake factor is found to be $0.300 \pm 0.129(stat) \pm 0.035(syst)$ for electrons and $0.174 \pm 0.039(stat) \pm 0.028(syst)$ for muons. The relatively large fake factor for electrons is a result of the tight definition of a bad lepton, to pass the *medium* electron identification cuts.

Using the corrected fake factor, the fake lepton contamination of the signal region can be estimated by scaling a control region that passes all of the signal cuts but has a bad lepton, as defined above, associated with the W boson decay. The composition of this region in Monte Carlo and the counts from data is shown in Figure 8.8. Scaling the events with a muon associated with the W decay and events with an electron associated with a W decay by their respective fake factors, the data-driven estimate of the fake lepton backgrounds is shown in Figure 8.9. The total counts in each channel are shown in Table 8.1.

The contribution of events with multiple fake leptons is also considered and found to be O(1%). These contributions are considered negligible for the remainder of this analysis.

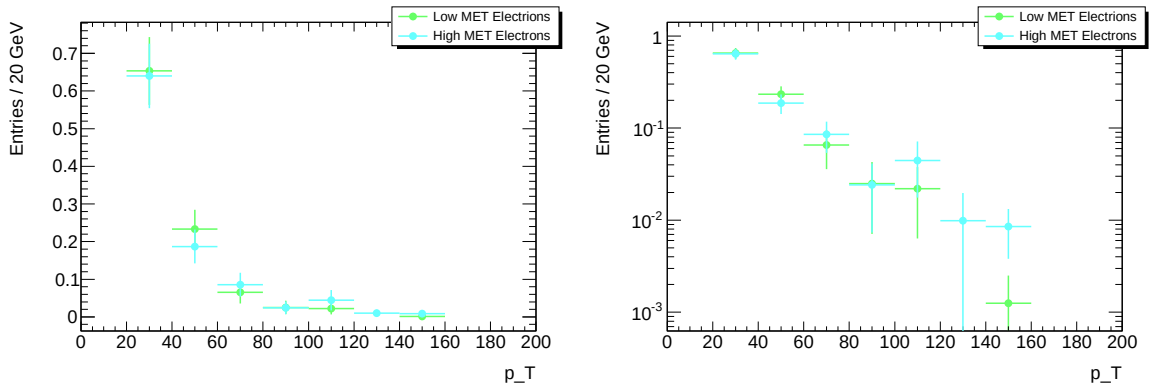

Figure 8.4: Third lepton p_T for events with $E_T^{miss} > 25$ GeV and $E_T^{miss} < 25$ GeV where the third lepton is an electron, on a linear scale (left) and log scale (right) in Z+jets Monte Carlo. Differences between these distributions will give rise to systematic uncertainties is the Z tagged fake factor.

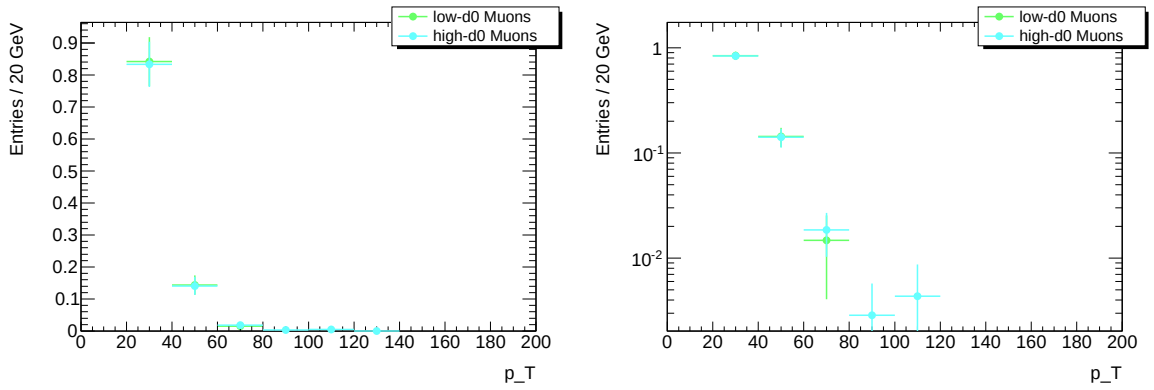

Figure 8.5: Third lepton p_T for events with d_0 significance > 3 and d_0 significance < 3, on a linear scale (left) and log scale (right) in Z+jets Monte Carlo. Differences between these distributions will give rise to systematic uncertainties in the Z tagged fake factor.

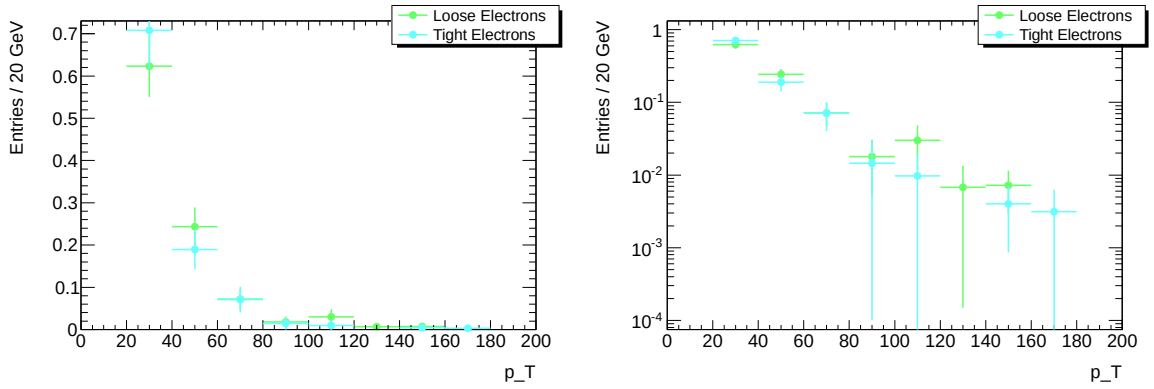

Figure 8.6: Third electron p_T for events with a good third electron and bad third electron, on a linear scale (left) and log scale (right) in Z+jets Monte Carlo. Differences between these distributions will give rise to systematic uncertainties in the Z tagged fake factor.

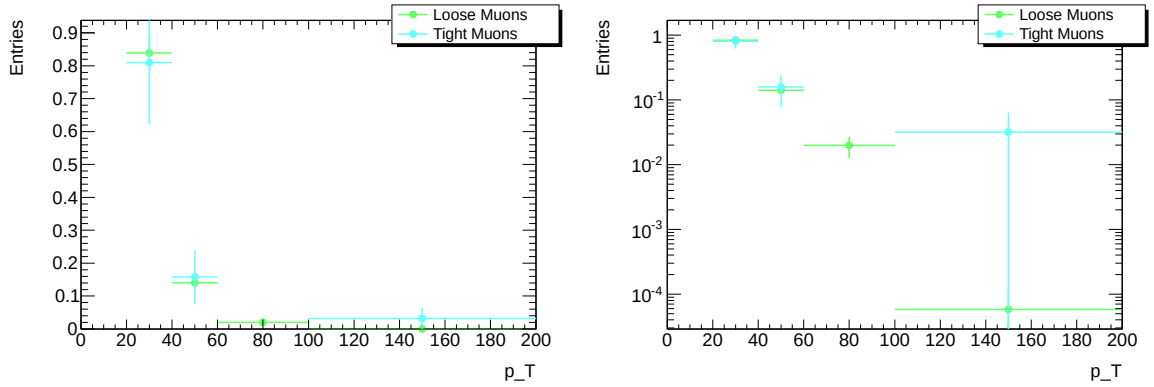

Figure 8.7: Third lepton p_T for events with a good third muon and bad third muon, on a linear scale (left) and log scale (right) in Z+jets Monte Carlo. Differences between these distributions will give rise to systematic uncertainties in the Z tagged fake factor.

8.2 WZ Control Region

The major background to this analysis is Standard Model WZ, the contribution of which is estimated entirely from Monte Carlo. To properly understand this background, a region is defined where the contribution from Standard Model WZ is large, but the effect of any potential signal is small. To avoid any bias on the cuts due to a potential signal contribution, the analysis blinded, restricting any use of the data to this and other control regions. When these control regions are well understood, the analysis is frozen and the signal region is unblinded. The WZ control region is defined by inverting the boson angular cuts described in Section 7.6. Thus, the WZ control region passes all of the signal selection cuts, but requires:

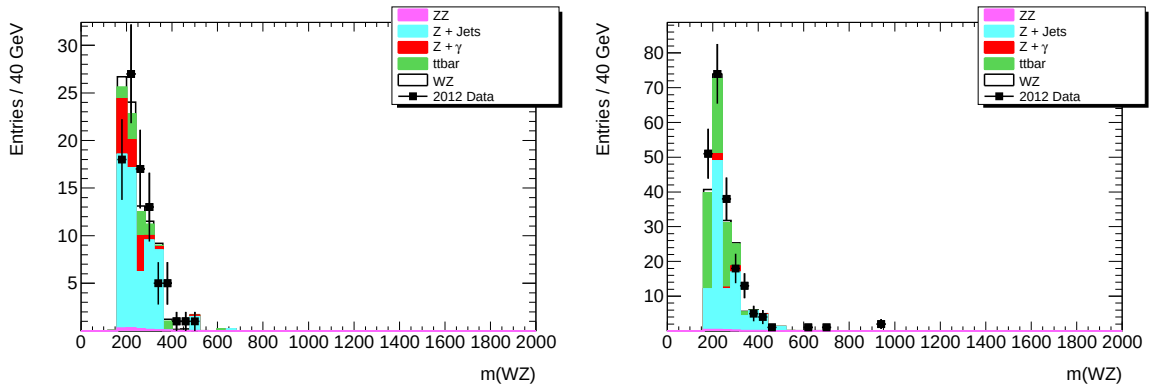

Figure 8.8: Event $M(WZ)$ distribution for events with a bad third electron (left) or muon (right). These distributions are scaled by the electron or muon fake factor (after subtracting out contamination from processes that produce three real leptons) to derive a data-driven estimate of the fake lepton background.

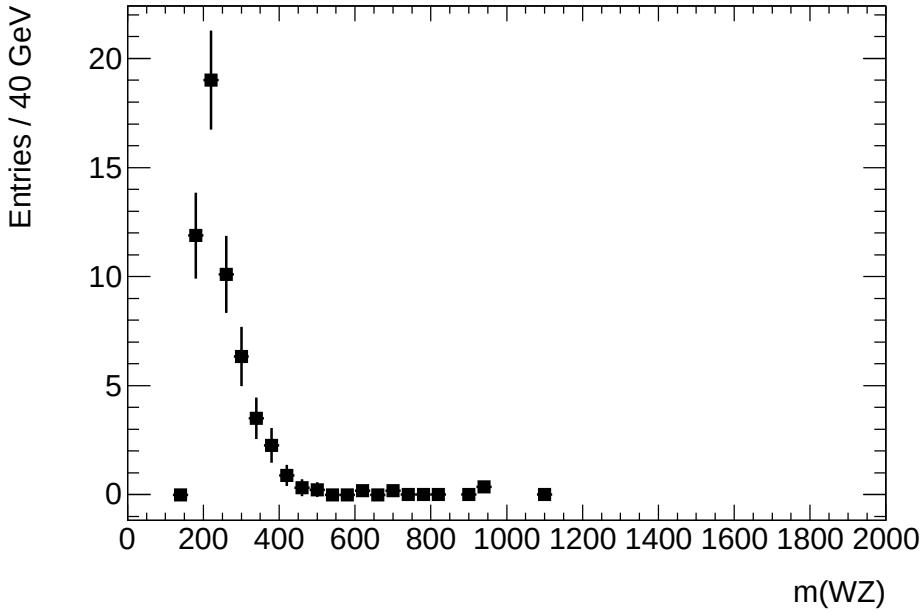

Figure 8.9: Event $M(WZ)$ distribution for the data-driven Z plus jets background estimate combining all lepton channels using the Z tagged fake factor method, including statistical errors for events in the signal region.

Table 8.1: Data-driven estimation of $\ell\ell$+jets background from Z tagged events. Statistical uncertainties are only for statistics in the control region. Statistical uncertainty in the fake factor measurement itself is folded into the systematic uncertainty

.

	$e\nu ee$	$\mu\nu ee$	$e\nu\mu\mu$	$\mu\nu\mu\mu$
WZ Control Region	$8.95 \pm 1.45 \pm 3.98$	$15.19 \pm 1.59 \pm 4.18$	$11.78 \pm 1.67 \pm 5.25$	$19.22 \pm 1.78 \pm 5.29$
Signal Region	$5.36 \pm 1.17 \pm 2.39$	$7.99 \pm 1.15 \pm 2.20$	$15.16 \pm 2.14 \pm 6.75$	$10.04 \pm 1.28 \pm 2.76$

- $\Delta y(W, Z) > 1.8$ or
- $\Delta\phi(W, Z) < 2.6$

These cuts defines a region that is strongly dominated by events coming from the Standard Model WZ process and is orthogonal to the signal selection. Figure 8.10 shows various object kinematics in this control region: The reconstructed Z boson mass, the reconstructed W boson transverse mass, the p_T of the Z boson, the p_T of the W boson, the transverse mass of the WZ system, and the invariant mass of the WZ system. Good agreement is seen between the data and the Standard Model predictions in this region for all of these kinematic variables. Additionally, the agreement in the four lepton-flavor channels is considered for missing transverse energy in Figure 8.11 and for WZ transverse mass in Figure 8.12. The composition of the WZ control region is shown in Table 8.2. Overall, 359 events are observed in the WZ control region, compared to an expected 376 ± 18.4 events from Standard Model processes. The overall event count is in good agreement with expectations from Standard Model processes. The per-channel event counts are also in good agreement with Standard Model processes.

Channel	Data	Total background	WZ	ZZ	$Z\gamma$	$\ell\ell'$+jets (DD)
$e\nu ee$	53	70.7 ± 4.5	50.8 ± 1.4	6.7 ± 0.1	4.3 ± 1.5	8.9 ± 4.0
$\mu\nu ee$	94	88.4 ± 4.5	70.3 ± 1.6	3.9 ± 0.1	0.0 ± 0.0	15.2 ± 4.2
$e\nu\mu\mu$	102	97.1 ± 5.7	75.2 ± 1.5	5.2 ± 0.2	5.0 ± 1.7	11.7 ± 5.2
$\mu\nu\mu\mu$	110	120.6 ± 5.6	95.9 ± 1.7	5.5 ± 0.1	0.0 ± 0.0	19.2 ± 5.3

Table 8.2: Event yields, in the SM WZ control region for the $e\nu ee$, $\mu\nu ee$, $e\nu\mu\mu$, and $\mu\nu\mu\mu$ channels. The theoretical uncertainties in the numbers of the SM predictions are close to 10%, mainly dominated by the uncertainties in the SM inclusive WZ cross section.

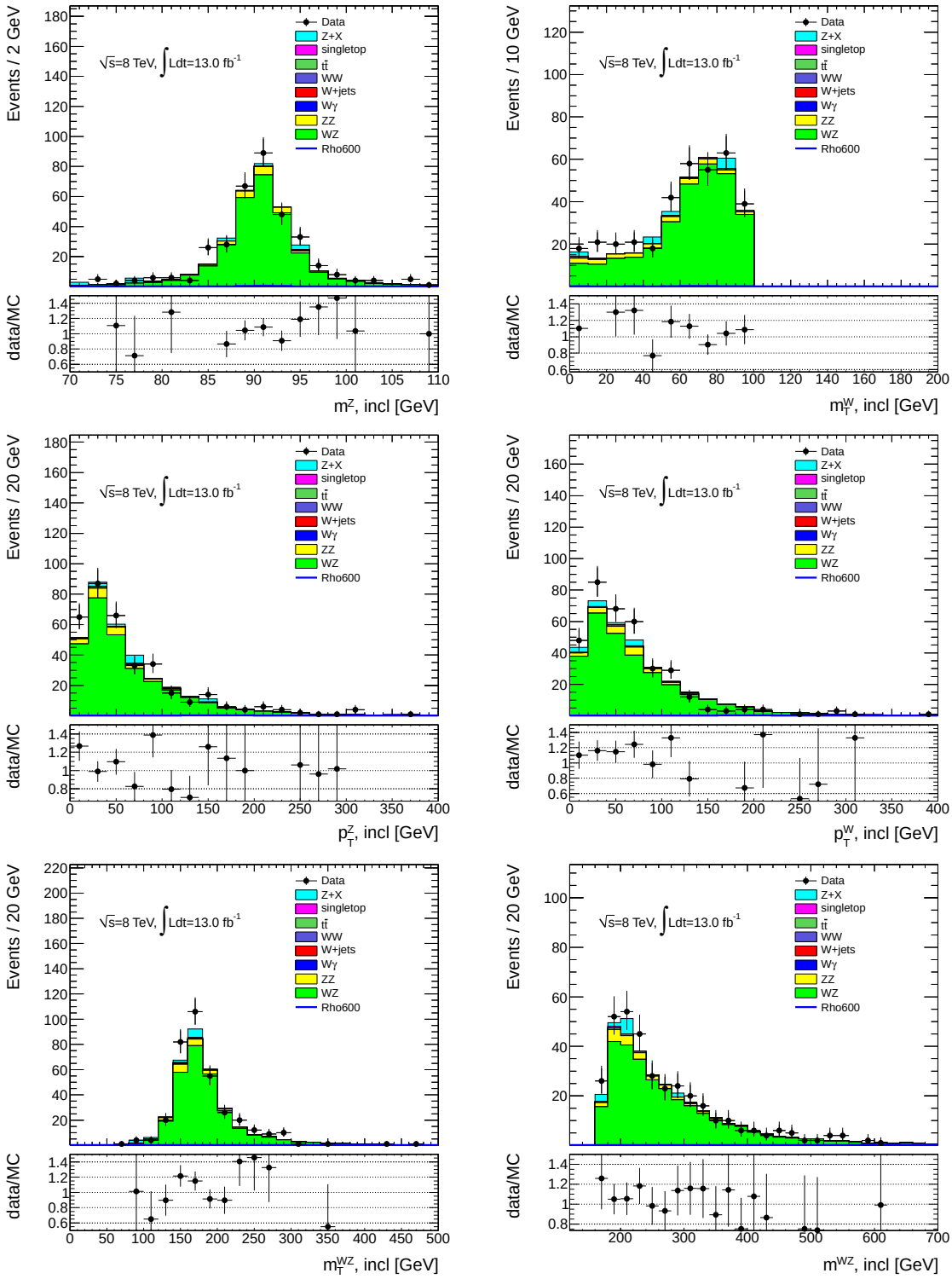

Figure 8.10: Comparison of data with MC prediction for the SM WZ control region for dilepton invariant mass (top left,) W boson transverse mass (top right,) Z p_T (middle left,) W p_T (middle right,) transverse mass of the WZ system (bottom left,) and the invariant mass of the WZ system (bottom right,) distributions. The errors are statistical only.

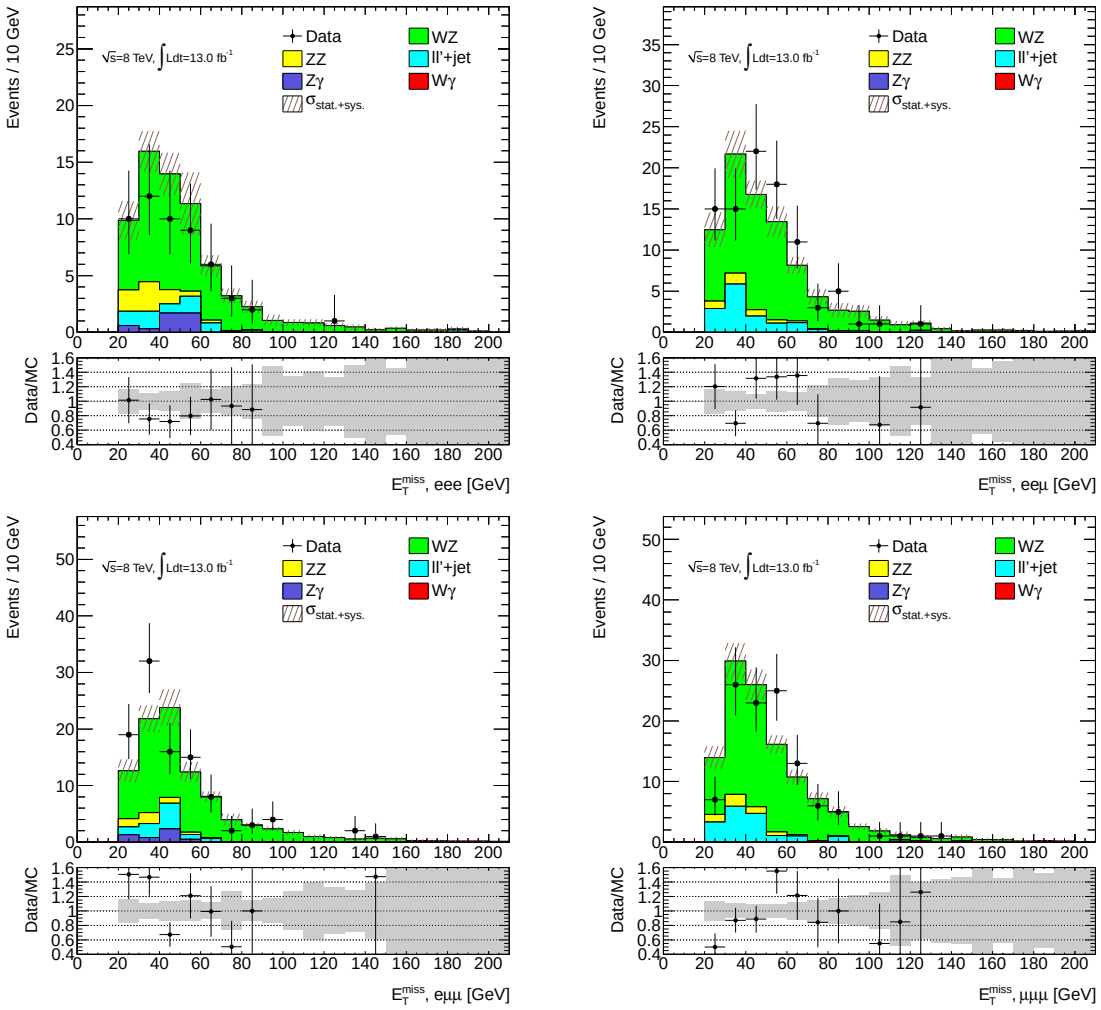

Figure 8.11: Comparison of data with MC prediction for the E_T^{miss} distribution in the SM WZ control region for four individual lepton-flavor channels: $e\nu ee$ (top left,) $\mu\nu ee$ (top right,) $e\nu\mu\mu$ (bottom left,) and $\mu\nu\mu\mu$ (bottom right). The errors are statistical only.

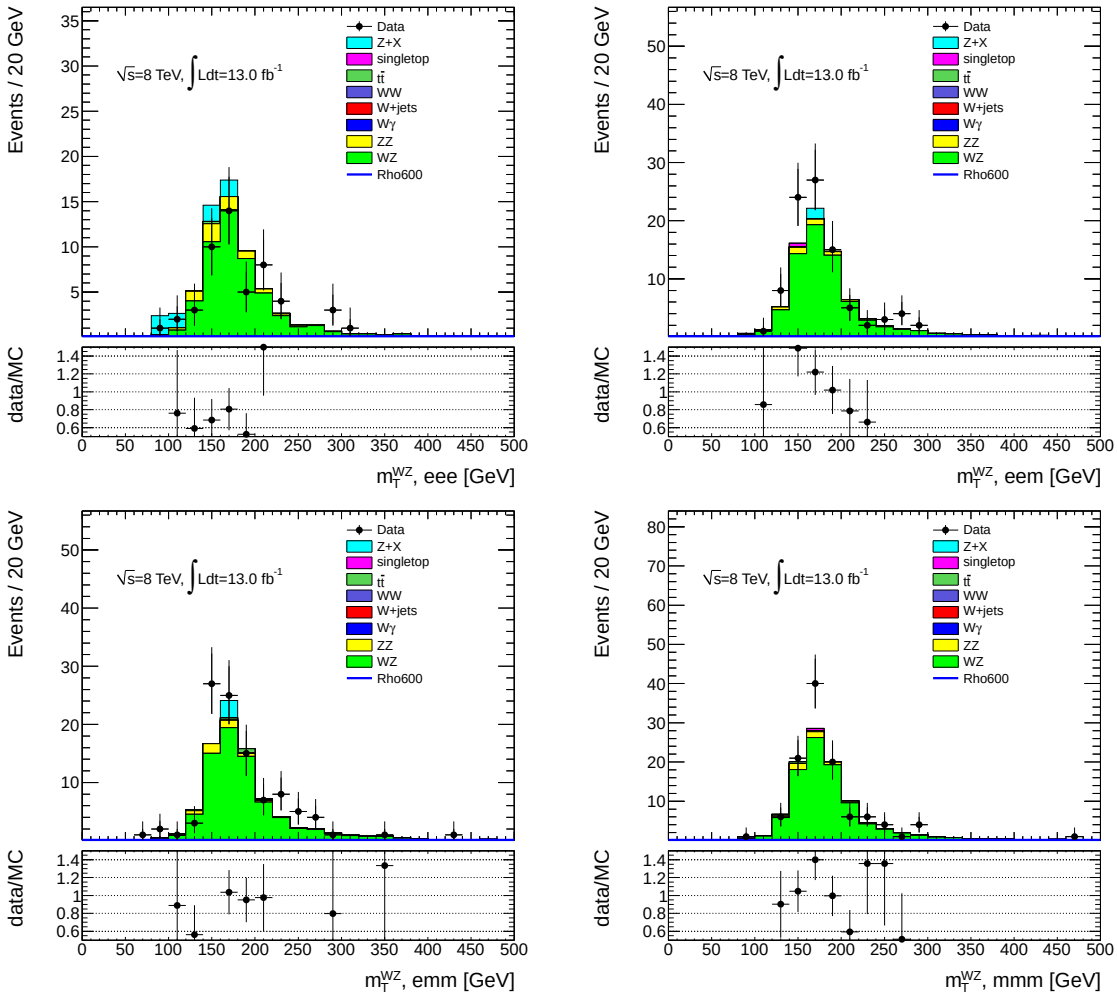

Figure 8.12: Comparison of data with MC prediction for the m_{T}^{WZ} distribution in the SM WZ control region for four individual lepton-flavor channels: $e\nu ee$ (top left,) $\mu\nu ee$ (top right,) $e\nu\mu\mu$ (bottom left,) and $\mu\nu\mu\mu$ (bottom right). The errors are statistical only.

8.2.1 High m_{WZ} in the WZ Control Region

Because any new physics signal is likely to occur in the region of high WZ invariant mass, it is particularly important that the backgrounds in this region are well understood. In addition to considering the event kinematics and event counts in the WZ control region, the high m_{WZ} section of the WZ control region are considered. Figure 8.13 shows the distribution of m_Z and $m_{T,WZ}$ for events with $m_{WZ} > 300$ GeV and $m_{WZ} < 300$ GeV. Unsurprisingly, high WZ invariant mass events tend to have a broader m_Z distribution due to the degraded lepton energy resolution at higher lepton p_T.

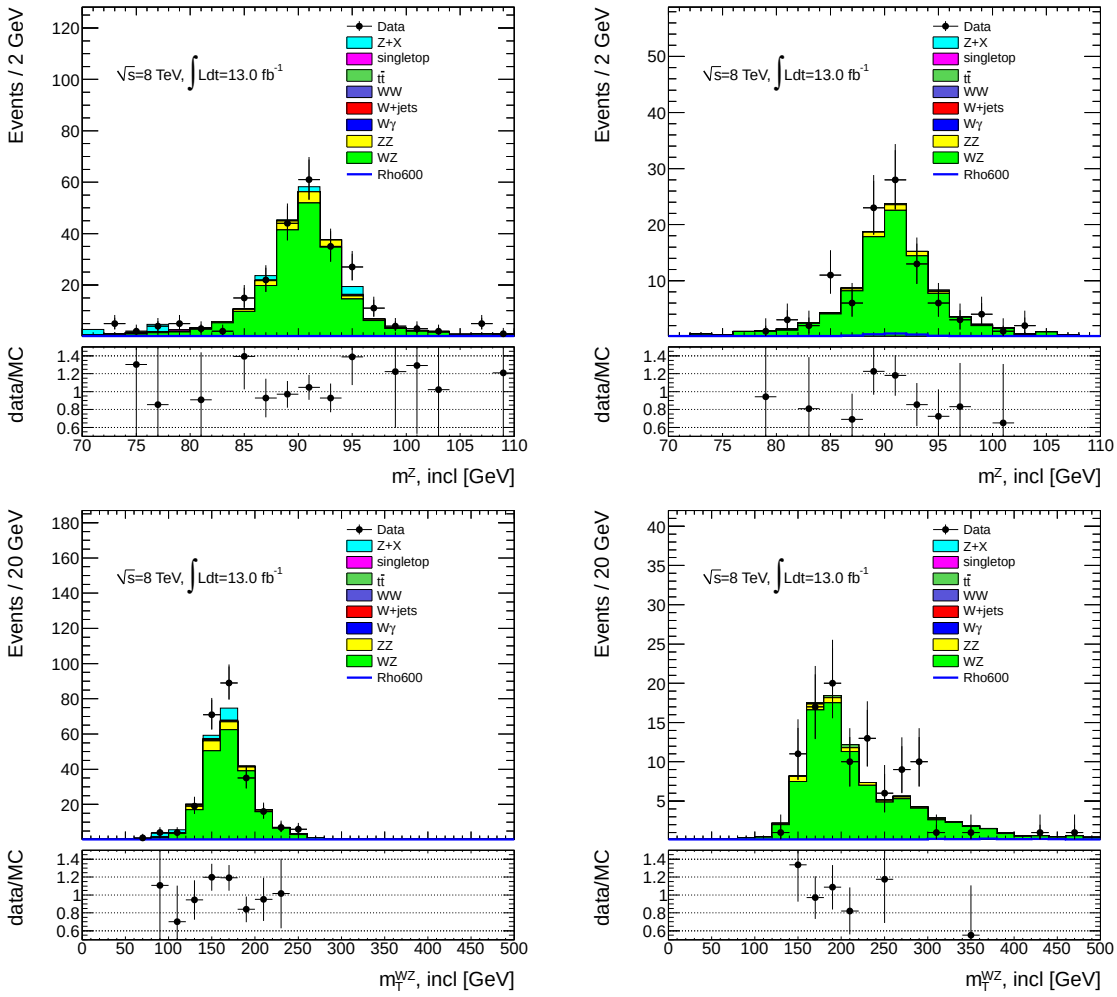

Figure 8.13: Comparison of the events in the SM WZ control region with $m(WZ)$ <300 GeV (left) and with $m(WZ)$ >300 GeV (right) for the combined channel. The plots are the dilepton invariant mass (top row) and the transverse mass of the WZ system (bottom row).

Additionally, the consistency of the high m_{WZ} tail with the expectation from these back-

	$e\nu ee$			$\mu\nu ee$			$e\nu\mu\mu$			$\mu\nu\mu\mu$			inclusive		
Region	Exp.	Obs.	p-value	Exp.	Obs.	p-value	Exp.	Obs.	p-value	Exp.	Obs.	p-value	Exp.	Obs.	p-value
$m(WZ) > 350$ GeV	10.9 ± 4.2	8	0.29	14.1 ± 3.4	17	0.36	17.5 ± 4.2	21	0.34	20.0 ± 4.0	17	0.29	62.5 ± 9.5	63	0.51
$m(WZ) > 400$ GeV	6.2 ± 3.0	6	0.50	9.2 ± 2.6	12	0.34	9.9 ± 3.2	13	0.32	12.5 ± 3.1	12	0.45	37.8 ± 7.1	43	0.33
$m(WZ) > 450$ GeV	4.0 ± 2.6	2	0.24	6.5 ± 2.2	10	0.25	6.2 ± 2.6	6	0.48	8.2 ± 2.5	9	0.53	25.0 ± 5.8	27	0.44
$m(WZ) > 500$ GeV	2.5 ± 2.1	2	0.44	4.2 ± 1.8	7	0.28	4.5 ± 2.2	2	0.15	5.7 ± 2.2	7	0.47	17.0 ± 4.8	18	0.49
$m(WZ) > 550$ GeV	1.7 ± 1.9	1	0.39	3.1 ± 1.5	5	0.36	2.9 ± 1.8	0	0.06	4.0 ± 1.8	5	0.50	11.6 ± 4.2	11	0.46
$m(WZ) > 600$ GeV	1.1 ± 1.5	1	0.53	2.3 ± 1.3	3	0.59	2.1 ± 1.1	0	0.12	2.9 ± 1.5	2	0.31	8.5 ± 3.3	6	0.27
$m(WZ) > 650$ GeV	0.7 ± 0.6	1	0.45	1.4 ± 1.0	2	0.65	1.7 ± 0.9	0	0.19	2.5 ± 1.4	2	0.39	6.2 ± 2.3	5	0.34
$m(WZ) > 700$ GeV	0.4 ± 0.5	1	0.28	0.9 ± 0.8	2	0.50	1.2 ± 0.7	0	0.32	1.9 ± 1.2	2	0.75	4.4 ± 1.9	5	0.56
$m(WZ) > 750$ GeV	0.3 ± 0.4	1	0.23	0.7 ± 0.6	2	0.42	0.9 ± 0.6	0	0.42	1.4 ± 1.0	2	0.65	3.3 ± 1.5	5	0.40
$m(WZ) > 800$ GeV	0.3 ± 0.3	1	0.21	0.5 ± 0.5	1	0.36	0.6 ± 0.5	0	0.53	1.2 ± 0.9	1	0.41	2.6 ± 1.3	3	0.66
$m(WZ) > 850$ GeV	0.1 ± 0.2	1	0.11	0.5 ± 0.5	1	0.32	0.4 ± 0.4	0	0.65	0.9 ± 0.8	0	0.41	1.9 ± 1.1	2	0.78
$m(WZ) > 900$ GeV	0.1 ± 0.1	1	0.08	0.3 ± 0.3	1	0.22	0.3 ± 0.3	0	0.76	0.8 ± 0.7	0	0.45	1.5 ± 0.9	2	0.68

Table 8.3: The observed and expected numbers of events in different $m(WZ)$ regions. The p-value to observe this number of events assuming the background only hypothesis is also shown.

grounds is considered. Table 8.3 lists the per-channel and inclusive event counts above a variety of m_{WZ} cuts in the WZ control region. The p-value[1] to observe the number of data events given the expectation from these backgrounds is listed with the event counts. This p-value accounts for uncertainties in the backgrounds by throwing a number of pseudo-experiments with the Poisson mean varied by the uncertainty associated with that channel. This tail is in good agreement with the expectations from the Standard Model. The smallest p-value observed in the inclusive channel is for events with $m_{WZ} > 600$ GeV where 6 events are observed and 8.5 are expected. The most significant excess in the inclusive channel is for events with $m_{WZ} > 400$ GeV, with a p-value of 0.22, and 43 observed events compared to 37.8 expected.

8.3 Background Extrapolation

Careful consideration is paid to the signal region at high m_{WZ}, where the improved energy and luminosity of this analysis, compared to previous efforts, allow for additional reach. Unfortunately, above ∼800 GeV, the m_{WZ} distribution contains only a few events from Monte Carlo and data-driven backgrounds. Rather than using the events in this region directly, the high mass events are used to parametrize a smooth distribution that is more useful as an input to the limit setting procedure, described in Section 10.2. This parametrization produces a smooth distribution of events in the m_{WZ} tail, even though only limited statistics are available and provides an estimate of the distribution of events into regions where no background events are generated.

For the backgrounds not coming from Standard Model WZ, all processes are added together and split by lepton channel. This combination and splitting is a compromise between fitting each background separately and having a limited lever arm in the high mass region

[1]The p-value is the probability to observe a test statistic at least as unlikely as what was observed, based on a background only hypothesis

and combining all lepton flavor channels together and having a distribution that is not well described by a simple function. The resulting distribution in each channel is fit above $m_{WZ} > 300$ GeV to the sum of two exponential functions,

$$N(x) = c_1 e^{k_1 x} + c_2 e^{k_2 x}. \tag{8.3}$$

Because the high m_{WZ} region is above the characteristic energy scale of physics in the associated processes and above the scale of any detector turn on effects, smooth behavior of the m_{WZ} distribution is expected. The resulting fit is normalized to the number of expected background events in the fit region. Because of statistical fluctuations in the samples used, the samples are rebinned before performing the fit, so that a single event with large weight does not appear as an anomalous point over a background from different samples. While this has an insignificant effect on the fit result, it provides a more easily understood distribution of the points that the fit uses as input. The background distributions and fit function for the non-WZ backgrounds are shown in Figure 8.14. The uncertainties in this fit are also shown. The difference in the shape of the high mass tail between events with the W decaying to an electron and events with the W decaying to a muon is the result of the differing behavior for fake electrons and fake muons coming from the data-driven background estimation, described in Section 8.1.

The background from Standard Model WZ events is also fit and extrapolated. Because of the larger number of such events that pass the event selection cuts, the Monte Carlo itself can be used for a larger part of the distribution. The Standard Model WZ background is fit to a single exponential function above $m_{WZ} > 500$ GeV,

$$N(x) = c_1 e^{k_1 x}. \tag{8.4}$$

A single exponential can be used for this fit because a single homogeneous sample is being modeled. Again, the fit is broken up by lepton flavor channels. Separate fits of the reducible and irreducible backgrounds are used because of the different kinematic behavior of the two samples. The Standard Model WZ distribution, and the resulting fit and uncertainty are showing in Figure 8.15.

In general, the tail of any single sample is well modeled by a single exponential. The sum of irreducible backgrounds, coming from non-WZ processes, is thus fit to a sum of exponentials, rather than single exponential, to account for the fact that different regions are dominated by different samples. Other fit functions are also considered, but the difference in result is negligible compared to the uncertainty associated with the exponential fits. The uncertainty associated with these fits can be very large, O(500%,) for very high m_{WZ}. This fit uncertainty is propagated through the analysis and is the dominant uncertainty for very high mass signals.

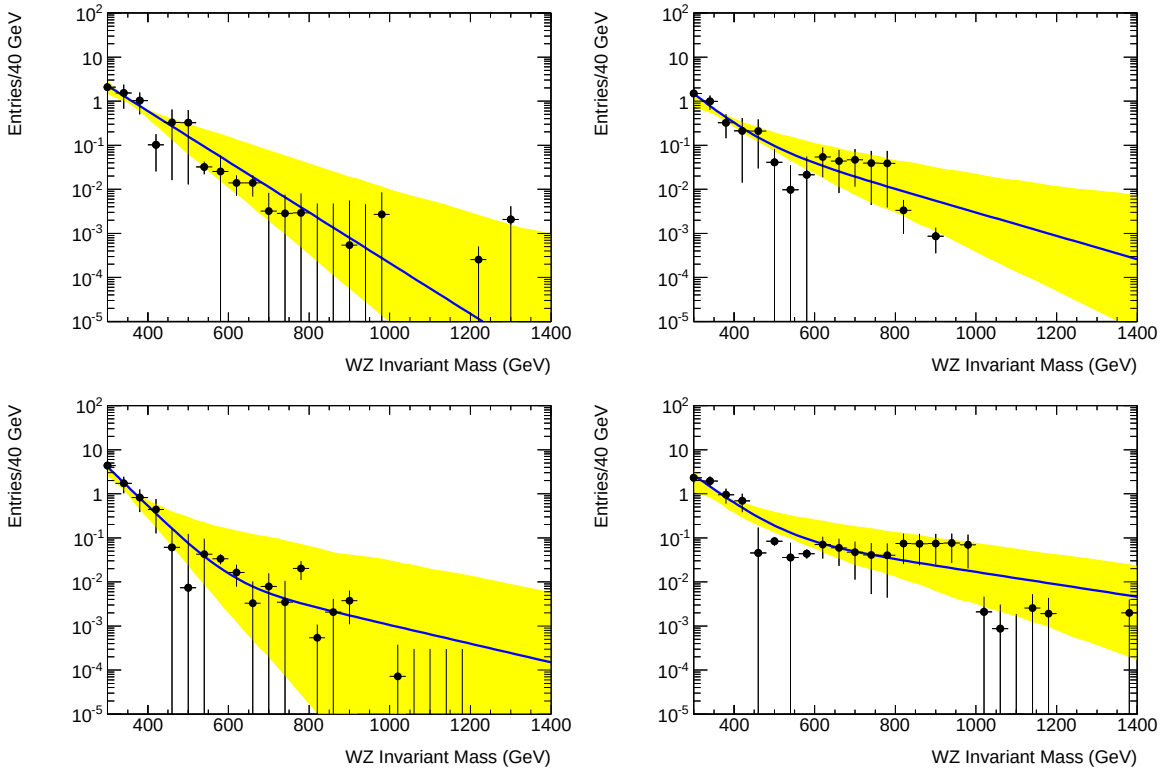

Figure 8.14: Distribution of reducible backgrounds from each lepton channel together with double exponential fit to that channel. The histogram and fitted distribution are normalized to the same number of events. The shaded area indicates the uncertainty in the fitted distribution. The individual plots are for the $e\nu ee$ (top left,) $\mu\nu ee$ (top right,) $e\nu\mu\mu$ (bottom left,) and $\mu\nu\mu\mu$ (bottom right) channels.

8.4 Signal Interpolation

Because the fully simulated W' signal points are broadly spaced, a new physics signal could fall in between two points and would not be well described by either of them. To avoid this issue, the W' signal distributions in the m_{WZ} variable are fit to a characteristic function, and the parameters of that function are interpolated between mass points. This interpolation is then used to model W' signal points between the fully simulated mass points: one interpolated signal every 50 GeV. Because this 50 GeV spacing is smaller than the characteristic width of the $W' \to WZ$ mass peak, limit setting can be performed without concern that a potential signal will fall in between the interpolated mass points.

For this interpolation, each of the fully simulated W' signal samples is fit to a Crystal

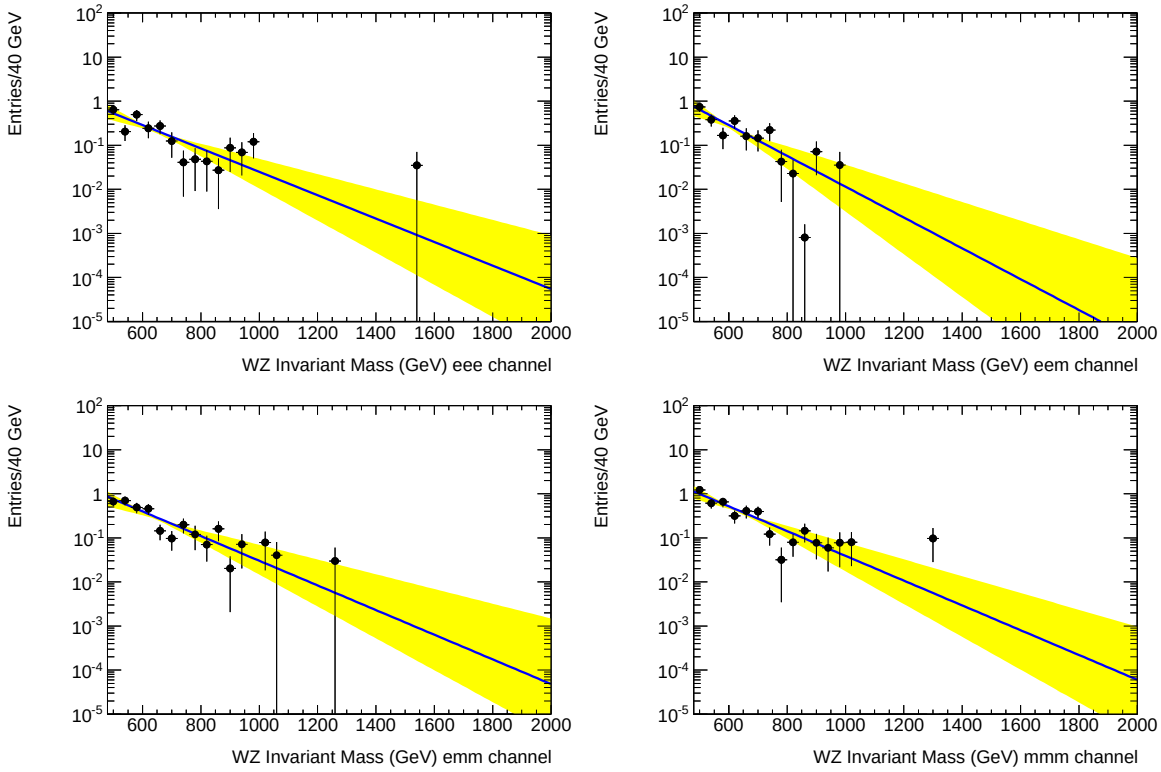

Figure 8.15: Distribution of Standard Model WZ background from each lepton channel together with exponential fit to that channel. The shaded area indicates the uncertainty in the fitted distribution. The individual plots are for the $e\nu ee$ (top left,) $\mu\nu ee$ (top right,) $e\nu\mu\mu$ (bottom left,) and $\mu\nu\mu\mu$ (bottom right) channels.

Ball function, which consists of a Gaussian core with a power law tail:

$$CB(x;m,\sigma,a,n) = N \cdot \begin{cases} \exp(-\frac{(x-m)^2}{2\sigma^2},) & \text{for } \frac{x-m}{\sigma} > -a \\ A \cdot (B - \frac{x-m}{\sigma})^{-n}, & \text{for } \frac{x-m}{\sigma} \leqslant -a \end{cases}, \tag{8.5}$$

$$A = \left(\frac{n}{|a|}\right)^n \cdot \exp\left(-\frac{|a|^2}{2}\right) \tag{8.6}$$

$$B = \frac{n}{|a|} - |a|\,. \tag{8.7}$$

The fit parameters: m, the most probably value of the distribution; σ, the width of the Gaussian; a, the crossover point between the Gaussian and power law regions; and n, the exponent in the power law section of the distribution are extracted from these fits. The distribution of m_{WZ} from the fully simulated events and the fit functions is shown in Figure 8.16.

With the fits performed for all of the simulated points, the Crystal Ball parameters are interpolated using polynomials of various degrees: A degree 3 polynomial for the distribution

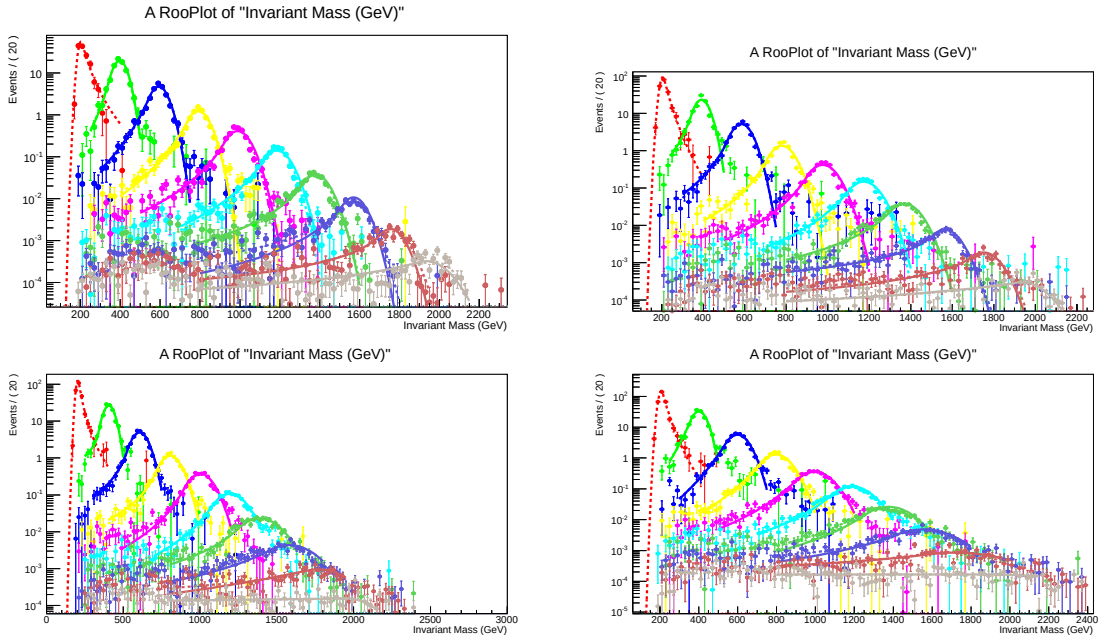

Figure 8.16: Comparison of the crystal ball function fit (dotted lines) to the simulated W' samples with masses 200, 400, 600, 800, 1000, 1200, 1400, 1600, 1800, and 2000 GeV for $e\nu ee$ (top left,) $\mu\nu ee$ (top right,) $e\nu\mu\mu$ (bottom left,) and $\mu\nu\mu\mu$ (bottom right). Also shown are the interpolated signal shapes obtained from the parameter fits (full lines).

of m, a degree 5 polynomial for the distributions of n and σ, a degree 6 polynomial for the distribution of a. The parameters obtained from fitting each signal point to a Crystal Ball and the fit function used to interpolate between those points is shown for the $e\nu ee$ channel in Figure 8.17. Given the interpolation between these parameters, new m_{WZ} distributions can be generated for any W' mass point. Such points are generated every 50 GeV. The shapes of the resulting distributions are shown for the $e\nu ee$ channel in Figure 8.18. In this distribution it is clear that the interpolated signal points have significant overlap with each other, and thus any potential data within this range will be reasonably explained by at least one of these distributions. To accurately match the statistical uncertainty of the fully simulated samples, each fit template is used to generate 30,000 simulated points that are used in the final distribution. Where systematic uncertainties are propagated to the signal samples, this fit and interpolation procedure is redone with the varied distributions to obtain interpolated signals that are consistent with the varied fully simulated signals.

To ensure that this interpolation is stable against the removal of a particular point, a closure test is performed. The 1000 GeV fully simulated mass point is removed and the interpolation procedure is repeated. The interpolated parameters are used to generate an interpolated mass point at 1000 GeV. The interpolated distribution of m_{WZ} shows good agreement with the distribution of m_{WZ} from the fully simulated events. The agreement in

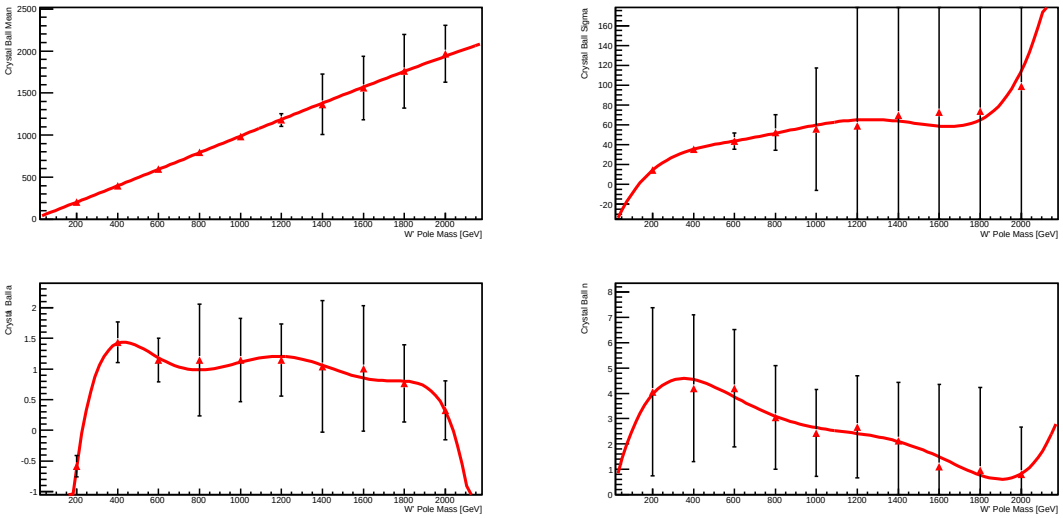

Figure 8.17: Left: Parameter fits of the Crystal Ball function, itself fitted to the fully-simulated W' samples with masses 200, 400, 600, 800, 1000, 1200, 1400, 1600, 1800, and 2000 GeV.

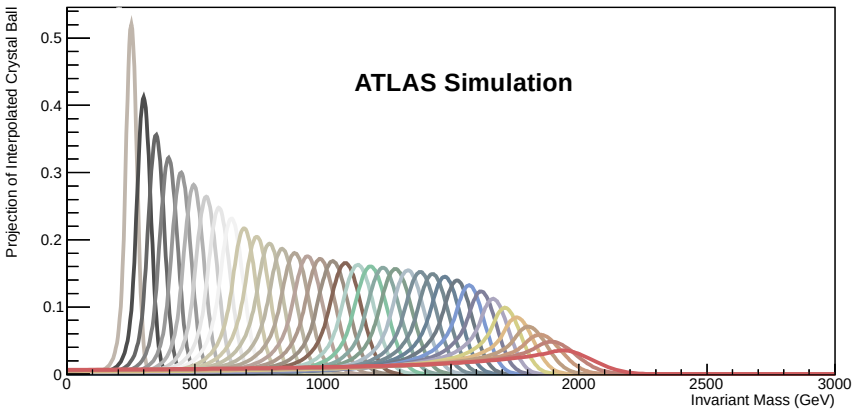

Figure 8.18: Templates of W' signal with masses between 200 and 2000 GeV in steps of 50 GeV, obtained from interpolating the parameters of a Crystal Ball function fit to the fully simulated points.

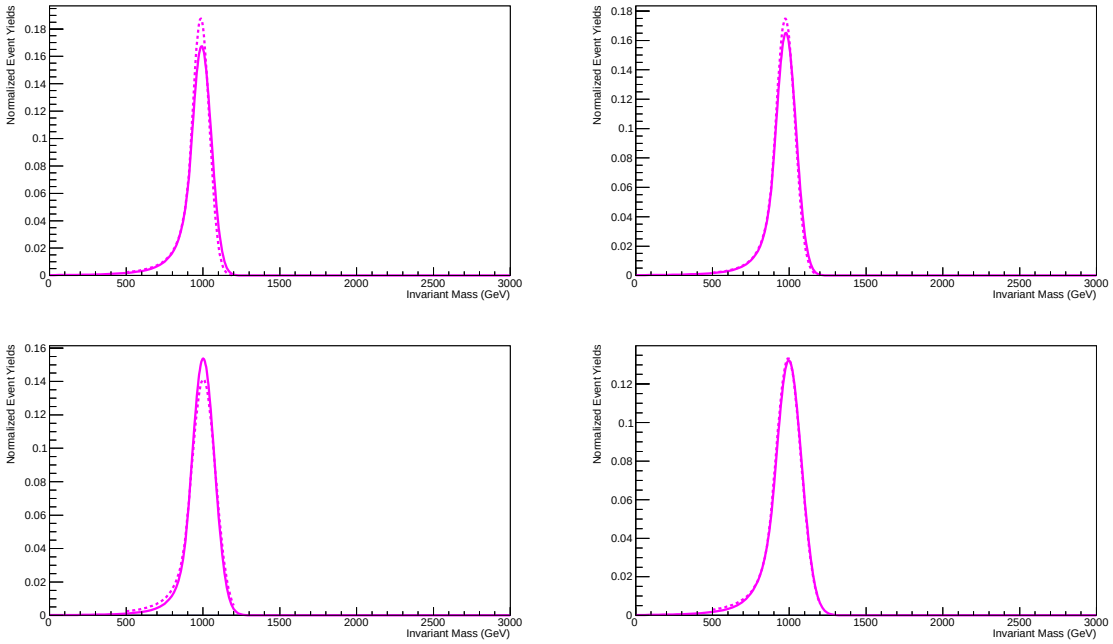

Figure 8.19: Comparison of the crystal ball function fit (dotted lines) to the interpolated W' shape (full line). The $e\nu ee$ (top left,) $\mu\nu ee$ (top right,) $e\nu\mu\mu$ (bottom left,) and $\mu\nu\mu\mu$ (bottom right) channels are individually shown.

each lepton channel is shown in Figure 8.19

Finally, the acceptance, the fraction of events that pass the signal selection cuts, for each interpolated mass point is derived using a spline fit to the acceptance for the fully simulated points. A polynomial fit is not done here because the fully simulated points are used, where they are available, for the limit setting. Such use would cause a discontinuity in the acceptance and thus in the resulting limits when going from a fully simulated to an interpolated point. The distribution of the acceptance, per lepton flavor channel, is shown in Figure 8.20. A full list of the signal acceptance, per lepton flavor channel, and cross sections are in Table 8.4.

The degraded acceptance for very high mass signal points is a result of the relatively large lepton isolation cones used in the event selection, detailed in Sections 7.4.1 and 7.5.1. At very high mass, the Z boson in the event is highly boosted and its decay products will be more collimated. As a result, at high signal mass, the Z decay leptons will increasingly fall inside each others isolation cones. These electrons and muons will then fail the isolation requirements.

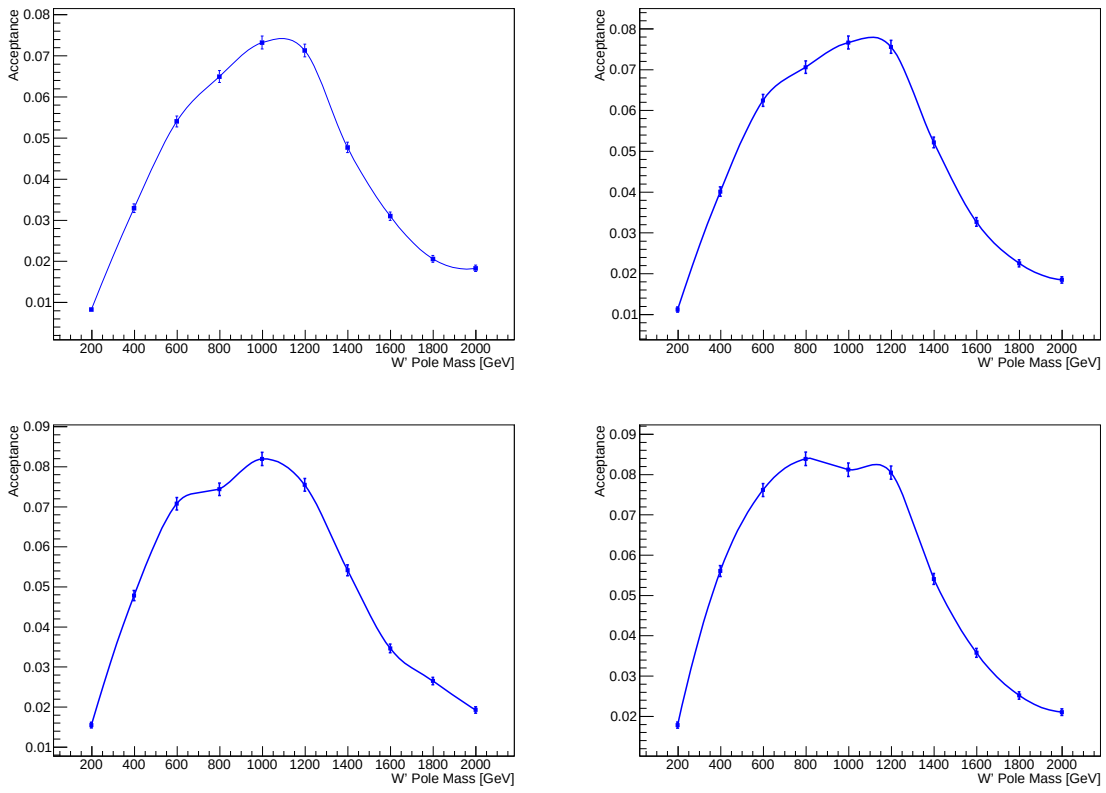

Figure 8.20: Spline fits to the acceptances in the $e\nu ee$ (to left,) $\mu\nu ee$ (top right,) $e\nu\mu\mu$ (bottom left,) and $\mu\nu\mu\mu$ (bottom right) channels using the simulated W' samples (also in blue).

Table 8.4: Summary of cross-sections times branching ratio and acceptances per channel used to derive cross section limits at intermediate $M_{W'}$ mass values, where fully simulated samples are not available.

W' Mass	$\sigma \times B$	Acceptance × Efficiency *per* channel				
$[GeV]$	[pb]	$e\nu ee$	$e\nu\mu\mu$	$\mu\nu ee$	$\mu\nu\mu\mu$	Average
200	1.099	0.033	0.045	0.061	0.071	0.053
250	0.9353	0.056	0.073	0.093	0.118	0.085
300	0.5294	0.081	0.102	0.126	0.159	0.117
350	0.2959	0.106	0.131	0.159	0.194	0.148
400	0.1746	0.131	0.160	0.191	0.224	0.177
450	0.1074	0.156	0.187	0.220	0.250	0.203
500	6.939e-02	0.178	0.211	0.247	0.271	0.227
550	4.644e-02	0.199	0.233	0.268	0.289	0.247
600	3.243e-02	0.216	0.250	0.283	0.305	0.264
650	2.269e-02	0.230	0.262	0.290	0.317	0.275
700	1.641e-02	0.241	0.270	0.293	0.326	0.283
750	1.212e-02	0.251	0.276	0.294	0.333	0.289
800	9.281e-03	0.259	0.282	0.297	0.335	0.293
850	6.940e-03	0.269	0.288	0.304	0.333	0.299
900	5.352e-03	0.278	0.294	0.313	0.330	0.304
950	4.154e-03	0.286	0.300	0.322	0.326	0.309
1000	3.293e-03	0.293	0.306	0.328	0.325	0.313
1050	2.582e-03	0.298	0.311	0.328	0.327	0.316
1100	2.057e-03	0.299	0.314	0.324	0.330	0.317
1150	1.646e-03	0.296	0.311	0.315	0.330	0.313
1200	1.349e-03	0.285	0.302	0.301	0.321	0.302
1250	1.076e-03	0.266	0.284	0.284	0.302	0.284
1300	8.773e-04	0.242	0.261	0.262	0.275	0.260
1350	7.197e-04	0.216	0.234	0.240	0.245	0.234
1400	5.996e-04	0.191	0.208	0.217	0.216	0.208
1450	4.859e-04	0.170	0.185	0.194	0.192	0.185
1500	4.019e-04	0.152	0.164	0.173	0.171	0.165
1550	3.335e-04	0.137	0.146	0.154	0.156	0.148
1600	2.795e-04	0.123	0.130	0.138	0.142	0.133

Chapter 9

Systematic Uncertainties

A number of sources of systematic uncertainty may affect the response of this analysis to a potential signal and the expected distribution of the backgrounds. These systematic uncertainties originate from limited precision in the measured performance of the associated physics objects and uncertainties in the expected behavior of the backgrounds. The dominant uncertainty in the background prediction comes from the uncertainty in the cross section for Standard Model WZ production, although other physics-object uncertainties are not negligible. The dominant systematic uncertainty in the high-mass tail comes from the extrapolation procedure and can produce errors O(1) or larger. Systematic uncertainties that affect the shape of the $m(WZ)$ distribution, used to set limits, are propagated through the analysis with the shape dependence of their effect intact. A full list of the systematic uncertainties in this analysis and their effects on a representative signal and background distribution are in Tables 9.2 and 9.1, respectively.

Systematic uncertainties are treated as entirely correlated across channels; e.g., the electron energy scale uncertainty changes the normalization and shape of the $m(WZ)$ distribution coherently and affects the $e\nu ee$, $e\nu\mu\mu$, $\mu\nu ee$, and $\mu\nu\mu\mu$ channels simultaneously. In this case, the effect on the $\mu\nu\mu\mu$ channel is 0 by construction. Different systematic uncertainties are assumed to be uncorrelated with each other. The may be a very optimistic assumption. The systematic uncertainty for missing transverse energy, which is built from other detector objects, is clearly correlated with the systematic uncertainty for those detector objects. When a systematic uncertainty related to a detector object is varied, that variation is propagated through to the missing transverse energy; e.g., the electron energy scale systematic uncertainty includes the effect of the electron energy scale on the missing transverse energy calculation in addition to its direct effect on electrons.

Table 9.1: Systematic uncertainty for the SM WZ process.

	$e\nu ee$ Channel	$\mu\nu ee$ Channel	$e\nu\mu\mu$ Channel	$\mu\nu\mu\mu$ Channel
Statistics	3.1%	2.7%	2.3%	2.0%
Luminosity	3.6%	3.6%	3.6%	3.6%
Electron trigger	0.01%	0.02%	0.06%	0.00%
Muon trigger	0.00%	0.01%	0.03%	0.19%
Electron ID	2.91%	1.88%	1.03%	0.00%
Electron reconstruction	1.99%	1.33%	0.66%	0.00%
Electron energy resolution	0.80%	0.56%	0.37%	0.00%
Electron energy scale	0.84%	0.92%	0.26%	0.00%
Electron isolation	1.88%	1.25%	0.63%	0.00%
Muon ID	0.00%	0.31%	0.62%	0.93%
Muon isolation	0.00%	0.30%	0.60%	0.90%
Muon momentum resolution MS	0.00%	0.06%	0.14%	0.10%
Muon momentum resolution ID	0.00%	0.11%	0.04%	0.15%
Muon momentum scale	0.00%	0.00%	0.07%	0.23%
Jet energy scale	1.51%	2.20%	1.32%	1.19%
Jet energy resolution	0.14%	0.30%	0.43%	0.08%
METResoSoft	0.59%	0.46%	0.89%	0.19%
METScaleSoft	1.20%	0.80%	1.33%	1.25%
Total (with statistical uncertainty)	6.63%	5.85%	5.06%	4.66%

9.1 Detector Systematics

9.1.1 Luminosity

An accurate measurement of the total luminosity depends on the luminosity calibrations performed during beam separation scans, similar to those documented in [9]. Uncertainty in the luminosity determination can arise from jitter in the beam during scans, a degradation of the beam size during a scan, uncertainties in handling multiple interactions, and uncertainties in the ability to measure the lengths using the Inner Detector. Additionally, the long term stability of this calibration is limited, and these calibrations can only be performed several times a year. The luminosity uncertainty for these data taken during the 2012 run is 3.6%. A more complete discussion of the luminosity determination is in Section 3.3

9.1.2 Trigger

The performance of the electron and muon trigger algorithms is discussed more fully in Sections 5.5 and 5.4. The performance of the associated triggers is evaluated using $Z \to \ell\ell$ tag-and-probe studies. Corrections between Monte Carlo and measured performance are

Table 9.2: Systematic uncertainty for W' signal process with $M(W') = 800$ GeV.

	$e\nu ee$ Channel	$\mu\nu ee$ Channel	$e\nu\mu\mu$ Channel	$\mu\nu\mu\mu$ Channel
Statistics	2.9%	2.7%	2.6%	2.5%
Luminosity	3.6%	3.6%	3.6%	3.6%
Electron trigger	0.00%	0.01%	0.08%	0.00%
Muon trigger	0.00%	0.00%	0.01%	0.23%
Electron ID	2.35%	1.53%	0.82%	0.00%
Electron reconstruction	2.01%	1.34%	0.67%	0.00%
Electron energy resolution	0.43%	0.20%	0.39%	0.00%
Electron energy scale	0.22%	0.24%	0.25%	0.00%
Electron isolation	1.84%	1.23%	0.61%	0.00%
Muon ID	0.00%	0.37%	0.76%	1.14%
Muon isolation	0.00%	0.30%	0.60%	0.90%
Muon momentum resolution MS	0.00%	0.04%	0.04%	0.09%
Muon momentum resolution ID	0.00%	0.00%	0.03%	0.11%
Muon momentum scale	0.00%	0.00%	0.10%	0.04%
Jet energy scale	0.27%	0.37%	0.05%	0.47%
Jet energy resolution	0.74%	0.40%	0.06%	0.45%
METResoSoft	0.39%	0.33%	0.20%	0.24%
METScaleSoft	0.67%	0.16%	0.47%	0.02%
PDF	1%	1%	1%	1%
Total (with statistical uncertainty)	6.06%	5.26%	4.85%	4.78%

considered as functions of η and p_T. Variations of the resulting correction factor are applied for each lepton and propagated through the full analysis. The resulting effect on signal and background acceptance is found to be $< 1\%$ in all channels, with the most significant trigger effects being associated with the $\mu\nu\mu\mu$ channel.

9.2 Object Systematics

9.2.1 Electrons

Electron energy scale and resolution corrections are derived from $Z \to ee$ events [10] and used to correct electron performance. Uncertainties associated with these corrections are also derived from these data in bins of p_T and η, and are propagated through the analysis for both increased and decreased energy scale and resolution. Uncertainty in the electron energy is a result of uncertainty of the material model in the Inner Detector, variation in the fit model used to measure the energy scale, and variation in the energy correction of the pre-sampler. Energy scale and resolution tend to have a larger effect on the final distribution

shape than the sample acceptance. These shape dependent effects are taken into account during the limit-setting procedure, described in Section 10.2. Variation in the electron energy resolution has an effect up to 1% on the signal acceptance and background normalization, depending on the lepton-flavor channel. Variation of the electron energy scale has an effect up to 1% on the signal acceptance and background normalization, depending on lepton-flavor channel.

Additionally, Z tag-and-probe studies are used to evaluate the electron isolation efficiency, identification efficiency, and reconstruction efficiency, described fully in [10]. These studies provide scale factors for the electron efficiency and uncertainties for those scale factors. Uncertainty in the electron efficiencies are a result of subtracting uncertain backgrounds, uncertain background composition, and limited selection efficiency for signal events. The resulting uncertainties, binned by p_T, η, and for reconstruction efficiency, electron quality, are propagated through the analysis. The effect of these variations on the final $m(WZ)$ distribution is considered, although this procedure does not change the kinematics of any individual event. Electron efficiency effects are responsible for significant uncertainties in the relevant lepton-flavor channels. Individually, variations in the isolation efficiency, identification efficiency, and reconstruction efficiency can be $2-3\%$ depending on the lepton-flavor channel.

9.2.2 Muons

Muon momentum scale and resolution corrections are derived from $Z \to \mu\mu$ events [86] and are used to correct muon performance. Uncertainties associated with these corrections are also derived from these data in bins of p_T and η. Uncertainty in muon momenta is the result of uncertainty in the ID material and uncertainty in the muon system alignment. Muon momentum resolution uncertainties are derived separately for the ID and the muon system, and are varied independently. The effects muon momentum uncertainties on the $m(WZ)$ shape are propagated through the analysis. The effect of muon momentum scale and resolution variation on the signal acceptance and background normalization is $< 1\%$ in all lepton-flavor channels for each effect.

Z tag-and-probe studies are also used to evaluate the muon identification and isolation efficiency, described fully in [11]. These studies provide scale factors that are applied to the muon identification and isolation efficiency. Uncertainties in these scale factors, binned by the lepton kinematics, are propagated through the analysis. Muon efficiency uncertainty is measured by varying in the tag definitions and probe definitions used for this study [87]. Uncertainty in the muon identification and isolation efficiency each give an O(1%) variation in the signal acceptance and background normalization. While the variation of these scale factors does not change the kinematics of any individual event, only the weight of that event, differential changes in these weights can affect the shape of the final $m(WZ)$ distribution, and this shape-dependent effect is also considered.

9.2.3 Missing Transverse Energy

Because the missing transverse energy is built out of other physics objects in an event, as described in Section 5.7, uncertainty in each of these objects must be passed into the missing transverse energy calculation. Any uncertainty associated with leptons simultaneously changes the missing transverse energy and the lepton performance, and thus properly correlates effects on leptons and missing transverse energy. Significant contributions to the uncertainty in the missing transverse energy performance also come from uncertainty in the performance of jets and unclustered calorimeter energy.

Although jets are not directly used in this analysis, the use of jets as objects in the reconstruction of missing transverse energy makes this analysis sensitive to the performance of reconstructed jets. Jet performance studies [88] examine the reconstructed energy of jets recoiling from photons and reconstructed Z bosons to ensure accurate reconstruction of the jet energy. Calibrated jets at these energies can then be balanced against higher energy jets to ensure a proper energy scale in that regime as well. Uncertainty in the measurement of this energy scale comes from differences between the in situ calibration and test-beam data, variation in the quark/gluon fraction in jets, variation in the flavor composition of jets, and the dependence of nearby event topology on the calorimeter response. Variation in the jet energy scale and resolution, propagated through the missing energy calculation, have an effect $\sim 2\%$ of on the background normalization and an effect of $\sim 1\%$ on the signal acceptance. The smaller effect on signal acceptance is likely due to the larger neutrino momentum in those events.

Similarly, the accurate measurement of unclustered calorimeter energy is necessary for an accurate measurement of the missing transverse energy in an event. This performance is measured $Z \to \mu\mu$ events, looking at the recoil of the calorimeter energy against the hard objects in the event. This calibration is considered both for events with and without jets [89]. The dominant uncertainty in the measurement of this soft energy response is the difference between data and Monte Carlo. The effects of pileup in an event primarily add extra soft, unclustered energy. Pileup effects are considered when varying the response of missing transverse energy to the soft calorimeter energy term. Variation in the soft calorimeter terms, propagated through the missing transverse energy calculation, have an effect of $\sim 1\%$ on both signal acceptance and background normalization.

9.3 Theory Systematics

9.3.1 Cross Section

For backgrounds that are estimated entirely from Monte Carlo, the measured uncertainty in the cross section is propagated through to the generated events. Measurements of the WZ, ZZ, and $Z\gamma$ cross sections have been performed using the ATLAS detector [90] [91] [92]. In generating these events, differences between the MCFM and MC@NLO generators were considered, along with a variation of the PDF, between CT10 and MSTW2008. Additionally,

the effects of varying the PDF parameters within their known uncertainties, varying the renormalization and factorization scales within a factor of two either direction, and varying the value of α_S within its known uncertainty are considered. The resulting uncertainties in the Monte Carlo cross sections are listed in Table 9.3

Table 9.3: Systematic uncertainty for W' signal process with $M(W') = 800$ GeV

Process	σ	$\frac{\delta\sigma}{\sigma}$
WZ	18.5 pb	7%
ZZ	5.96 pb	5%
$Z\gamma$	14.7 pb	8%

9.3.2 Parton Distribution Functions

The variation of signal acceptance is considered as a function of the parton distribution function parameters used in the Monte Carlo generation. The signal samples are generated with PYTHIA [74] using the MSTW2008 [2] PDF. The central value of these PDFs are accompanied by 40 other PDFs that are obtained by the varying the 20 independent fit parameters by $\pm 1\sigma$. The effect of PDF variation on the signal acceptance is estimated as:

$$\Delta A = \frac{1}{2}\sqrt{\sum_{i=1}^{n}(A_i^+ - A_i^-)^2}, \tag{9.1}$$

where A_i^+ is the acceptance when parameter i is varied upward and A_i^- is the acceptance when parameter i is varied downward.

In the same manner, the CT10 PDF [79] is used to calculated the signal acceptance and variation on that acceptance within the CT10 PDF set. The two PDFs give different signal acceptances. Similarly the variation parameters within each PDF affects the signal acceptance. These two effects on signal acceptance are added in quadrature. The breakdown of the internal and total variation of signal acceptance as a result of PDF uncertainty is listed for a single W' mass point at 1000 GeV in Table 9.4. The effect of systematic uncertainty in the PDFs is summarized in Table 9.5 for W' samples and in Table 9.6 for ρ_T samples.

9.3.3 Standard Model WZ Shape Uncertainty

Proper modeling of the high mass tail of the $m(WZ)$ distribution is particularly important for understanding backgrounds in this analysis. While Section 9.3.1 describes uncertainty in the integrated WZ cross section, variation in event kinematics, specifically in the $m(WZ)$ distribution, are considered here. The $m(WZ)$ distribution from the POWHEG generator is compared to the same distribution using events from the SHERPA and MADGRAPH [93]

Table 9.4: Summary of the fractional uncertainties in the PDF on the fiducial acceptance for a $M(W') = 1000$ GeV sample, computed using PDF re-weighting with respect to MSTW2008 and CT10 set

PDF Set	$e\nu ee$ [%]	$\mu\nu ee$ [%]	$e\nu\mu\mu$ [%]	$\mu\nu\mu\mu$ [%]	Inclusive [%]
Nominal Acceptance	0.081	0.085	0.091	0.090	0.347
MSTW2008lo68cl Int Var	0.002	0.002	0.001	< 0.001	< 0.001
MSTW2008lo68cl Tot Var	0.002	0.002	0.001	< 0.001	< 0.001
CT10 Acceptance	0.081	0.085	0.091	0.090	0.347
CT10 Int Var	0.006	0.004	0.006	0.002	0.002
CT10 Tot Var	0.006	0.005	0.007	0.002	0.003
Total Uncertainty	0.006	0.005	0.007	0.002	0.003

Table 9.5: Summary of the fractional uncertainties on the fiducial acceptance for all the W' samples

Sample	$e\nu ee$ [%]	$\mu\nu ee$ [%]	$e\nu\mu\mu$ [%]	$\mu\nu\mu\mu$ [%]	Inclusive [%]
$m(W') = 200$ GeV	1.9	2.7	1.9	2.8	2.3
$m(W') = 400$ GeV	0.9	0.7	0.7	0.5	0.6
$m(W') = 600$ GeV	0.9	0.8	0.3	0.3	0.4
$m(W') = 800$ GeV	0.6	0.9	0.6	0.4	0.4
$m(W') = 1000$ GeV	0.6	0.5	0.7	0.2	0.3
$m(W') = 1200$ GeV	1.2	0.4	0.4	0.9	0.3
$m(W') = 1400$ GeV	0.9	0.5	0.3	0.6	0.2
$m(W') = 1600$ GeV	0.9	1.3	2.7	3.5	2.0
$m(W') = 1800$ GeV	3.8	3.8	5.3	4.6	4.3
$m(W') = 2000$ GeV	6.9	8.0	7.3	8.8	7.8

generators. Because only differences between the generator kinematics are of interest, these samples are not run through the full ATLAS detector simulation and object reconstruction, and are instead considered after generation by these programs. These distributions are normalized to the nominal POWHEG event yield. In the high mass tails, where shape uncertainties are a large concern, the limited number of Monte Carlo events make it difficult to disentangle generator differences from statistical fluctuations. Even for the most conservative binning considered, no statistically significant difference is seen between POWHEG and the other two generators. The distribution of events given such a binning is shown in Figure 9.1. Thus, no additional systematic uncertainty is assigned to the shape of the $m(WZ)$ distribution.

Table 9.6: Summary of the fractional uncertainties on the fiducial acceptance for all the ρ_T samples

Sample	$e\nu ee$ [%]	$\mu\nu ee$ [%]	$e\nu\mu\mu$ [%]	$\mu\nu\mu\mu$ [%]	Inclusive [%]
ρ_T $m = 250$ GeV	0.04	0.205	0.454	0.675	0.822
ρ_T $m = 300$ GeV	0.04	0.205	0.455	0.676	0.823
ρ_T $m = 350$ GeV	0.042	0.21	0.46	0.679	0.825
ρ_T $m = 400$ GeV	0.044	0.215	0.466	0.684	0.828
ρ_T $m = 450$ GeV	0.046	0.22	0.471	0.688	0.83
ρ_T $m = 500$ GeV	0.048	0.226	0.478	0.693	0.834
ρ_T $m = 550$ GeV	0.051	0.232	0.484	0.698	0.837
ρ_T $m = 600$ GeV	0.053	0.237	0.49	0.702	0.839
ρ_T $m = 650$ GeV	0.056	0.244	0.497	0.707	0.843
ρ_T $m = 700$ GeV	0.059	0.251	0.504	0.713	0.846
ρ_T $m = 750$ GeV	0.062	0.256	0.51	0.717	0.849
ρ_T $m = 800$ GeV	0.065	0.263	0.517	0.722	0.852
ρ_T $m = 850$ GeV	0.068	0.269	0.523	0.726	0.855
ρ_T $m = 900$ GeV	0.071	0.276	0.53	0.731	0.858
ρ_T $m = 950$ GeV	0.074	0.283	0.537	0.737	0.861
ρ_T $m = 1000$ GeV	0.078	0.29	0.544	0.741	0.864

9.4 Analysis Systematics

9.4.1 Fake Lepton Backgrounds

Because a data-driven technique is used to derive the contribution of backgrounds containing fake leptons, the previous discussion of detector uncertainties, object uncertainties, and theory uncertainties does not apply. A full discussion of the uncertainties associated with the fake lepton backgrounds is in Section 8.1. As a reminder, the fake lepton background comes with an uncertainty of ∼25% for events with a fake muon and ∼40% for events with a fake electron. This uncertainty covers the contribution of events with multiple fake leptons. The dominant uncertainty in the measurement of the fake electron background is the uncertain size of the subtracted prompt leptons when measuring the fake factor. The dominant uncertainties in the measurement of the fake muon background are the limited number of data events in the sample where the fake factor is measured and uncertainty in the correction needed to extrapolate from high d_0 events to low d_0 events.

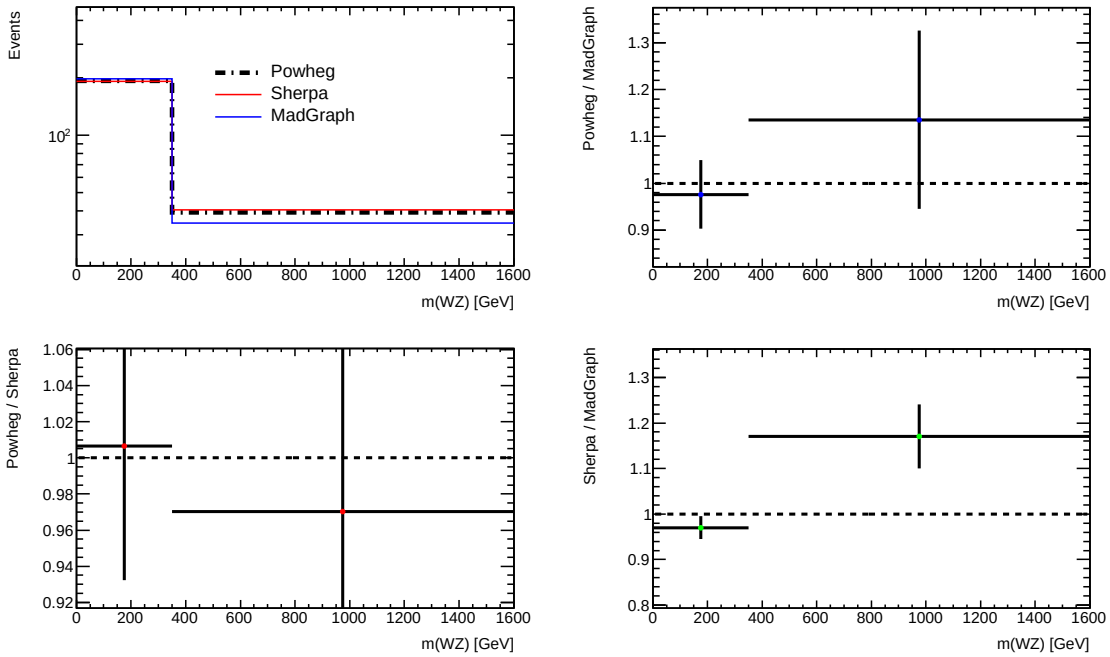

Figure 9.1: Shape comparison between POWHEG, SHERPA, and MADGRAPH with bin boundaries at 0, 300, and 1600 GeV. Uncertainties shown are one sigma statistical uncertainties.

9.4.2 Background Extrapolation

The extrapolation of Standard Model backgrounds into the high $m(WZ)$ region, described in Section 8.3, comes with a significant uncertainty in the fit used to perform that extrapolation. This fit was performed with the ROOFIT [94] package, and the resulting uncertainty comes from the fit uncertainty obtained using that package. In particular, the errors on the background extrapolation were obtained by a sampling method where the fit parameters were varied within $\pm 1\sigma$ as defined by the fit covariance matrix. The error band is the interval that contains 68% of the resulting curves.

Uncertainty in the extrapolation fit has a small effect on the total number of events in the Standard Model background, $\sim$1%. In the distribution tails, the uncertainty in this extrapolation is, however, very large. At 800 GeV, the extrapolation uncertainty is 50%. At 1200 GeV, the extrapolation uncertainty is 200%. While other systematic uncertainties are applied in this regime, the uncertainty in the extrapolation fit is strongly dominant.

Chapter 10

Results

With the WZ control region well understood, the analysis signal region can be considered. As described in Chapter 7, the signal region is defined by events with three good leptons, high missing energy, a reconstructed W and Z boson, and angular cuts that require the W and Z bosons to be back-to-back. Specifically,

- 3 good electrons or muons in the event with $p_T > 25$ GeV and no fourth lepton with $p_T > 20$ GeV
- A missing transverse energy, $E_T^{miss} > 25$ GeV
- A Z boson reconstructed from two same flavor, opposite sign leptons with $|m_{\ell\ell} - m_Z| < 20$ GeV
- A W boson reconstructed from the remaining lepton and the missing energy with $m_{T,W} < 100$ GeV
- A back-to-back signature of the reconstructed bosons, with $\Delta y(W, Z) < 1.8$ and $\Delta\phi(W, Z) > 2.6$.

After these cuts, a total of 325 events are observed with an expected Standard Model background of $294.8 \pm 4.5(stat) \pm 24.7(syst)$. No significant excess in the total event counts is observed. Since, even in this signal region, the vast majority of events are expected to come from Standard Model WZ processes, no excess in the integrated event counts is expected. The dominant uncertainty in the event counts comes from the theoretical uncertainty in calculating the Standard Model cross sections. The systematic uncertainties in the backgrounds from fake leptons is also significant. The breakdown of these events by background and expected contribution of various signals is seen in Table 10.1. The statistical uncertainty across all of the channels is considered to be uncorrelated and is added in quadrature. Systematics uncertainties from the same source are applied coherently across all lepton-flavor channels. Systematics uncertainties from different sources are optimistically assumed to be uncorrelated and are added in quadrature. The dominant systematic uncertainties are associated

with the Standard Model cross sections, the fake factor measurement, and the extrapolation of background to high $m(WZ)$. Contributions from events with more than one fake lepton and from events with a fake lepton that forms a good reconstructed Z are small and covered by the systematic uncertainty for the $\ell\ell + jets$ background. The photon in the $Z\gamma$ background has a vanishing chance of resulting in a fake muon, and so the contribution of this process to channels with a muon associated with the W boson decay is negligible. The breakdown of data in the signal cutflow is seen in Table 10.2. The acceptance times efficiency for these cuts on a representative signal point at $m(W') = 800$ GeV are found in Table 10.3. The low acceptance times efficiency for the three lepton cut folds in the inefficiencies for all of the leptons to pass the good lepton selection, including both the lepton quality cuts and the isolation requirements in addition to the event quality requirements described in Section 7.

Table 10.1: The estimated background yields, the observed number of data events, and the predicted signal yield after applying the signal selection cuts

Sample	$e\nu ee$ Channel	$\mu\nu ee$ Channel	$e\nu\mu\mu$ Channel	$\mu\nu\mu\mu$ Channel	inclusive
Backgrounds:					
WZ	$39.1 \pm 1.2 \pm 4.0$	$52.0 \pm 1.4 \pm 5.2$	$60.2 \pm 1.4 \pm 5.8$	$81.5 \pm 1.6 \pm 7.7$	$232.8 \pm 2.8 \pm 22.4$
ZZ	$3.7 \pm 0.1 \pm 0.3$	$3.3 \pm 0.1 \pm 0.2$	$3.6 \pm 0.1 \pm 0.3$	$4.4 \pm 0.1 \pm 0.3$	$15.0 \pm 0.2 \pm 0.9$
$Z\gamma$	$2.4 \pm 1.0 \pm 0.9$	0	$6.0 \pm 1.8 \pm 0.8$	0	$8.4 \pm 2.1 \pm 1.2$
$\ell\ell + jets$	$5.4 \pm 1.2 \pm 2.4$	$8.0 \pm 1.2 \pm 2.2$	$15.2 \pm 2.1 \pm 6.8$	$10.0 \pm 1.3 \pm 2.8$	$38.6 \pm 2.9 \pm 10.4$
Sum of Backgrounds	$50.56 \pm 2.0 \pm 4.7$	$63.3 \pm 1.8 \pm 6.2$	$85.0 \pm 3.1 \pm 9.0$	$95.9 \pm 2.1 \pm 8.2$	$294.8 \pm 4.5 \pm 24.7$
Data	55	73	98	98	324
Signals:					
$W' \to WZ$ ($M(W') = 600$ GeV)	22.8 ± 0.7	26.3 ± 0.8	29.8 ± 0.8	32.1 ± 0.8	111.0 ± 1.6
$W' \to WZ$ ($M(W') = 800$ GeV)	7.8 ± 0.2	8.5 ± 0.2	9.0 ± 0.2	10.1 ± 0.2	35.4 ± 0.4
$W' \to WZ$ ($M(W') = 1000$ GeV)	3.1 ± 0.1	3.3 ± 0.1	3.5 ± 0.1	3.5 ± 0.1	13.4 ± 0.2
$\rho_{\mathrm{T}} \to WZ$ ($M(\rho_{\mathrm{T}}) = 400$ GeV)	14.2 ± 0.7	17.8 ± 0.7	22.3 ± 0.8	25.0 ± 0.8	79.3 ± 1.6
$\rho_{\mathrm{T}} \to WZ$ ($M(\rho_{\mathrm{T}}) = 600$ GeV)	4.9 ± 0.2	5.8 ± 0.2	6.7 ± 0.2	7.3 ± 0.2	24.7 ± 0.4
$\rho_{\mathrm{T}} \to WZ$ ($M(\rho_{\mathrm{T}}) = 800$ GeV)	2.0 ± 0.1	1.9 ± 0.1	2.3 ± 0.1	2.6 ± 0.1	8.8 ± 0.2

Table 10.2: Cut flow table in data

Cutflow	$e\nu ee$ Channel	$\mu\nu ee$ Channel	$e\nu\mu\mu$ Channel	$\mu\nu\mu\mu$ Channel
Three leptons and $\lvert M_{\ell\ell} - M_Z \rvert < 20$ GeV	201	257	340	349
E_T^{miss} >25 GeV	123	193	224	246
m_{T}^W <100 GeV	108	167	200	208
$\Delta y(W,Z)$ <1.8	98	140	173	177
$\Delta\phi(W,Z) > 2.6$	55	73	98	98

Table 10.3: Relative acceptance times efficiency for each selection cut, and the total acceptance times efficiency for $M(W') = 800$ GeV

Cutflow	$e\nu ee$ Channel	$\mu\nu ee$ Channel	$e\nu\mu\mu$ Channel	$\mu\nu\mu\mu$ Channel
Three leptons	0.348	0.374	0.400	0.434
$\lvert M_{\ell\ell} - M_Z \rvert < 20$ GeV	0.954	0.946	0.943	0.948
$m_T(W) < 100$ GeV	0.916	0.890	0.928	0.913
tight++ ID $W(e\nu)$	0.942	-	0.943	-
$E_T^{miss} > 25$ GeV	0.980	0.974	0.991	0.983
$\Delta y(WZ)$	0.943	0.943	0.929	0.927
$\Delta\phi(WZ)$	0.977	0.973	0.977	0.978
Total acceptance times efficiency	0.259	0.282	0.297	0.335

Because the $\Delta y(W,Z)$ and $\Delta\phi(W,Z)$ distributions are used to separate the WZ control region from the signal region, the distribution of data in these variables is interesting to consider. Figure 10.1 shows these variables after all other cuts in the analysis are applied. The slight deficit of data in the WZ control region and slight excess of data in the signal region are seen here to arise largely from the $\Delta\phi(W,Z)$ distribution.

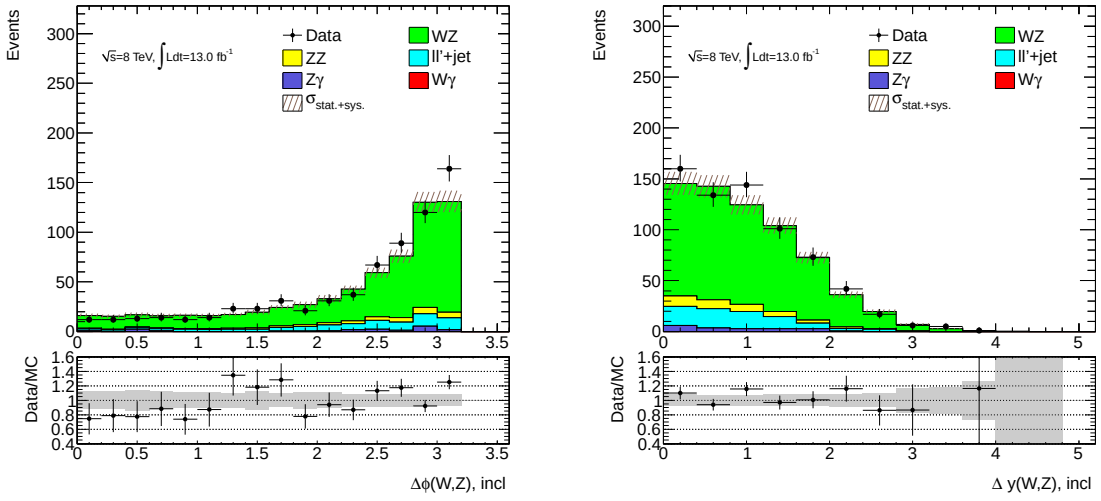

Figure 10.1: Comparison of data with the expected background for the boson angular cuts: $\Delta\phi(W,Z)$ on the left, $\Delta y(W,Z)$ on the right

10.1 Signal Region Kinematics

Although only the $m(WZ)$ distribution is considered for limit setting, other kinematic distributions in the signal region are examined to ensure that the data are well understood. Figure 10.2 shows the reconstructed W and Z boson kinematic distributions in the signal region along with data and several simulated signal points. The Standard Model backgrounds agree well with the observed data. In each lepton-flavor channel, the following distributions are considered: missing transverse energy in Figure 10.3, Z boson p_T in Figure 10.4, and WZ transverse mass in Figure 10.5. The shapes show good consistency between Standard Model backgrounds and the observed data. No particular lepton-flavor channel shows strong features compared to the inclusive data.

The distribution used to set limits based on these data is the distribution of the WZ invariant mass, with the W boson 4-vector reconstructed as described in Section 7.6. The full WZ invariant mass distribution including the background extrapolation described in Section 8.3 is shown in Figure 10.6. This distribution broken down by lepton-flavor channel is shown in Figure 10.7 on a linear scale and in Figure 10.8 on a logarithmic scale.

The sparsely populated tail of these distributions makes it difficult to assess the agreement between data and estimated backgrounds without performing a statistical test. Table 10.4 shows the integrated event counts above a number of $m(WZ)$ cuts, for both data and expected backgrounds, along with the p-value to observe that many events based on a Standard-Model-background-only hypothesis. Statistical and systematic errors are considered by performing a number of pseudo-experiments with the mean of the Poisson distributed background events varied by a random amount in each trial determined by a Gaussian distribution with width equal measured uncertainty. The smallest p-value for the integrated event counts in this test is 0.03, for $m(WZ) > 320$ GeV. Above this cut, 86 events are observed with an expected background of 57.5 ± 5.0. Given the significant overlap of the various cuts here and the use of a more detailed limit-setting approach, no trails factor is computed for these probabilities.

A number of high $m(WZ)$ events are observed. The details of 16 events with $m(WZ) > 500$ GeV are shown in Tables 10.5, 10.6, 10.7, and 10.8. No particular pattern or problematic behavior is observed in these events. A visualization of the detector response in the event with the highest $m(WZ)$ is shown in Figure 10.9.

10.2 Limit Setting

With no significant excess of data observed in the signal region, the distribution of $m(WZ)$ is used to constrain potential new physics decaying to WZ, based on the W' and ρ_T models. These constraints are derived using a semi-frequentist approach to run pseudo-experiments to determine the compatibility of the data with the expected backgrounds and a number of different signal hypotheses. This approach allows the analysis to incorporate all of the information about the $m(WZ)$ shape and all of the shape dependence of systematic uncertainties

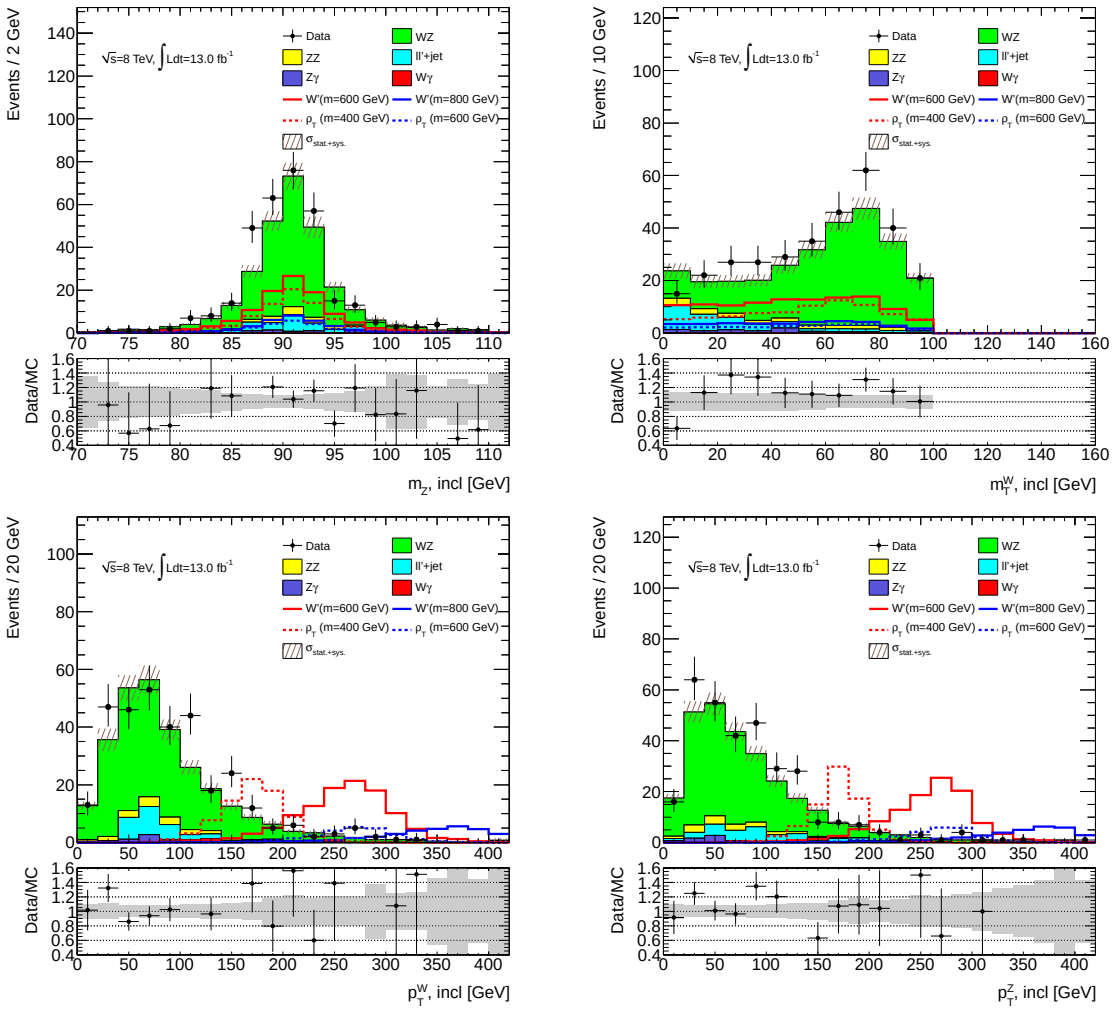

Figure 10.2: Comparison of the data with the background estimation for events with all selection cuts applied: Z candidate mass (top left,) M_T^W (top right,) Z boson p_T (bottom left,) and W boson p_T (bottom right). Predictions from W' samples with masses of 600 and 800 GeV and ρ_{T} samples with masses of 400 and 600 GeV are also shown.

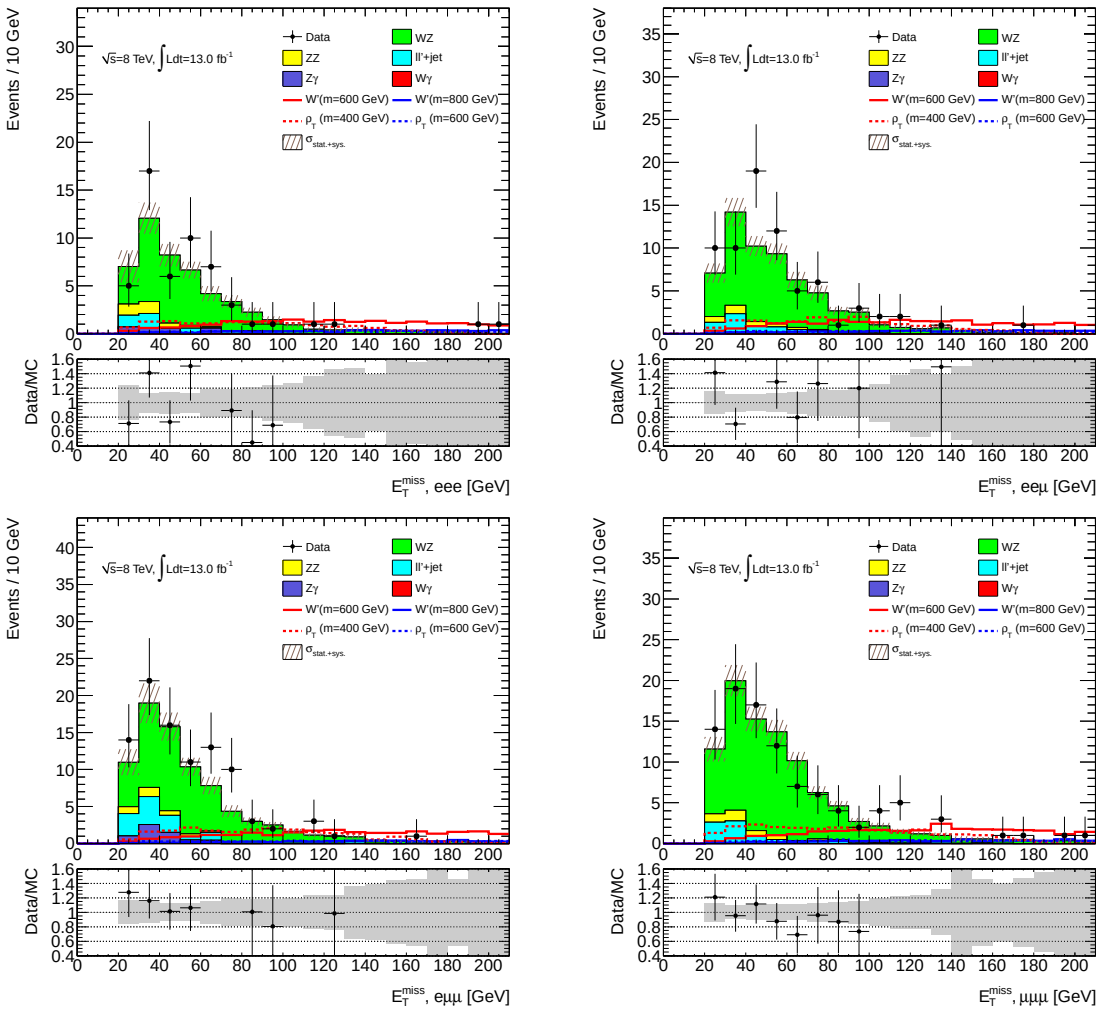

Figure 10.3: Comparison of missing transverse energy between data with expected background for events with all selection cuts applied: $e\nu ee$ channel (top left,) $\mu\nu ee$ channel (top right,) $e\nu\mu\mu$ channel (bottom left,) $\mu\nu\mu\mu$ channel (bottom right,) Predictions from W' samples with masses of 600 and 800 GeV and ρ_{T} samples with masses of 400 and 600 GeV are also shown.

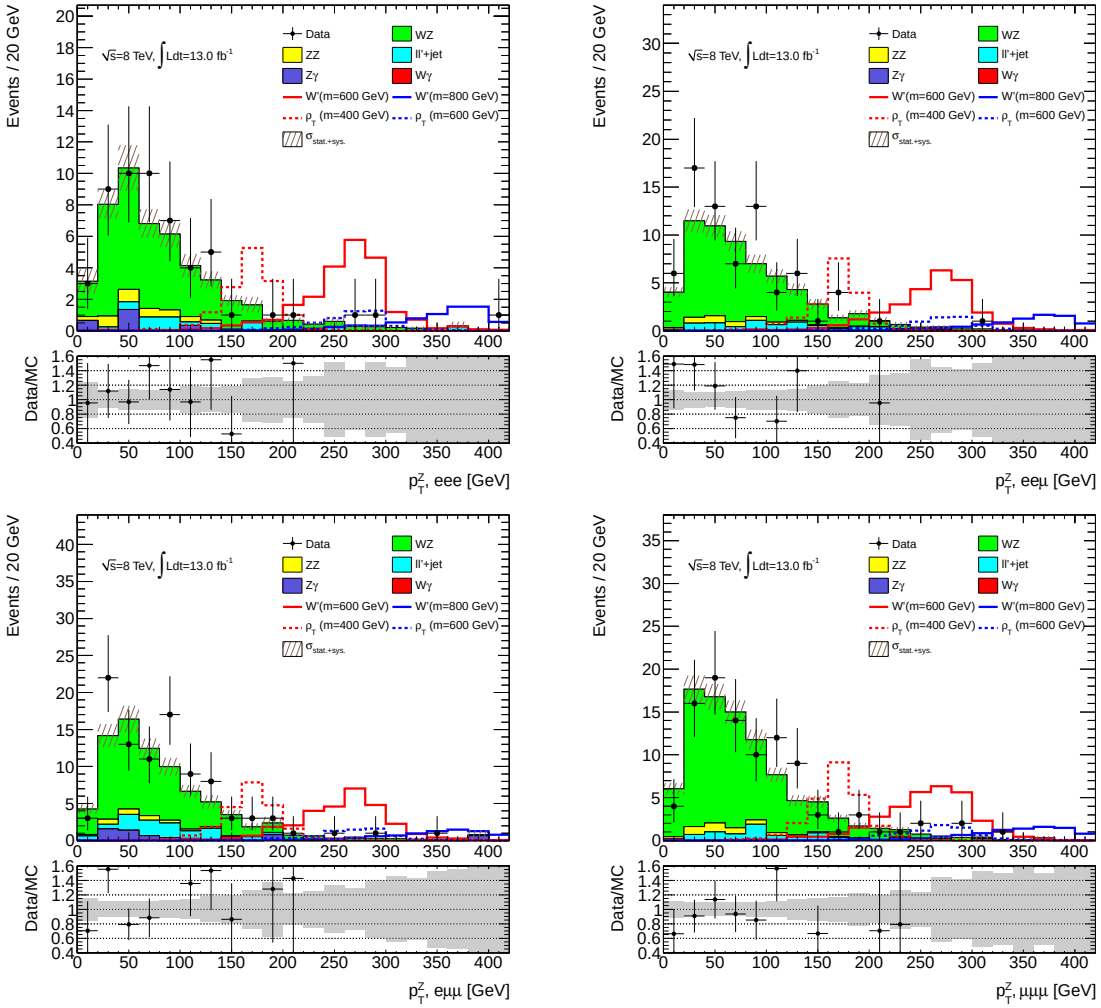

Figure 10.4: Comparison of Z boson transverse momentum between data with expected background for events with all selection cuts applied: $e\nu ee$ channel (top left,) $\mu\nu ee$ channel (top right,) $e\nu\mu\mu$ channel (bottom left,) $\mu\nu\mu\mu$ channel (bottom right). Predictions from W' samples with masses of 600 and 800 GeV and ρ_{T} samples with masses of 400 and 600 GeV are also shown.

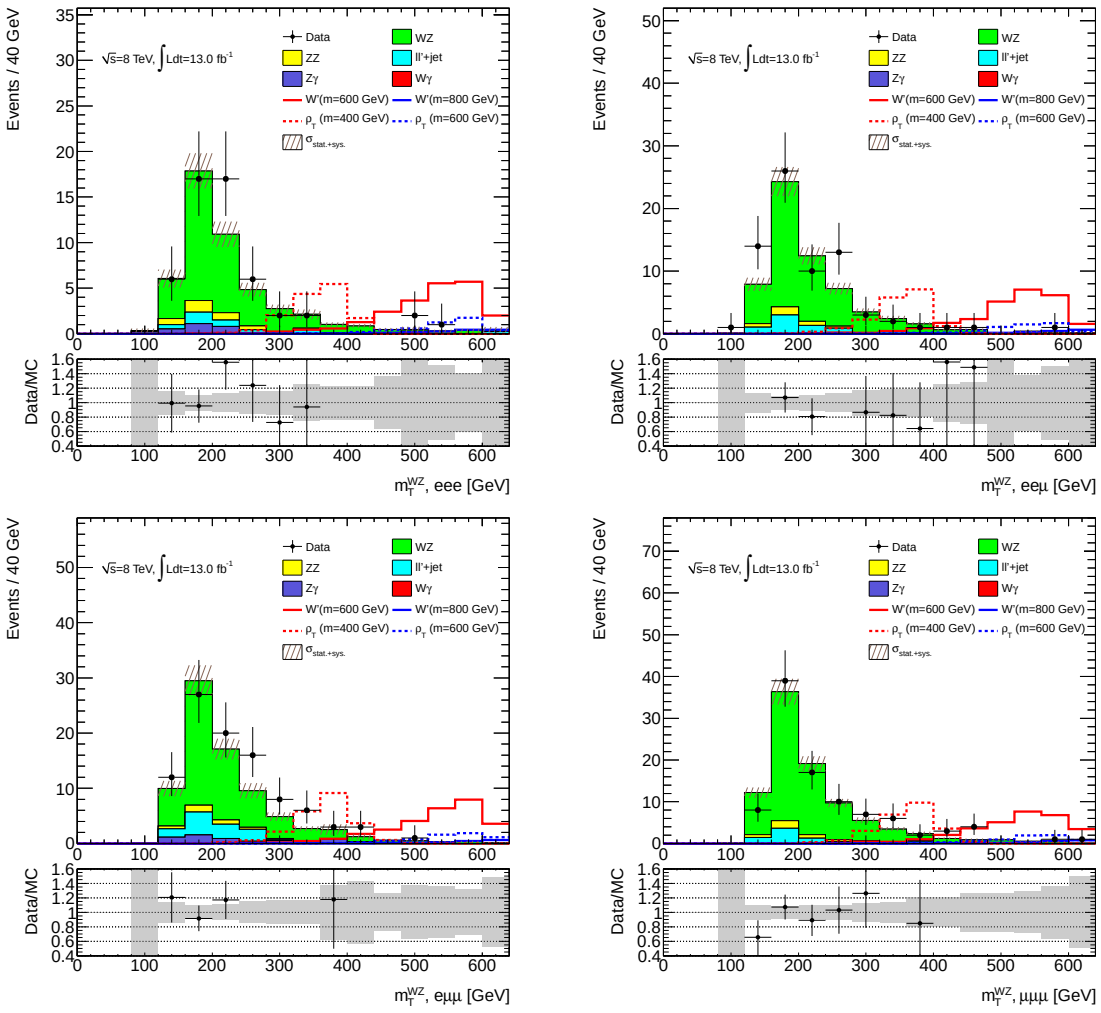

Figure 10.5: Comparison of WZ transverse mass between data with expected background for events with all selection cuts applied: $e\nu ee$ channel (top left,) $\mu\nu ee$ channel (top right,) $e\nu\mu\mu$ channel (bottom left,) $\mu\nu\mu\mu$ channel (bottom right,) Predictions from W' samples with masses of 600 and 800 GeV and ρ_{T} samples with masses of 400 and 600 GeV are also shown.

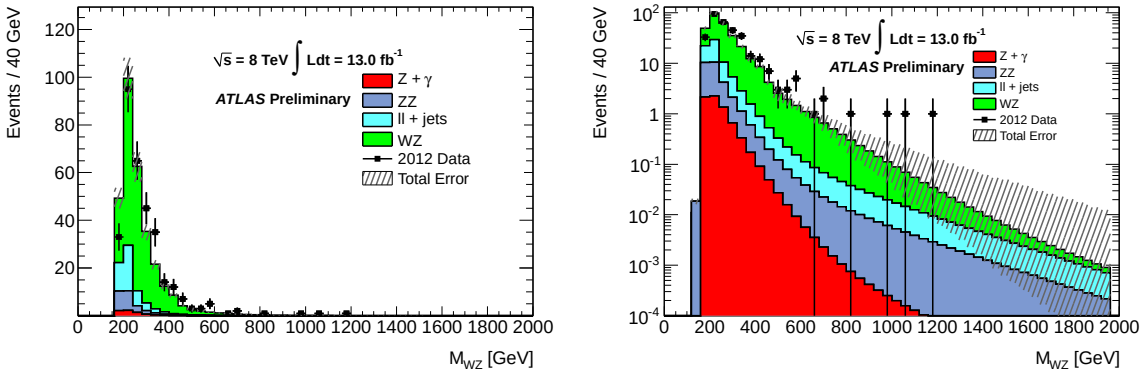

Figure 10.6: Comparison of the data with the background estimation for events with all selection cuts applied and extrapolated backgrounds included: WZ bosons invariant mass with linear (left) and log scale (right).

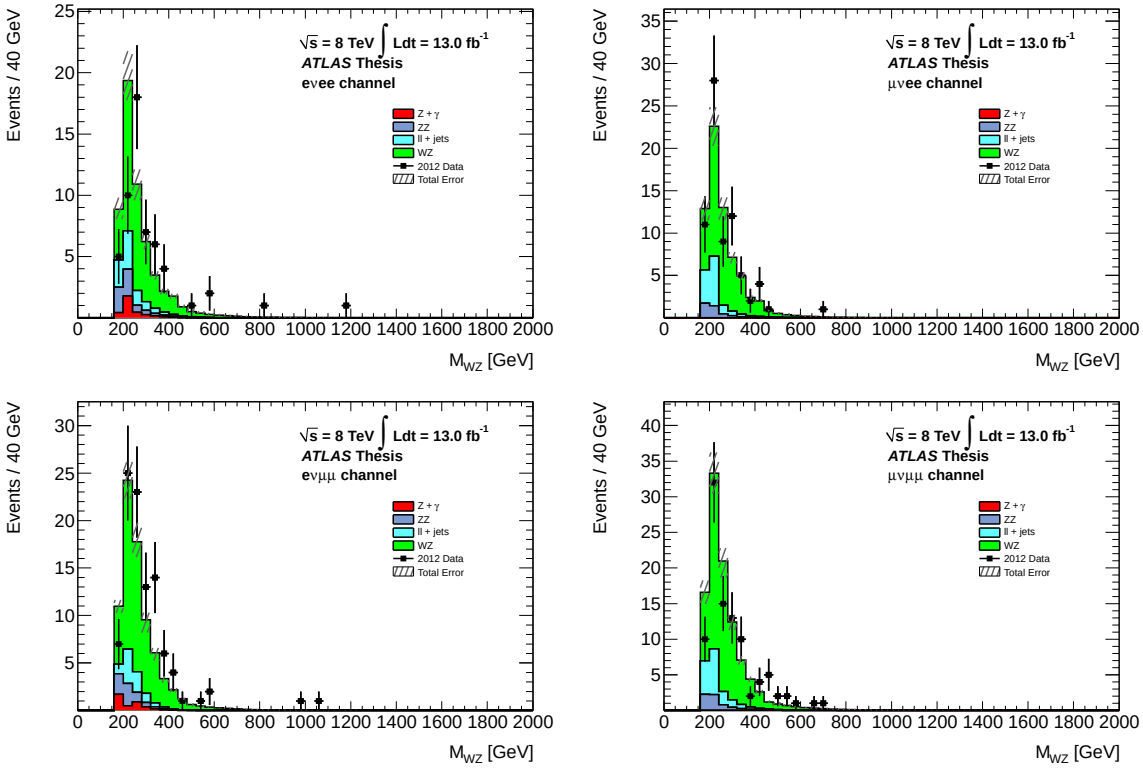

Figure 10.7: Comparison of the data with the background estimation for events with all selection cuts applied and extrapolated backgrounds included: WZ bosons invariant mass in the: $e\nu ee$ channel (top left,) $\mu\nu ee$ channel (top right,) $e\nu\mu\mu$ channel (bottom left,) $\mu\nu\mu\mu$ channel (bottom right).

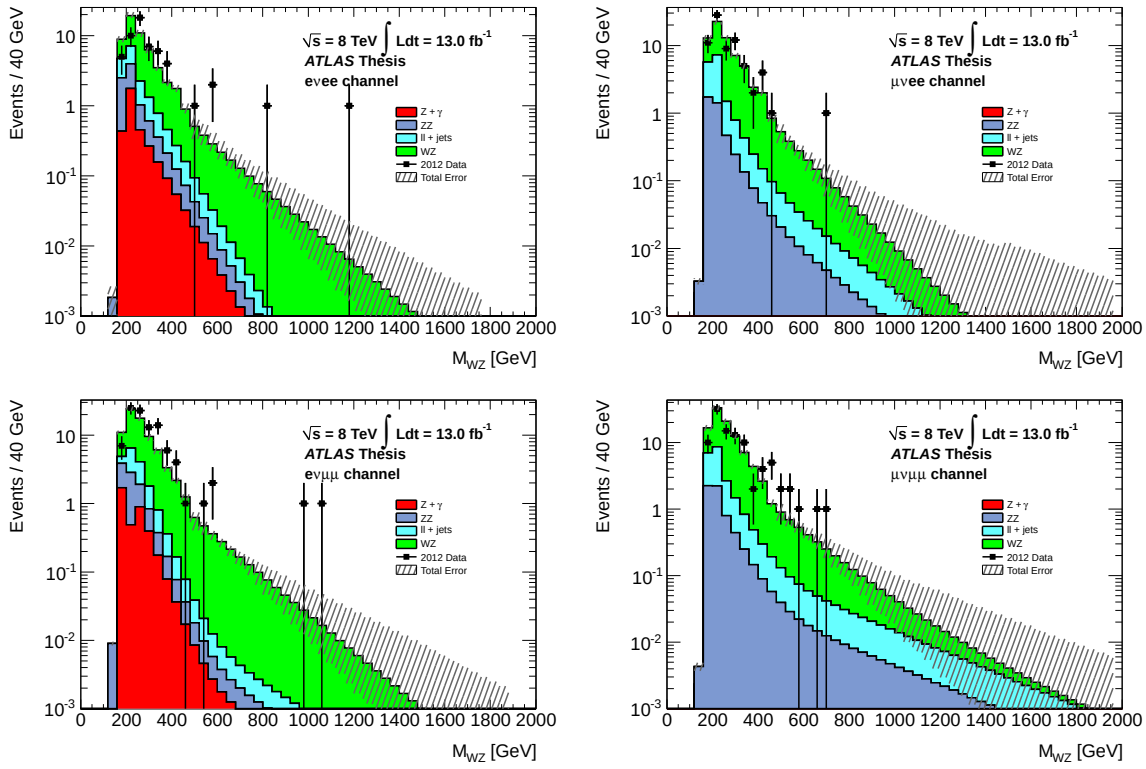

Figure 10.8: Comparison of the data with the background estimation for events with all selection cuts applied and extrapolated backgrounds included: WZ bosons invariant mass in the: $e\nu ee$ channel (top left,) $\mu\nu ee$ channel (top right,) $e\nu\mu\mu$ channel (bottom left,) $\mu\nu\mu\mu$ channel (bottom right).

in this distribution. The use of interpolated signal points, described in Section 8.4, ensures that any excess in the data will be reasonably described by some signal distribution.

10.2.1 Limit Setting Procedure

The basis for the limit-setting procedure used here is the likelihood ratio for observing some new physics signal over a given background [95], as defined in Equation 10.1. Here, $\mathbf{x}$ is the number of events observed, b is the number of expected background events, and s is the number of expected signal events. The likelihood function $\mathcal{L}$ is for the Poisson probability distribution:

$$\Lambda(\mathbf{x}) = \frac{\mathcal{L}(s+b|\mathbf{x})}{\mathcal{L}(b|\mathbf{x})}. \tag{10.1}$$

More explicitly, the fully expanded likelihood ratio test statistic is:

	$e\nu ee$			$\mu\nu ee$			$e\nu\mu\mu$			$\mu\nu\mu\mu$			inclusive		
Region	Exp.	Obs.	p-value	Exp.	Obs.	p-value	Exp.	Obs.	p-value	Exp.	Obs.	p-value	Exp.	Obs.	p-value
m(WZ)> 320 GeV	10.4 ± 2.1	15	0.20	12.1 ± 2.2	13	0.53	15.6 ± 2.3	30	0.01	19.4 ± 3.2	28	0.08	57.5 ± 5.0	86	0.03
m(WZ)> 360 GeV	7.0 ± 1.6	9	0.39	7.2 ± 1.6	8	0.55	9.5 ± 1.7	16	0.08	12.3 ± 2.5	18	0.14	35.9 ± 3.8	51	0.03
m(WZ)> 400 GeV	4.8 ± 1.3	5	0.66	4.8 ± 1.3	6	0.50	6.1 ± 1.3	10	0.19	7.9 ± 2.0	16	0.03	23.6 ± 3.0	37	0.03
m(WZ)> 440 GeV	3.0 ± 1.0	5	0.36	2.8 ± 1.0	2	0.28	3.9 ± 1.0	6	0.36	5.3 ± 1.6	12	0.03	15.1 ± 2.4	25	0.04
m(WZ)> 480 GeV	2.1 ± 0.8	5	0.19	2.0 ± 0.8	1	0.19	2.7 ± 0.8	5	0.29	4.1 ± 1.4	7	0.24	10.9 ± 2.0	18	0.08
m(WZ)> 520 GeV	1.6 ± 0.7	4	0.24	1.4 ± 0.7	1	0.30	2.1 ± 0.7	5	0.17	3.2 ± 1.2	5	0.39	8.3 ± 1.7	15	0.07
m(WZ)> 560 GeV	1.3 ± 0.6	4	0.15	1.0 ± 0.6	1	0.41	1.6 ± 0.7	4	0.22	2.5 ± 1.1	3	0.69	6.4 ± 1.6	12	0.09
m(WZ)> 600 GeV	1.0 ± 0.5	2	0.57	0.8 ± 0.6	1	0.48	1.2 ± 0.6	2	0.67	2.0 ± 1.0	2	0.84	4.9 ± 1.4	7	0.37
m(WZ)> 640 GeV	0.7 ± 0.5	2	0.48	0.6 ± 0.5	1	0.37	0.9 ± 0.6	2	0.57	1.6 ± 0.9	2	0.77	3.8 ± 1.3	7	0.22
m(WZ)> 680 GeV	0.6 ± 0.4	2	0.40	0.4 ± 0.5	1	0.29	0.7 ± 0.6	2	0.48	1.2 ± 0.8	1	0.31	3.0 ± 1.2	6	0.21
m(WZ)> 720 GeV	0.4 ± 0.4	2	0.32	0.3 ± 0.5	0	0.74	0.6 ± 0.6	2	0.40	1.0 ± 0.8	0	0.37	2.3 ± 1.1	4	0.39
m(WZ)> 760 GeV	0.3 ± 0.3	2	0.26	0.2 ± 0.4	0	0.80	0.4 ± 0.5	2	0.32	0.8 ± 0.7	0	0.45	1.8 ± 1.0	4	0.28
m(WZ)> 800 GeV	0.3 ± 0.3	2	0.21	0.2 ± 0.4	0	0.85	0.3 ± 0.5	2	0.26	0.6 ± 0.6	0	0.53	1.4 ± 0.9	4	0.19
m(WZ)> 840 GeV	0.2 ± 0.3	1	0.17	0.1 ± 0.3	0	0.89	0.3 ± 0.5	2	0.21	0.5 ± 0.6	0	0.60	1.1 ± 0.9	3	0.29
m(WZ)> 880 GeV	0.2 ± 0.3	1	0.13	0.1 ± 0.3	0	0.92	0.2 ± 0.4	2	0.16	0.4 ± 0.5	0	0.66	0.9 ± 0.8	3	0.22
m(WZ)> 920 GeV	0.1 ± 0.2	1	0.10	0.1 ± 0.3	0	0.94	0.2 ± 0.4	2	0.13	0.3 ± 0.5	0	0.71	0.7 ± 0.7	3	0.16
m(WZ)> 960 GeV	0.1 ± 0.2	1	0.08	0.0 ± 0.2	0	0.95	0.1 ± 0.3	2	0.10	0.3 ± 0.4	0	0.76	0.5 ± 0.6	3	0.13
m(WZ)> 1000 GeV	0.1 ± 0.2	1	0.06	0.0 ± 0.2	0	0.97	0.1 ± 0.3	1	0.08	0.2 ± 0.4	0	0.80	0.4 ± 0.5	2	0.28

Table 10.4: The observed and expected numbers of events in different $m(WZ)$ regions after all selection cuts. The p-value to observed this number of events given a background only hypothesis is also shown. The extrapolated background distribution has been used in this calculation. The error on the expected number of events is the combined statistical and systematic uncertainty.

Table 10.5: Details of the 5 events with $m(WZ) > 500$ GeV in the $e\nu ee$ channel

$m(WZ)$	E_T^{miss}	ℓ flavor	ℓ p_T	ℓ η	ℓ ϕ	j p_T	Z p_T	$m(Z)$	W p_T	$m_T(W)$
518.8	111.2	e	197.6	-1.353	-2.347	128.1	294.2	101.1	202.8	82.23
		e	107.6	-1.074	1.366					
		e	97.78	-0.6633	-2.535					
576.9	87.59	e	224.4	-1.116	1.845		276.5	89.91	260.3	75.76
		e	183.5	-0.8404	-1.37					
		e	61.23	-1.577	2.465					
1184	201.5	e	257.8	1.356	-2.49	57.29	405.6	91.77	454.6	65.33
		e	249.6	-0.2005	0.8695					
		e	157.5	-0.6258	0.6944					
593.2	34.19	e	264.9	-0.5082	-1.263	31.36	211.6	93.42	284.2	92.98
		e	174.8	-1.689	1.923					
		e	43.01	-0.8185	2.527					
835	228.5	e	394	-0.3597	0.2761	263.9	567.4	94.31	294.3	30.41
		e	181.2	-0.3846	0.6301	30.33				
		e	67.3	-0.728	-2.4					

$$\Lambda(\mathbf{x}) = \frac{(s+b)^{\mathbf{x}} e^{-(s+b)}}{\mathbf{x}!} / \frac{(b)^{\mathbf{x}} e^{-(b)}}{\mathbf{x}!}. \tag{10.2}$$

Because events in these individual channels represent occurrences that are exceedingly rare compared to the LHC collision rate, the counts in each lepton-flavor channel are essentially uncorrelated. Assuming that the channels are fully independent, this test statistic is easily expanded to consider the counts of $\mathbf{x}$ in each channel. The combined likelihood for the back-

Table 10.6: Details of the single event with $m(WZ) > 500$ GeV in the $\mu\nu ee$ channel

$m(WZ)$	E_T^{miss}	ℓ flavor	$\ell\ p_T$	$\ell\ \eta$	$\ell\ \phi$	j p_T	$Z\ p_T$	$m(Z)$	$W\ p_T$	$m_T(W)$
682.7	229.5	e	257.9	-0.3676	-0.7698		303.3	90.57	271.4	69.63
		e	45.98	-1.162	-0.9345					
		μ	50.68	0.8554	2.844					

Table 10.7: Details of the 5 events with $m(WZ) > 500$ GeV in the $e\nu\mu\mu$ channel

$m(WZ)$	E_T^{miss}	ℓ flavor	$\ell\ p_T$	$\ell\ \eta$	$\ell\ \phi$	j p_T	$Z\ p_T$	$m(Z)$	$W\ p_T$	$m_T(W)$
595.8	95.18	e	118.4	-1.572	1.449		207	89.73	211.9	26.43
		μ	156.9	0.5278	-1.698					
		μ	52.96	-0.3515	-2.081					
976.2	264.7	e	75.52	0.1934	1.672	411.2	616.9	87.04	336.4	51.11
		μ	465.3	-0.8322	-1.868	173.4				
		μ	157.5	-0.7649	-2.184	48.49				
1050	37.09	e	451.3	-0.9526	-2.663		451.7	92.65	486.9	38.46
		μ	280.3	-0.1598	0.4377					
		μ	173.9	0.1999	0.651					
533.2	248.6	e	69.72	-0.5231	-0.4707	128.3	152.4	89.82	307.2	83.57
		μ	110.3	0.1762	2.764	37.78				
		μ	42.68	1.393	2.964	37.78				
571.5	37.46	e	130.4	-2.261	-2.604	418.2	354.8	99.28	166.6	20.57
		μ	249.5	-1.225	0.4869	188.6				
		μ	114.4	-0.8867	0.971	64.88				
						49.95				

Table 10.8: Details of the 5 events with $m(WZ) > 500$ GeV in the $\mu\nu\mu\mu$ channel

$m(WZ)$	E_T^{miss}	ℓ flavor	$\ell\ p_T$	$\ell\ \eta$	$\ell\ \phi$	j p_T	$Z\ p_T$	$m(Z)$	$W\ p_T$	$m_T(W)$
562.6	111.9	μ	226.1	1.135	2.319	88.45	280.1	80.85	141.4	20.3
		μ	61.89	1.512	2.895	61.25				
		μ	30.97	0.6294	-0.07024					
550.8	168	μ	116.3	-1.549	2.943	164.8	182.3	90.45	263.5	64.8
		μ	103.4	-0.2629	0.2459	148.5				
		μ	66.07	-0.5591	2.976	65.71				
						48.24				
						46.88				
706.5	192	μ	192.5	0.1779	2.822	50.01	330.4	90.31	279.1	29.05
		μ	147.8	0.4115	2.335	25.29				
		μ	88.6	1.639	-0.2787					
533.7	130.2	μ	118.9	2.215	-1.866	142.8	118.7	86.9	236.4	78.53
		μ	79.67	0.7832	0.5344	135.2				
		μ	53.6	-0.137	1.499					
663.8	86.37	μ	184.7	0.3312	0.6493		293.1	87.34	267.2	45.11
		μ	165.5	-0.6381	-2.465					
		μ	130.4	-1.16	-2.19					

ground only and signal plus background hypotheses are simply the product of the likelihoods for each individual channel. Similarly, this approach can accommodate data that are divided

into various bins by the product of likelihoods across those bins. This allows the evaluation of the likelihood ratio across analysis channels and with multiple data bins:

$$\Lambda(\mathbf{x}) = \prod_{c}^{channels} \prod_{a}^{bins} \frac{(s_{ca} + b_{ca})^{\mathbf{x}_{ca}} e^{-(s_{ca}+b_{ca})}}{\mathbf{x}_{ca}!} / \frac{(b_{ca})^{\mathbf{x}_{ca}} e^{-(b_{ca})}}{\mathbf{x}_{ca}!}. \tag{10.3}$$

The parallel structure of calculating the likelihood across different bins and different channels is reduced by referring to "bins" in a generic sense to mean the product of both. As final limits will be obtained by maximizing this likelihood, the negative log likelihood ratio (LLR) is computed. The latter is easier to work with mathematically, and the parameter value that maximizes one will maximize both.

$$LLR(\mathbf{x}) = -2\ln(\Lambda(\mathbf{x})) = -2\sum_{m}^{\text{bins}} \left[s_m - \mathbf{x}_m \ln\left(1 + \frac{s_m}{b_m}\right)\right]. \tag{10.4}$$

Taking $\mathbf{x} = \mathbf{D}$, the distribution of events observed in data, the LLR for these data are determined. To quantify how consistent this LLR is with the background only and signal plus background hypotheses, this single LLR is compared to a histogram of LLRs generated by performing pseudo-experiments. A single pseudo-experiment proceeds as follows:

1. For each systematic uncertainty, i, a random number g_i is generated from a normalized Gaussian distribution with a mean of 0 and a width (σ) equal to the size of that systematic uncertainty. Where asymmetric systematic uncertainties occur, a bifurcated Gaussian is used instead. Where the uncertainty is large compared to the size of the nominal value, a Log-Normal distribution is used instead. Where systematic uncertainties vary by bin, m, a single random number is generated from a Gaussian distribution, g_i, and that number is scaled by the size of the systematic uncertainty in each bin, $g_{i,m}$. Thus, shape-dependent systematic uncertainties are applied consistently across all bins.

   If a single systematic uncertainty is not well correlated across channels and bins, its contribution is divided into components that *are* strongly correlated across channels and bins. This method explains why there is a systematic uncertainty associated with the electron identification efficiency, a separate systematic uncertainty associated with electron energy scale, etc., rather than just a systematic uncertainty associated with "electrons." This approach is still imperfect because it offers no hope of including partially-correlated systematic uncertainties. In many cases the limited information available for parameterizing systematic uncertainties makes the pursuit of a full correlation matrix between different systematic uncertainties in different channels and different bins impossible. There are, however, some high-energy physics analyses, e.g., for the measurement of Parton Distribution Functions that *do* have well-explored systematic uncertainties and can use a correlation matrix to address partial correlations [96]. Such analyses are, however, uncommon.

The random sampling of systematic errors is clearly at odds with a strictly frequentist limit-setting approach. This sampling is equivalent to treating the systematic errors as nuisance parameters with a Gaussian (or bifurcated Gaussian or Log-Normal) Bayesian prior probability density functions. When many pseudo-experiments are run, these nuisance parameters are marginalized by an implicit numerical integration. The use of this integration implies that the LLR obtained in a pseudo-experiment is not strictly a ratio of likelihoods. It will, nonetheless, still be called a LLR in the remainder of this discussion.

An optimistic assumption is made in treating the systematic uncertainties as Gaussian. In some cases, this assumption is more reasonable: The systematic uncertainty in the electron fake factor is the result of differences between "good" and "bad" lepton kinematics, differences between signal and control region kinematics, differences between triggered and untriggered events, and differences between measurements using events from different Monte Carlo generators. If these contributions are numerous, small, uncorrelated, and have finite variance, the central limit theorem can be appealed to to justify the use of a Gaussian distribution. In some pathological cases, e.g., if the dominant uncertainty in the $m(WZ)$ distribution was the difference between the results from the only two NLO generators available, there might be only two values to compare to understand a systematic uncertainty. With such limited information, no strong case can be made for any particular distribution. In such a case, assuming a Gaussian distribution is the result only of optimism. A more rigorous treatment of these pathological systematic uncertainties, where they appear, would be beneficial, but is not performed.

2. For each background, j, a distribution of background events is generated. In each bin, m, the expected background is determined by $B_j^m = B_{j,0}^m(1 + \sum_i^N g_{i,m})$. Here, $B_{j,0}^m$ is the nominal expected yield for background j in bin m. $g_{i,m}$ is the random number determined in the previous step, and N is the total number of systematic uncertainties that apply to this background. Then B_j^m is the expected background yield for this background and bin in this pseudo-experiment.

3. In precisely the same way, for some signal, k, a distribution of events is generated. In each bin, m, the expected signal is determined by $S_k^m = S_{k,0}^m(1 + \sum_i^M g_{i,m})$. Here, $S_{k,0}^m$ is the nominal expected yield for signal k in bin m. $g_{i,m}$ is the random number determined in the first step, and M is the total number of systematic uncertainties that apply to this signal. Then S_k^m is the expected signal yield for this signal and bin in this pseudo-experiment.

4. Two "data" yields are then generated for this pseudo-experiment. $\mathbf{D_b}$ is the yield in each bin given only the Standard Model background processes. $\mathbf{D_{s+b}}$ is the yield given some signal process and the Standard Model background processes. For each bin, a random number is sampled from a Poisson distribution with a mean given by the signal

and background distributions for this particular pseudo-experiment: $\sum_j^{N_b} B_j^m$ for $\mathbf{D_b}$ and $\sum_j^{N_b} B_j^m + S_k^m$ for $\mathbf{D_{s+b}}$. The signal and background means vary from pseudo-experiment to pseudo-experiment because of the random sampling of systematic errors.

5. Given the pseudo-experiment event counts for the background only and signal plus background hypothesis, determined above, the LLR is constructed for each, designated as $LLR(\mathbf{D_b})$ for the background only hypothesis and $LLR(\mathbf{D_{s+b}})$ for the background plus some signal hypothesis.

For each signal point, 100,000 pseudo-experiments are performed assuming the signal plus background and background only hypotheses. These pseudo-experiments populate a histogram of $LLR(\mathbf{D_b})$ and $LLR(\mathbf{D_{s+b}})$ for each signal. A p-value, assuming the background only hypothesis or signal plus background hypothesis, is computed by integrating the normalized histogram of $LLR(\mathbf{D_b})$ or $LLR(\mathbf{D_{s+b}})$, respectively, from the value $LLR(\mathbf{D})$ to $+\infty$. The degree to which these histograms are separated is a measure of the ability to distinguish signal from background.

From these p-values, the CL_s [97] is,

$$\mathrm{CL}_s = \frac{p\text{-value, assuming the signal plus background hypothesis}}{1 - p\text{-value, assuming the background only hypothesis}}[1]. \tag{10.5}$$

Here, the p-values are based on the log-likelihood ratio test statistic.

If the histograms of the LLRs given the background only and signal plus background hypotheses are normalized to unity and written as $H(q||b)$ and $H(q||s+b)$ respectively, the CL_s is calculated as

$$\mathrm{CL}_s = \frac{\sum_{q=LLR(\mathbf{D})}^{+\infty} H(q||s+b)}{\sum_{-\infty}^{q=LLR(\mathbf{D})} H(q||b)}. \tag{10.6}$$

This quantity is similar in interpretation to CL_b, except for signal rather than background. A value of CL_s approaching one implies that the data are very well described by the signal hypothesis, and a small value of CL_s implies that no signal is observable in the data.

10.2.2 Limit-Setting Output

This general framework is implemented for the WZ analysis described in the previous chapters. The values for $S_{k,0}^m$, $B_{j,0}^m$, and D are taken from the $m(WZ) \equiv m(3\ell + E_T^{miss})$ histograms in the $e\nu ee$, $e\nu\mu\mu$, $\mu\nu ee$, and $\mu\nu\mu\mu$ channels. 50 bins are used in the histogram range from $[0, 2000]$ GeV with a constant bin size of 40 GeV. The distribution of signal, background, and data events along with the combined uncertainties are shown in Figure 10.7. Systematic uncertainties are applied in a shape-dependent manner, coherently to each bin, channel, and sample that they affect. The effect of a systematic uncertainty on a given bin is taken as the effect of that systematic uncertainty on the nearest 20% of the nominal sample. This

ensures that systematic uncertainties are applied smoothly and that individual bins with limited or null statistics still provide a sensible, coherent response to the fluctuation of each systematic uncertainty. The fractional response curves for two such systematic uncertainties on a ρ_T sample with a 1000 GeV mass is shown in Figure 10.10. The effect of the electron identification efficiency is seen to raise or lower the normalization of the sample. The effect of the electron energy scale is seen to shift the peak to the left or right. For extrapolated backgrounds, described in Section 8.3, this smoothing ensures that systematic uncertainties can be estimated for the samples before extrapolation and that the effect of each systematic uncertainty is well defined even in regions where no events exist in the original samples.

For each mass hypothesis for both W' and ρ_T signals, the CL_s is computed using the method described above. If the resulting value for that signal and mass is ≤ 0.05, the corresponding mass hypothesis is excluded at 95% CL. Similarly, if $\mathrm{CL}_s > 0.05$, no exclusion is possible. For each signal hypothesis, the excluded cross section is determined by adjusting the signal yield until $\mathrm{CL}_s = 0.05$. The amount by that the signal is scaled times the nominal signal cross section gives the cross section for that signal that is excluded at 95% CL, $\sigma^{95\%}$.

10.2.3 Interpretation as W'

Using this procedure, $\sigma^{95\%}$ and all intermediate steps are obtained for all of the W' mass hypotheses in each lepton-flavor channel individually and for the simultaneous fit to all lepton-flavor channels. The resulting p-values are shown in Table 10.9 and represent the probability that the listed backgrounds fluctuate to the observed yield. The smallest observed p-value occurs in the $e\nu\mu\mu$ channel for the 350 GeV mass point with a p-value of 0.00073. With no expectation for new physics to favor one particular lepton-flavor channel, the smallest p-value in the combination of all channels occurs at the 350 GeV mass point with a p-value of 0.0087. Because of the partial overlap in $m(WZ)$ for adjacent mass points, no trials factor is included in these p-values. These results are more unlikely than the integrated p-values for $m(WZ) > 320$ in the $e\nu\mu\mu$ and inclusive channels shown in Table 10.4.

The excluded cross section times branching ratio is shown in Figures 10.11, 10.12, 10.13, 10.14 for the lepton-flavor channels $e\nu ee$, $e\nu\mu\mu$, $\mu\nu ee$, and $\mu\nu\mu\mu$ respectively, and Figure 10.15 for the combined limits. Results are shown with no systematic uncertainties and full systematic uncertainties. The expected exclusion is derived from the median pseudo-experiment response with no signal present. Background fluctuations by $\pm 1\sigma$ and $\pm 2\sigma$ are shown in the green and yellow bands, respectively. The effect of the large systematic uncertainty in the background expectation in the high mass tail is seen in the widening of these bands. The W' cross section is also shown in these plots. The expected excluded mass for this signal is represented by the intersection of the expected cross section limit with the W' cross section at that mass. The observed excluded mass is similarly found as the intersection of the observed cross section limit with the W' cross section at that mass. The effects of the degraded signal acceptance at very high signal mass, described in Section 8.4 are seen in the similarly degraded performance of the expected and observed limits in this region. The excluded W' cross section times branching ratio at mass points between 200 and 1600 GeV

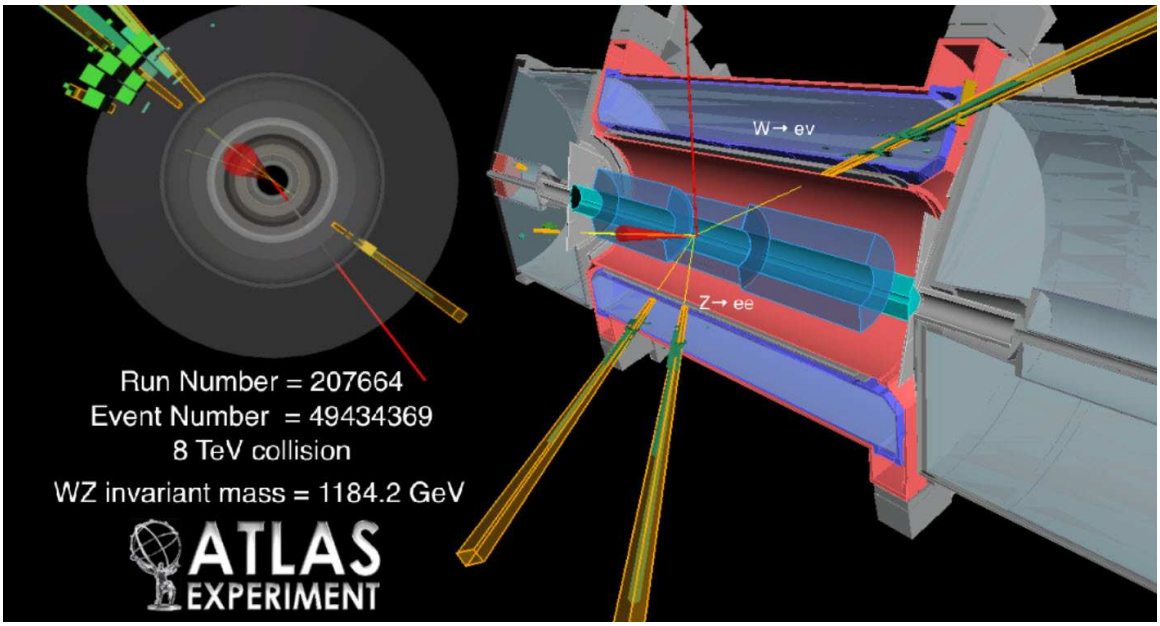

Figure 10.9: An event display of the event with the highest observed $m(WZ)$ of 1184 GeV. Here three electrons are reconstructed from, with their calorimeter energy deposits seen in yellow. The missing energy the event is reconstructed and shown in red.

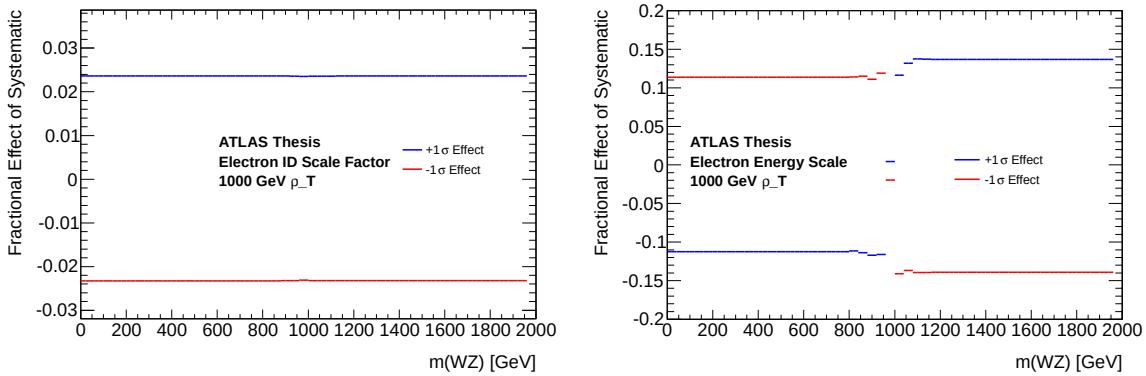

Figure 10.10: The effect of varying the systematic uncertainties associated with the electron identification scale factor (left) and electron energy scale (right) after the systematic uncertainty smoothing procedure. The effect of each systematic uncertainty is smooth and well defined, even in bins with little or no data.

Table 10.9: The p-value, given the background only hypothesis, that the background fluctuates to or above the data in each channel. Systematic uncertainties are included in this calculation.

W' Mass	$e\nu ee$	$\mu\nu ee$	$e\nu\mu\mu$	$\mu\nu\mu\mu$	Combination
200	0.86	0.29	0.47	0.84	0.71
250	0.36	0.31	0.14	0.63	0.31
300	0.056	0.22	0.0067	0.48	0.032
350	0.057	0.21	0.00073	0.36	0.0087
400	0.27	0.23	0.018	0.067	0.012
450	0.64	0.28	0.11	0.0082	0.035
500	0.39	0.53	0.14	0.0046	0.029
550	0.18	0.77	0.14	0.014	0.05
600	0.13	0.71	0.14	0.049	0.061
650	0.29	0.48	0.37	0.088	0.17
700	0.34	0.32	0.61	0.18	0.28
750	0.19	0.31	0.65	0.3	0.32
800	0.14	0.37	0.29	0.5	0.28
850	0.14	0.38	0.23	0.59	0.29
900	0.19	0.39	0.072	0.62	0.22
950	0.22	0.41	0.03	0.64	0.19
1000	0.17	0.42	0.023	0.68	0.15
1050	0.11	0.43	0.022	0.66	0.099
1100	0.052	0.44	0.03	0.66	0.078
1150	0.018	0.43	0.052	0.66	0.076
1200	0.012	0.57	0.12	0.62	0.089
1250	0.028	0.44	0.13	0.65	0.12
1300	0.035	0.45	0.14	0.65	0.17
1350	0.045	0.45	0.15	0.64	0.24
1400	0.052	0.41	0.15	0.57	0.28
1450	0.051	0.46	0.14	0.63	0.28
1500	0.049	0.47	0.14	0.62	0.28
1550	0.054	0.47	0.14	0.62	0.28
1600	0.063	0.5	0.16	0.56	0.35

is shown in Table 10.10. The expected and observed limits on W' masses are shown in Table 10.11. The excluded cross sections are worse than expected by 1 to 2σ in most regions because of the excess of data observed in the signal region. Even so, this excess is not large enough to be interpreted as a new physics signal. An EGM W' below 1180 GeV is excluded at 95% confidence level.

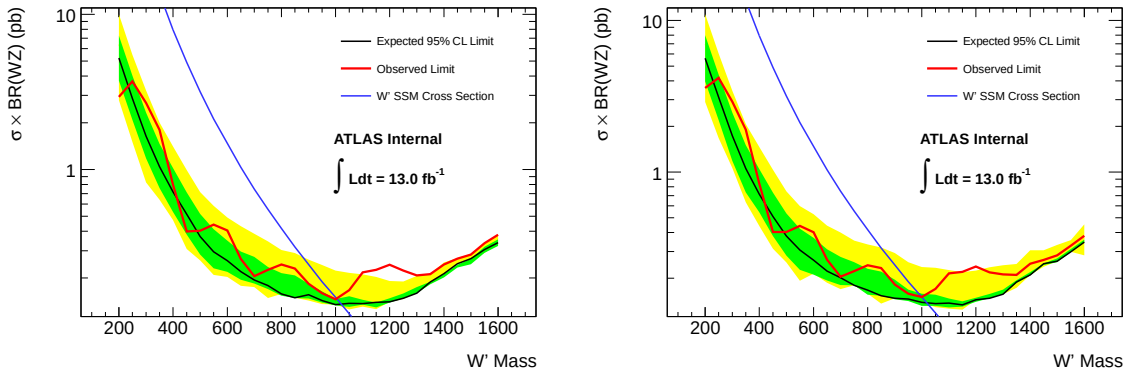

Figure 10.11: The expected excluded production cross section limit at 95% C.L. multiplied by the braching fraction for the $e\nu ee$ final state assuming the $W' \rightarrow WZ$ signal for the case of no systematic uncertainties (left) and full systematics uncertainties (right)

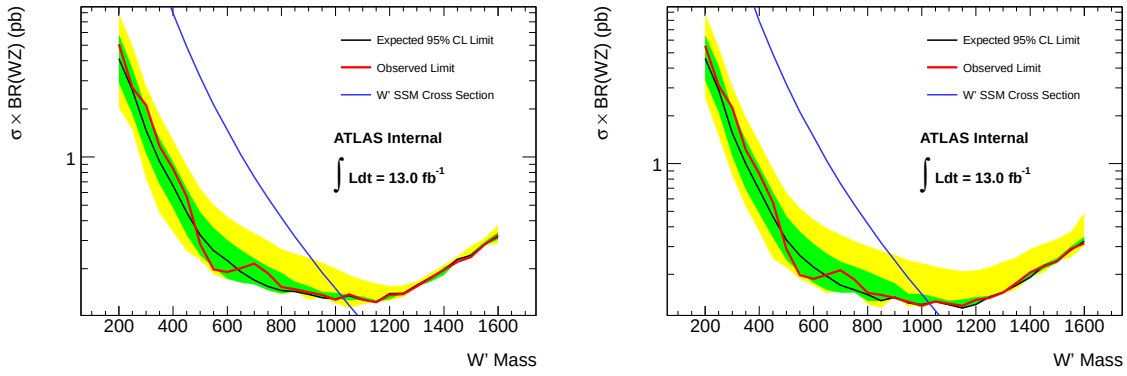

Figure 10.12: The expected excluded production cross section limit at 95% C.L. multiplied by the braching fraction for the $\mu\nu ee$ final state assuming the $W' \rightarrow WZ$ signal for the case of no systematic uncertainties (left) and full systematic uncertainties (right)

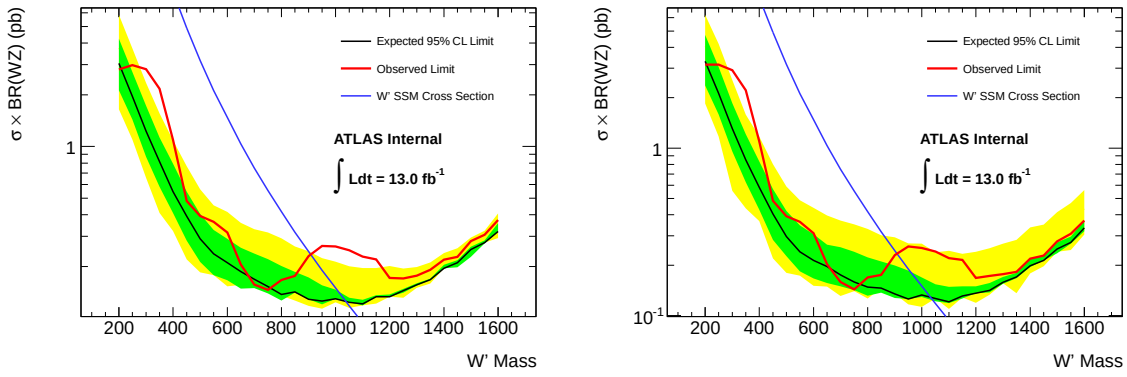

Figure 10.13: The expected excluded production cross section limit at 95% C.L. multiplied by the braching fraction for the $e\nu\mu\mu$ final state assuming the $W' \rightarrow WZ$ signal for the case of no systematic uncertainties (left) and full systematic uncertainties (right)

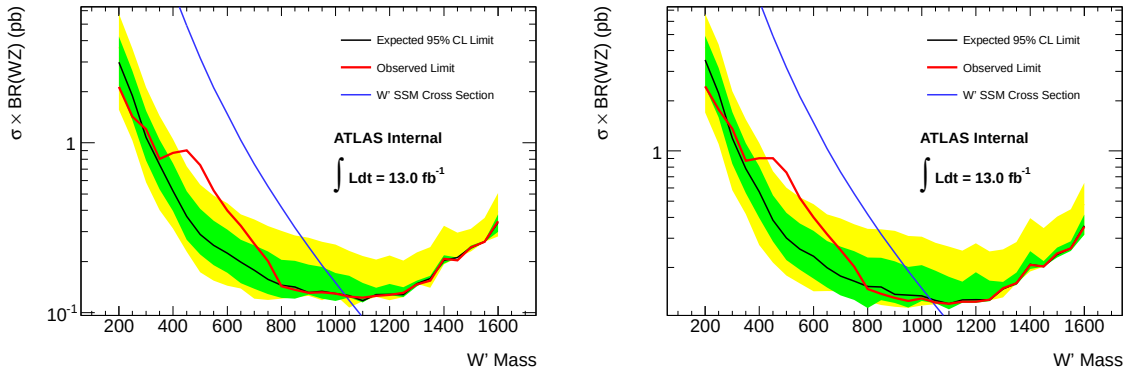

Figure 10.14: The expected excluded production cross section limit at 95% C.L. multiplied by the braching fraction for the $\mu\nu\mu\mu$ final state assuming the $W' \rightarrow WZ$ signal for the case of no systematic uncertainties (left) and full systematic uncertainties (right)

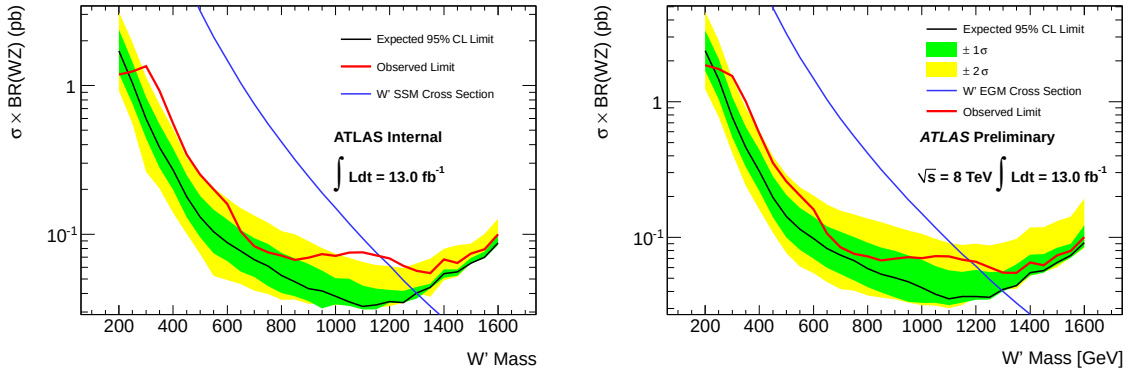

Figure 10.15: The expected excluded production cross section limit at 95% C.L. multiplied by the braching fraction for the combined $e\nu ee$, $\mu\nu ee$, $e\nu\mu\mu$, and $\mu\nu\mu\mu$ final state assuming the $W' \to WZ$ signal for the case of no systematic uncertainties (left) and full systematic uncertainties (right)

10.2.4 Interpretation as ρ_{TC}

In a similar manner, $\sigma^{95\%}$ and all intermediate steps are obtained obtained for all of the ρ_T mass hypotheses in each lepton-flavor channel and for the simultaneous fit to all lepton-flavor channels. The exclusion power for ρ_T signals is very similar to that for W' signals, with differences in the excluded mass changing mostly as a result of difference in the signal cross section. The cross section limits for ρ_T are derived for the combination of all lepton-flavor channels and are shown in Figure 10.16 for two assumptions in the technicolor mass hierarchy: $m(a_T) = 1.1m(\rho_T)$ and $m(a_T) \to \infty$. While the $m(a_T) \to \infty$ samples are not fully simulated, the effect of changing $m(a_T)$ is entirely on the resulting cross section times branching fraction. That effect is taken into account by scaling the fully reconstructed signals by the ratio in cross section. All systematic uncertainties are taken into account for these plots. The excluded cross section for these two mass hierarchy hypotheses is shown in Table 10.12 For $m(a_T) = 1.1m(\rho_T)$ a ρ_T with a mass below 870 GeV is excluded in the scenario $m(\pi_T) = m(\rho_T) - m(W)$.

Similarly, because the effect of varying the techipion mass is only to change the cross section times branching fraction of the ρ_T signal, the excluded cross section at a given mass can be used to set limits in the $m(\rho_T)$ vs $m(\pi_T)$ plane. To generate this two dimensional exclusion, the cross section times branching fraction for a large number of $m(\rho_T)$ and $m(\pi_T)$ points must be calculated. This calculation is performed in PYTHIA at leading order in α_s. Those cross sections are in Table 10.13

A coarse two-dimensional exclusion plot in $m(\rho_T)$ and $m(\pi_T)$ can then be computed by comparing the production cross section for a given point to the excluded cross section for the m_{ρ_T} of that point. If a point has a larger cross section than the relevant excluded cross section, that point in $m(\rho_T)$ and $m(\pi_T)$ space is excluded. The results of such an approach

Table 10.10: Expected and observed limit at 95% C.L. on the $\sigma \times B$ [pb] of the $W' \to WZ$ production, as a function of the W' mass

W' Mass [GeV]	Excluded $\sigma \times B$ [fb]	
	Expected	Observed
200.0	2392.0	1852.0
250.0	1458.0	1722.0
300.0	758.9	1546.0
350.0	454.8	1005.0
400.0	309.1	587.2
450.0	197.9	351.8
500.0	139.4	257.2
550.0	115.2	203.5
600.0	97.66	159.8
650.0	82.31	107.3
700.0	74.26	85.71
750.0	66.24	75.25
800.0	59.59	72.78
850.0	52.98	67.44
900.0	49.79	69.51
950.0	47.13	71.19
1000.0	42.95	71.06
1050.0	38.14	72.61
1100.0	35.1	72.61
1150.0	36.31	68.46
1200.0	36.2	67.02
1250.0	35.67	60.03
1300.0	41.83	54.94
1350.0	44.41	51.2
1400.0	56.04	66.14
1450.0	55.56	61.47
1500.0	63.42	73.81
1550.0	72.76	79.9
1600.0	91.45	93.39

are seen in Figure 10.17.

A more careful approach to this two-dimensional limit is performed by calculating the ratio of the production cross section to the excluded cross section at each point, drawing a smooth grid in between these points, and then projecting out the contour where $\sigma_{prod}/\sigma^{95\%} = 1$. The resulting exclusion plot for both the expected and observed limits and both the

Table 10.11: Expected and observed lower mass limits for the EGM W' boson in the $e\nu ee$, $e\nu\mu\mu$, $\mu\nu ee$, $\mu\nu\mu\mu$ channels as well as the combination of all channels

Signal	$e\nu ee$ [GeV]	$\mu\nu ee$ [GeV]	$e\nu\mu\mu$ [GeV]	$\mu\nu\mu\mu$ [GeV]	Combination [GeV]
EGM W' (expected w/o systematics)	1023	1027	1027	1036	**1299**
EGM W' (observed w/o systematics)	1004	1027	909	1039	**1165**
EGM W' (expected w/ systematics)	1020	1028	1034	1032	**1295**
EGM W' (observed w/ systematics)	1000	1029	909	1039	**1178**

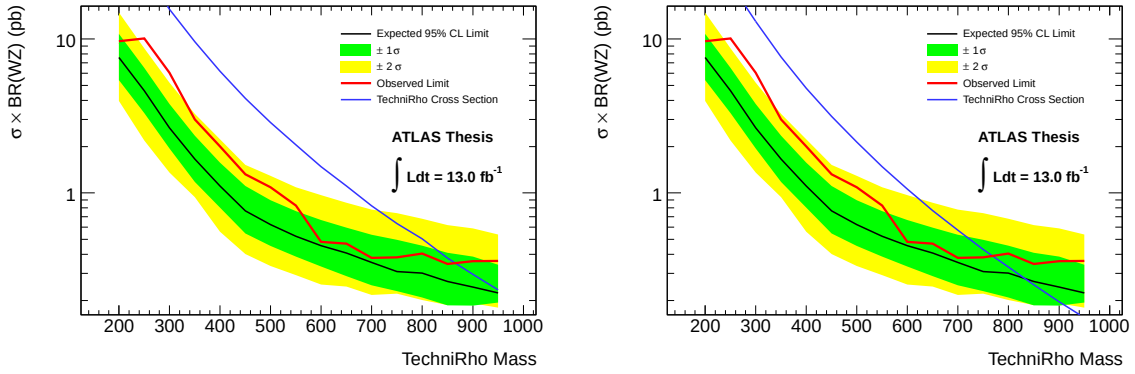

Figure 10.16: The expected excluded production cross section limit at 95% C.L. multiplied by the braching fraction for the combined $e\nu ee$, $\mu\nu ee$, $e\nu\mu\mu$, and $\mu\nu\mu\mu$ final state assuming the $\rho_T \to WZ$ signal for the case of $m(a_T) = 1.1m(\rho_T)$(left) and $m(a_T) \to \infty$ (right)

Table 10.12: Expected and observed limits on the ρ_T , with $m(a_T) = 1.1m(\rho_T)$ and $m(a_T) \to \infty$ for $m(\pi_T) = m(\rho_T) - m(W)$

Signal	$m(a_T) = 1.1m(\rho_T)$	$m(a_T) \to \infty$
ρ_T Expected	960 [GeV]	835 [GeV]
ρ_T Observed	870 [GeV]	770 [GeV]

$m(a_T) = 1.1m(\rho_T)$ and $m(a_T) \to \infty$ assumptions is shown in in Figure 10.18

Table 10.13: The production cross sections for the $\rho_T \to WZ \to \ell\nu\ell\ell$ process for several ρ_T masses and five assumptions on the ρ_T-π_T mass difference. All cross sections times branching fraction are computed at leading order in α_s by PYTHIA.

ρ_T Mass	$\sigma \times B$ [fb] $\Delta m = 0$	$\sigma \times B$ [fb] $\Delta m = 50$	$\sigma \times B$ [fb] $\Delta m = 100$	$\sigma \times B$ [fb] $\Delta m = 150$	$\sigma \times B$ [fb] $\Delta m = 200$	$\sigma \times B$ [fb] $\Delta m = 250$
200	594.6	567.9	-	-	-	-
250	396.3	380.5	182.7	-	-	-
300	234.9	224.4	134.3	49.42	-	-
350	143.4	137.8	93.82	39.64	16.31	-
400	93.34	88.79	65.76	31.42	18.42	8.397
450	63.09	59.07	46.11	24.71	14.97	8.046
500	43.92	41.16	33.4	19.61	12.14	8.35
550	31.11	29.43	24.39	15.52	9.955	6.916
600	22.62	21.24	18.21	12.26	8.201	5.726
650	16.93	15.9	13.62	9.765	6.659	4.738
700	12.66	11.85	10.44	7.795	5.514	3.935
750	9.666	9.057	7.999	6.185	4.558	3.353
800	7.411	7.233	6.294	4.97	3.715	2.786
850	5.679	5.409	4.881	3.995	3.099	2.357
900	4.469	4.246	3.886	3.221	2.552	1.961
950	3.513	3.368	3.072	2.606	2.121	1.662
1000	2.789	2.665	2.462	2.121	1.744	1.392

NEAR	p50	p100	p150	p200	p250	p300	p350	p400	p450	p500	p550	p600	p650	p700	p750	p800	p850	p900	p950	p1000
r200	-	-	-	-	-	-	-	-	-	-	-	-	-	-	-	-	-	-	-	-
r250	no	no	YES!	YES!	YES!	-	-	-	-	-	-	-	-	-	-	-	-	-	-	-
r300	no	no	no	YES!	YES!	YES!	-	-	-	-	-	-	-	-	-	-	-	-	-	-
r350	no	no	no	YES!	YES!	YES!	YES!	-	-	-	-	-	-	-	-	-	-	-	-	-
r400	no	no	no	no	YES!	YES!	YES!	YES!	-	-	-	-	-	-	-	-	-	-	-	-
r450	-	no	no	no	no	YES!	YES!	YES!	YES!	-	-	-	-	-	-	-	-	-	-	-
r500	-	-	no	no	no	YES!	YES!	YES!	YES!	YES!	-	-	-	-	-	-	-	-	-	-
r550	-	-	-	no	no	no	YES!	YES!	YES!	YES!	YES!	-	-	-	-	-	-	-	-	-
r600	-	-	-	-	no	no	no	YES!	YES!	YES!	YES!	YES!	-	-	-	-	-	-	-	-
r650	-	-	-	-	-	no	no	no	YES!	YES!	YES!	YES!	YES!	-	-	-	-	-	-	-
r700	-	-	-	-	-	-	no	no	no	no	YES!	YES!	YES!	YES!	-	-	-	-	-	-
r750	-	-	-	-	-	-	-	no	no	no	no	YES!	YES!	YES!	YES!	-	-	-	-	-
r800	-	-	-	-	-	-	-	-	no	no	no	no	YES!	YES!	YES!	YES!	-	-	-	-
r850	-	-	-	-	-	-	-	-	-	no	no	no	YES!	YES!	YES!	YES!	YES!	-	-	-
r900	-	-	-	-	-	-	-	-	-	-	no	no	no	no	no	no	YES!	YES!	-	-
r950	-	-	-	-	-	-	-	-	-	-	-	no	no	no	no	no	no	no	no	-
r1000	-	-	-	-	-	-	-	-	-	-	-	-	no	no	no	no	no	no	no	no

Figure 10.17: The expected limits in the $m(\rho_T)$ versus $m(\pi_T)$ plane with $m(a_T) = 1.1m(\rho_T)$. Rows correspond to ρ_T masses, columns correspond to π_T masses. A `YES!` implies that that point is excluded a `no` implies that that point is not excluded. A `-` implies that no technicolor sample was generated at that mass point.

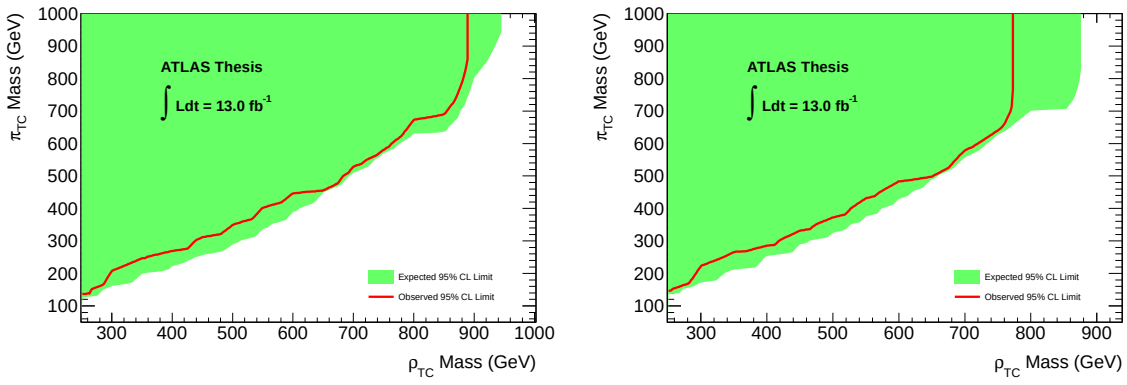

Figure 10.18: The 95% C.L. expected and observed excluded mass regions in the $m(\rho_T)$ versus $m(\pi_T)$ plane obtained from the technicolor samples. Left are the results for $m(a_T) = 1.1m(\rho_T)$ and right are those for $m(a_T) \to \infty$.

Chapter 11

Conclusions

This dissertation presents a search for new physics decaying resonantly to $W^{\pm}Z$ in the $\ell\nu\ell\ell$ channel using 13.0 fb^{-1} of p-p collisions measured using the ATLAS detector between April and September of 2012. Electrons, muons, and missing transverse energy are reconstructed by the detector and built into physics objects for this analysis. The full invariant mass of the leptonic WZ system is reconstructed by assuming that the W boson was on-shell when it decayed. Control regions dominated by Standard Model processes show excellent agreement with the predicted backgrounds.

Given excellent agreement in the Standard Model control regions, a signal region expected to be sensitive resonant WZ production is unblinded. No evidence of such new physics is observed in these data, and limits are set on the production cross section of an EGM W' decaying to WZ. An Extended Gauge Model W' below 1180 GeV is excluded at 95% CL. The resulting cross-section limits as a function of W' mass can be easily applied to any model that produces a narrow resonance that decays to WZ. The relatively wide detector resolution in this region ensures that the results are fairly insensitive to the model considered. Limits are also set using a LSTC model and can be interpreted as the exclusion of a significant portion of $m(\rho_T)$ and $m(\pi_T)$ space in that model. In the specific technicolor model used here with $m_{\rho T} = m_{\pi T} + m_W$ and $m_{aT} = 1.1 m_{\rho T}$, a ρ_T decaying to WZ below 870 GeV is excluded. If, instead $m_{aT} \to \infty$ is assumed, a ρ_T decaying to WZ below 770 GeV is excluded.

An excess between 1σ and 2σ is seen in the overall event counts in the signal region, including the high mass tail of the $m(WZ)$ distribution. This excess degrades the limits observed in this analysis by ~ 100 GeV for each signal compared with the expected power of this analysis Whether this excess is a result of statistical fluctuation or some other effect is not known. While systematic uncertainties in the analysis included PDF and generator effects on the total Standard Model WZ cross section and acceptance, no such analysis was made of the angular variables used to demarcate the signal region. In light of these results, further study of the differential cross section as a function of $\Delta\phi(W, Z)$ and $\Delta y(W, Z)$ should be undertaken.

The LHC has continued to collide protons through 2012, providing 21.7 fb^{-1} of p-p collisions for analysis. An extension of this analysis with the full 2012 dataset will extend

the limits derived here with only small changes to the analysis framework. Additionally, the dominant systematic uncertainty in parts of the signal region is a result only of the limited number of simulated events. This systematic uncertainty, and thus the power of this analysis, could be significantly improved by the simulation of more events, or by the simulation of filtered events, targeted to this high mass tail.

The Large Hadron Collider is now entering its first long shutdown, giving analyzers time to finish and refine their measurements on these first data. The research program of the LHC thus far has been impressive and, while it has given rise to a large number of excellent Standard Model measurements, including the observation of a Higgs boson candidate [15], it has failed to produce discover any new physics signature. The author joins the larger physics community in hoping that the next run of the LHC at design energy and luminosity will see the reversal of this trend.

Bibliography

[1] J. Beringer et al., *Review of Particle Physics*, Phys. Rev. D **86** (2012) 010001.

[2] A. Martin et al., *Parton distributions for the LHC*, Eur. Phys. J. **C63** (2009) 189–285, arXiv:0901.0002 [hep-ph].

[3] J. Andersen et al., *Discovering Technicolor*, Eur. Phys. J. Plus **126** (2011) 81, arXiv:1104.1255 [hep-ph].

[4] CERN, *CERN Accelerator Complex (operating and approved projets).*, LHC-PHO-1991-001 (1991).

[5] CERN, *Diagram of an LHC dipole magnet*, CERN-DI-9906025 (1999).

[6] ATLAS Collaboration, "ATLAS Experiment - Public Luminosity Results." twiki.cern.ch/twiki/bin/view/AtlasPublic/LuminosityPublicResults.

[7] L. Evans and P. Bryant, *LHC Machine*, JINST **3** (2008) S08001.

[8] G. Aad et al., *The ATLAS Experiment at the CERN Large Hadron Collider*, JINST **3** (2008) S08003.

[9] ATLAS Collaboration, *Luminosity Determination in pp Collisions at $s = 7$ TeV using the ATLAS Detector in 2011*, ATLAS-CONF-2011-116 (2011).

[10] ATLAS Collaboration, *Electron performance measurements with the ATLAS detector using the 2010 LHC proton-proton collision data*, Eur. Phys. J. **C72** (2012) 1909, arXiv:1110.3174v2 [hep-ex].

[11] ATLAS Collaboration, *Muon reconstruction efficiency in reprocessed 2010 LHC proton-proton collision data recorded with the ATLAS detector*, ATLAS-CONF-2011-063 (2011).

[12] ATLAS Collaboration, "MCP Mass Performance plots - HCP dataset 2012." atlas.web.cern.ch/Atlas/GROUPS/PHYSICS/MUON/PublicPlots/2012/ATL-COM-MUON-2013-006/index.html.

[13] ATLAS Collaboration, *Charged-particle multiplicities in pp interactions at sqrt(s) = 900 GeV measured with the ATLAS detector at the LHC*, Physics Letters B **688** (2010) 21–42, `arXiv:1003.3124 [hep-ex]`.

[14] ATLAS Collaboration, *Measurement of the top quark-pair production cross section with ATLAS in pp collisions at sqrts=7 TeV*, Eur. Phys. J. **C71** (2011) 1577.

[15] ATLAS Collaboration, *Observation of a New Particle in the Search for the Standard Model Higgs Boson with the ATLAS Detector at the LHC*, Physics Letters B **716** (2012) 1–29, `arXiv:1207.7214v2. [hep-ex]`.

[16] ATLAS Collaboration, *Search for resonant WZ to lvll production using 13 fb.1 in sqrt(s) = 8 TeV pp collisions with ATLAS*, ATLAS-CONF-2013-015 (2013).

[17] S. W. Herb et al., *Observation of a Dimuon Resonance at 9.5 GeV in 400-GeV Proton-Nucleus Collisions*, Phys. Rev. Lett. **39** (1977) 252–255.

[18] CDF Collaboration, F. Abe et al., *Observation of Top Quark Production in pp Collisions with the Collider Detector at Fermilab*, Physical Review Letters **74** (1995) 2626–2631.

[19] D0 Collaboration, S. Abachi et al., *Search for High Mass Top Quark Production in pp Collisions at vs = 1.8 TeV*, Physical Review Letters **74** (1995) 2422–2426.

[20] K. Kodama et al., *Observation of tau neutrino interactions*, Phys. Lett. B **504** (2000) 218–224.

[21] D. Griffiths, *Introduction to Elementary Particles*. WILEY, 2008.

[22] M. E. Peskin and D. V. Schroeder, *An Introduction to Quantum Field Theory*. Westview Press, 1995.

[23] D. Gross, *Twenty Five Years of Asymptotic Freedom*, Nucl. Phys. Proc. Suppl. **74** (1999) 426–446.

[24] P. Skands, *Introduction to QCD*, `arXiv:1207.2389 [hep-ph]`.

[25] T. Sjostrand, S. Mrenna, and P. Skands, *PYTHIA 6.4 Physics and Manual*, JHEP **0605** (2006) 026, `arXiv:hep-ph/0603175 [hep-ph]`.

[26] T. Gleisberg et al., *Event generation with SHERPA 1.1*, JHEP **0902** (2009) 007, `arXiv:hep-ph/811.4622`.

[27] M. Mangano et al., *ALPGEN, a generator for hard multiparton processes in hadronic collisions*, JHEP **0307** (2003) 001, `arXiv:hep-ph/0206293`.

[28] M. Patil and P. S. Joshi, *Naked singularities as particle accelerators*, Phys. Rev. D **82** (2010) 104049, arXiv:1011.5550v1.

[29] A. L. Fitzpatrick, G. Perez, and L. Randall, *Flavor from Minimal Flavor Violation and a Viable Randall-Sundrum Model*, Phys. Rev. Lett. **100** (2008) 171604.

[30] E. Eichten, I. Hinchliffe, K. Lane, and C. Quigg, *Supercollider Physics*, Rev. Mod. Phys. **56** (1984) 579–707.

[31] E. Farhi and L. Susskind, *Technicolour*, Phys. Rep. **74,3** (1981) 277–321.

[32] E. Eichten and K. Lane, *Dynamical breaking of weak interaction symmetries*, Phys. Lett. B **90** (1980) 125–130.

[33] R. Foadi, M. T. Frandsen, and F. Sannino, *125 GeV Higgs from a not so light Technicolor Scalar*, arXiv:1211.1083 [hep-ph].

[34] D. Dietrich, F. Sannino, and K. Tuominen, *Light composite Higgs from higher representations versus electroweak precision measurements: Predictions for CERN LHC*, Phys. Rev. **D72** (2005) 055001, arXiv:hep-ph/0505059 [hep-ph].

[35] M. Schmaltz and D. Tucker-Smith, *Little Higgs Review*, Ann. Rev. Nucl. Part. Sci **55** (2005) 229–270, arXiv:hep-ph/05021820 [hep-ph].

[36] N. Arkani-Hamed et al., *The Minimal moose for a little Higgs*, JHEP **0208** (2002) 021, arXiv:hep-ph/0206020 [hep-ph].

[37] G. Altarelli, B. Mele, and M. Ruiz-Altaba, *Searching for new Heavy Vetor Bosons in p anti-p colliders*, Z. Phys. C **45** (1989) 109.

[38] D0 Collaboration, V. Abazov et al., *A measurement of the WZ and ZZ production cross sections using leptonic final states in 8.6 fb^{-1} of $p\bar{p}$ collisions*, FERMILAB-PUB-12-022-E (2012), arXiv:1201.5652 [hep-ex].

[39] CDF Collaboration, T. Aaltonen et al., *Measurement of the WZ Cross Section and Triple Gauge Couplings in $p\bar{p}$ Collisions at $\sqrt{s} = 1.96$ TeV*, Submitted to PRD-RC (2012), 1202.6629.

[40] ATLAS Collaboration, *Measurement of WZ production in proton-proton collisions at sqrt(s) = 7 TeV with the ATLAS detector*, CERN-PH-EP-2012-179 (2012), arXiv:1208.1390 [hep-ex].

[41] CMS Collaboration, *Measurement of the WW, WZ and ZZ cross sections at CMS*, CMS-PAS-EWK-11-010 (2011).

[42] D0 Collaboration, V. Abazov et al., *Search for a resonance decaying into WZ boson pairs in $p\bar{p}$ collisions*, Phys. Rev. Lett. **104** (2010) 061801.

[43] ATLAS Collaboration, *Search for resonant WZ production in the WZ to l nu l' l' channel in sqrt(s) = 7 TeV pp collisions with the ATLAS detector*, Phys. Rev. **D85** (2012) 112012.

[44] CMS Collaboration, *Search for a W' or techni-rho decaying into WZ in pp collisions at sqrt(s) = 7 TeV*, Phys. Rev. Lett. **109** (2012) 141801.

[45] LHC Collaboration, M. Benedikt (ed.), P. Collier (ed.), V. Mertens (ed.), J. Poole (ed.), and k. Schindl (ed.), *LHC Design Report Volume III The LHC Injector Chain*, CERN-2004-003.

[46] J. Blewett, *200-GeV Intersecting Storage Accelerators*, 8th Int. Conf. on High Energy Acel. (1971) 501–504.

[47] LHC Collaboration, M. Bajko et al., *Report of the Task Force on the Incident of 19 September 2008 at the LHC*, LHC-PROJECT-REPORT-1168 (2009).

[48] S. Myers and F. Zimmermann, eds., *Chamonix 2010 Summary Report*, Proceedings of Chamonix 2010 workshop on LHC Performance. 2010.

[49] S. Myers and F. Zimmermann, eds., *Chamonix 2012 Summary Report*, Proceedings of Chamonix 2012 workshop on LHC Performance. 2012.

[50] S. Chatrchyan et al., *The CMS experiment at the CERN LHC*, JINST **3** (2008) S08004.

[51] A Augusto Alves Jr et al., *The LHCb Detector at the LHC*, JINST **3** (2008) S08005.

[52] K. Aamodt et al., *The ALICE experiment at the CERN LHC*, JINST **3** (2008) S08002.

[53] ATLAS Collaboration, *ATLAS pixel detector electronics and sensors*, JINST **3** (2008) S07007.

[54] ATLAS TRT Collaboration, E. Abat et al., *The ATLAS Transition Radiation Tracker (TRT) proportional drift tube: design and performance*, JINST **3** (2008) S02013.

[55] ATLAS Collaboration, *Readiness of the ATLAS Liquid Argon Calorimeter for LHC Collisions*, Eur. Phys. J. **C70** (2010) 723–753, `arXiv:0912.2642 [hep-ex]`.

[56] ATLAS Collaboration, *Expected Performance of the ATLAS Experiment: Detector, Trigger and Physics*, ATLAS-OPEN-2008-020 (2008).

[57] ATLAS Collaboration, *Study of the Hadron Shower Profiles with the Tile Hadron Calorimeter*, CERN-LHCC-96-042.

[58] A. Yamamoto et al., *Progress in ATLAS central solenoid magnet*, IEEE Transactions on Applied Superconductivity **10** (2000) 353–356.

[59] S. Palestini, *The muon spectrometer of the ATLAS experiment*, Nucl. Phys. **125** (2003) 337.

[60] ATLAS Collaboration, *ATLAS Muon Spectrometer Technical Design Report*, CERN-LHCC-97-022 (1997).

[61] ATLAS Collaboration, *Characterization of Interaction-Point Beam Parameters Using the pp Event- Vertex Distribution Reconstructed in the ATLAS Detector at the LHC*, ATLAS-CONF-2010-02727 (2010).

[62] ATLAS Collaboration, T. Cornelissen et al., *The new ATLAS track reconstruction (NEWT)*, J. Phys. Conf. Ser. **119** (2008) 032014.

[63] R. Fruhwirth, *Application of Kalman filtering to track and vertex fitting*, Nucl. Instrum. Meth. **A262** (1987) 444–450.

[64] ATLAS Collaboration, *Performance of primary vertex reconstruction in proton-proton collisions at ps = 7 TeV in the ATLAS experiment*, ATLAS-CONF-2010-069 (2010).

[65] R. Fruhwirth, W. Waltenberger, and P. Vanlaer, *Adaptive vertex Fitting*, J. Phys. **G34** (2007) N343.

[66] ATLAS Collaboration, *Electron and photon reconstruction and identification in ATLAS: expected performance at high energy and results at 900 GeV*, ATLAS-CONF-2010-005 (2010).

[67] R. Nicolaidou et al., *Muon identification procedure for the ATLAS detector at the LHC using Muonboy reconstruction package and tests of its performance using cosmic rays and single beam data*, Journal of Physics: Conference Series **219** (2010), 032052.

[68] W. Lampl et al., *Calorimeter Clustering Algorithms: Description and Performance*, ATLAS-LARG-PUB-2008-002 (2008).

[69] M. Cacciari, G. P. Salam, and G. Soyez, *The Anti-k(t) jet clustering algorithm*, JHEP **0804** (2008) 063, arXiv:0802.1189 [hep-ph].

[70] ATLAS Collaboration, *Performance of Missing Transverse Momentum Reconstruction in Proton-Proton Collisions at 7 TeV with ATLAS*, Eur. Phys. J. **C72** (2012) 1844, arXiv:1108.5602 [hep-ex].

[71] GEANT4 Collaboration, S. Agostinelli et al., *GEANT4: A simulation toolkit*, Nucl. Instrum. Meth. A **506** (2003) 250–303.

[72] E. Eichten and K. Lane, *Low-scale technicolor at the Tevatron and LHC*, Phys. Lett. B **669** (2008) 235–238, arXiv:0706.2339 [hep-ph].

[73] R. Foadi, M. Frandsen, T. A. Ryttov, and F. Sannino, *Minimal Walking Technicolor: Set Up for Collider Physics*, Phys. Rev. **D76** (2007) 055005, arXiv:0706.1696 [hep-ph].

[74] T. Sjostrand, S. Mrenna, and P. Skands, *A Brief Introduction to PYTHIA 8.1*, Comput. Phys. Commun. **178** (2008) 852–867, arXiv:0710.3820 [hep-ph].

[75] A. Sherstnev and R. Thorne, *Different PDF approximations useful for LO Monte Carlo generators*, arXiv:0807.2132 [hep-ph].

[76] E. Boos et al., eds., *Generic User Process Interface for Event Generators*, Physics at TeV Colliders II Workshop. 2001. arXiv:hep-ph/0109068.

[77] P. Nason, *A New method for combining NLO QCD with shower Monte Carlo algorithms*, JHEP **0411** (2004) 040, arXiv:hep-ph/0409146 [hep-ph].

[78] T. Melia, P. Nason, R. Rntsch, and G. Zanderighi, *W+W-, WZ and ZZ production in the POWHEG BOX*, JHEP **1111** (2011) 078, arXiv:1107.5051 [hep-ph].

[79] P. M. Nadolsky et al., *Implications of CTEQ global analysis for collider observables*, Phys. Rev. **D78** (2008) 013004, arXiv:0802.0007 [hep-ph].

[80] P. Golonka and Z. Was, *PHOTOS Monte Carlo: A Precision tool for QED corrections in Z and W decays*, Eur. Phys. J. **C45** (2006) 97–107, arXiv:hep-ph/0506026 [hep-ph].

[81] S. Jadach, Z. Was, R. Decker, and J. Kuhn, *The τ decay library TAUOLA, version 2.4*, Comput. Phys. Commun. **76** (1993) 361–380.

[82] J. M. Campbell and R. K. Ellis, *An update on vector boson pair production at hadron colliders*, Phys. Rev. D **60** (1999) 113006, arXiv:hep-ph/9905386.

[83] S. Frixione, P. Nason, and C. Oleari, *Matching NLO QCD computations with Parton Shower simulations: the POWHEG method*, JHEP **0711** (2007) 070, arXiv:0709.2092 [hep-ph].

[84] ATLAS Collaboration, *Performance of the ATLAS muon trigger in 2011*, ATLAS-CONF-2012-099 (2012).

[85] ATLAS Collaboration, *Performance of the ATLAS Electron and Photon Trigger in p-p Collisions at sqrts = 7 TeV in 2011*, ATLAS-CONF-2012-048 (2012).

[86] ATLAS Collaboration, *ATLAS Muon Momentum Resolution in the First Pass Reconstruction of the 2010 p-p Collision Data at sqrt(s)= 7TeV*, ATLAS-CONF-2011-046 (2011).

[87] ATLAS Collaboration, *Determination of the muon reconstruction efficiency in ATLAS at the Z resonance in proton-proton collisons at s = 7 TeV*, ATLAS-CONF-2011-008 (2011).

[88] ATLAS Collaboration, *Jet energy scale and its systematic uncertainty in proton-proton collisions at s = 7 TeV with ATLAS 2011 data*, ATLAS-CONF-2013-004 (2013).

[89] ATLAS Collaboration, *Performance of Missing Transverse Momentum Reconstruction in ATLAS with 2011 Proton-Proton Collisions at s = 7 TeV*, ATLAS-CONF-2012-101 (2012).

[90] ATLAS Collaboration, *Measurement of WZ production in proton-proton collisions at sqrt(s) = 7 TeV with the ATLAS detector*, Eur. Phys. J. (2012), `arXiv:1208.1390 [hep-ex]`.

[91] ATLAS Collaboration, *Measurement of ZZ production in pp collisions at sqrt(s)=7 TeV and limits on anomalous ZZZ and ZZgamma couplings with the ATLAS detector*, JHEP (2012), `arXiv:1211.6096 [hep-ex]`.

[92] ATLAS Collaboration, *Measurement of Wgamma and Zgamma production in proton-proton collisions at sqrt(s)=7 TeV with the ATLAS Detector*, JHEP **09** (2011) 072, `arXiv:1106.1592 [hep-ex]`.

[93] T. Stelzer and W. F. Long, *Automatic Generation of Tree Level Helicity Amplitudes*, Comput. Phys. Commun. **81** (1994) 357–371, `arXiv:9401258 [hep-ph]`.

[94] W. Verkerke and D. Kirkby, eds., *The RooFit toolkit for data modeling*, Computing in High Energy and Nuclear Physics (CHEP03). 2003. `arXiv:physics/0306116v1`.

[95] T. Junk, *Confidence level computation for combining searches with small statistics*, Nucl. Instrum. Meth. **A434** (1999) 435–443, `arXiv:hep-ex/9902006 [hep-ex]`.

[96] T. Carli et al., eds., *Experimental determination of Parton Distributions*, HERA and the LHC. 2004.

[97] A. L. Read, *Presentation of search results: the CLs technique*, J. Phys. **G28** (2002) 2693.